TUM School of Natural Science
Technical University of Munich

The Simulation of Polarized Light Propagating in Ocean Water

And its Application to the Pacific Ocean Neutrino Experiment

Tobias Kerscher

Master Thesis

May 29, 2024

Supervisor:	Prof. Dr. Elisa Resconi
Second Accessor:	Prof. Dr. Laura Fabbietti
Advisor:	Dr. Philipp Eller

I know that human beings and fish can coexist peacefully.

– George W. Bush

Abstract

The rather new and uprising field of neutrino-astronomy requires massive detectors. Complementing the already existing experiments such as IceCube, KM3NeT and Baikal-GVD, the Pacific Ocean Neutrino Experiment (P-ONE) is a proposed multi-cubic kilometer neutrino telescope to be deployed in the Cascadia Basin near Vancouver Island starting 2025. In order to be able to interpret the faint light signals caused by neutrino and muon events, a detailed understanding of its propagation to the detector is required.

After investigating the effects influencing the propagation of light in ocean water and introducing algorithms suited to handle the complex underlying mathematical problem, we combine both to create a software package capable of simulating it efficiently. The implementation runs on GPUs as they are not only predestined for such massively parallelizable tasks but nowadays also include dedicated ray tracing hardware, allowing the easy incorporation of arbitrary detector shapes.

Special attention is given to polarization and whether this effect can measurably impact signals.

Contents

Abstract **iii**

Contents **v**

1 Introduction **1**

2 Neutrino Astronomy **3**
2.1 Neutrino Sources . . . 3
2.2 Neutrino Telescopes . . . 5
2.3 P-ONE . . . 9

3 Light Model **11**
3.1 Radiometric Units . . . 11
3.2 Transient Light Propagation . . . 12
3.3 Refraction in Media . . . 12
3.4 Polarization Effects . . . 13

4 Light Interaction with Media **17**
4.1 At Interfaces . . . 17
4.2 Absorption . . . 19
4.3 Elastic Scattering . . . 20
4.4 Inelastic Scattering . . . 22
4.5 Equation of Transfer . . . 23

5 Polarization **27**
5.1 Stokes-Mueller Formalism . . . 27
5.2 Media Interaction . . . 28
5.3 Vector Radiative Transfer Equation . . . 31

6 Simulation Algorithm **33**
6.1 Path Integrals . . . 33
6.2 Monte Carlo Method . . . 35
6.3 Unidirectional Path Tracing . . . 37
6.4 Bidirectional Path Tracing . . . 42

7 Simulations **45**
7.1 Light Propagation and Energy Conservation . . . 45
7.2 Oceanic Water Simulation . . . 48
7.3 P-ONE Demonstrator . . . 52

8 Conclusion **55**

A GPGPU Programming **57**
A.1 GPU Execution Model . . . 57
A.2 Hardware Accelerated Ray Tracing . . . 58

B Source Code **59**

Bibliography **61**

List of Figures

2.1 Grand Unified Neutrino Spectrum (GUNS) . . . 3
2.2 Neutrino Cross Section . . . 6
2.3 Neutrino Interactions . . . 7
2.4 Cherenkov Radiation using Huygens Principle . . . 7
2.5 Cherenkov Cone . . . 8
2.6 Map of P-ONE Location . . . 9
2.7 P-ONE String . . . 9
2.8 Renderings of P-ONE Modules . . . 10
2.9 Rendering of P-OM Attached to String . . . 10

3.1 Phase and Group Velocity in Ocean water . . . 12
3.2 PMT Layer Model . . . 13
3.3 Optical PMT Properties at Glass-Cathode Interface . . . 14
3.4 PMT Characteristics in Air and Water . . . 15
3.5 Cosine Weighted PMT Characteristics in Air and Water . . . 15

4.1 Refraction into Denser Medium . . . 18
4.2 Absorption Coefficient of Pure Water . . . 19
4.3 Henyey-Greenstein Phase Function . . . 20
4.4 Fournier-Forand Phase Function . . . 20
4.5 Einstein-Smoluchowski Phase Function . . . 20
4.6 Petzold VSF Measurement . . . 21
4.7 Scattering Coefficient of Sea Water . . . 22
4.8 Raman Scattering Distribution . . . 23
4.9 Attenuating Media Interactions . . . 24
4.10 Enhancing Media Interaction . . . 24

5.1 Stokes Vector Illustration . . . 27
5.2 Rotating Stokes Vector . . . 28
5.3 Normalized Phase Matrix . . . 30

6.1 Surface Path Segment . . . 34
6.2 Comparison RNG and Sobol . . . 37
6.3 Detetector MIS in UDPT . . . 38
6.4 BDPT Connection Example . . . 42
7.1 Energy Conservation Test Setup . . . 45

7.2 Simulated Light Curves for Varying Scattering Coefficients . . . 46
7.3 Light curves for varying asymmetry parameter g . . . 47
7.4 Model for Absorption and Scattering in Deep Pacific Ocean . . . 49
7.5 Light Curves of a Spherical Light Source in Water . . . 50
7.6 Observed Polarization Degree from a Cherenkov Track . . . 51
7.7 Polarization Anisotropy Setup . . . 51
7.8 Polarization Anisotropy Simulation . . . 52
7.9 P-ONE 10 String Positions . . . 52
7.10 Cherenkov Angles in Water . . . 52
7.11 Shadowed P-OM Comparison . . . 53

7.12 P-ONE Demonstrator Simulation 54
A.1 Ray Tracing Illustration 58

List of Tables

7.1 Water Model Parameters 49

1 Introduction

The origins of astronomy trace back several thousand years to the earliest known human societies, influencing their culture and making it arguably one of the oldest scientific fields [1]. Only since in comparison relatively short period of time, have we stopped relying solely on light for extraterrestrial observations and moved on to a method now known as *multimessenger astronomy* combining multiple sources of information. Besides cosmic rays[1] discovered by Victor Hess in 1912, this nowadays also includes gravitational waves and neutrinos allowing us to probe regions of the universe not accessible by light [2]. This work focuses on the latter.

[1]: McLeod (2016), *Astronomy in the Ancient World: Early and Modern Views on Celestial Events*

1: Cosmic rays are actually particles. This misnomer has historical reasons.

[2]: Spurio (2014), *Particles and Astrophysics*

Besides IceCube [3] being perhaps the most prominent neutrino telescope gaining broad recognition in recent times through its discovery of a neutrino source [4], there are also several other ones at different locations such as KM3NeT in the Mediterranean Sea [5] or Baikal-GVD in southeast Russia [6]. However, the existing constellation does not cover the complete sky with satisfying sensitivity, making it desirable to add new neutrino telescopes complementing them [7].

[3]: Karle et al. (2003), 'IceCube — the next generation neutrino telescope at the South Pole'

[4]: IceCube Collaboration et al. (2018), 'Neutrino emission from the direction of the blazar TXS 0506+056 prior to the IceCube-170922A alert'

[5]: Katz (2006), 'KM3NeT: Towards a km3 Mediterranean neutrino telescope'

[6]: Avrorin et al. (2022), 'Deep-Underwater Cherenkov Detector in Lake Baikal'

[7]: Schumacher et al. (2021), 'PLEνM: A global and distributed monitoring system of high-energy astrophysical neutrinos'

The Pacific Ocean Neutrino Experiment (P-ONE) is a proposed multi-cubic kilometer neutrino telescope located in the Cascadia Basin off the shore of Vancouver Island in Canada aiming to increase the coverage in the Southern Hemisphere.[2] After two successful pathfinder missions, STRAW [8] and STRAW-b [9] (*STRings for Absorption in Water*), its deployment is planned to start in 2025 and will take advantage of the already existing deep-sea infrastructure maintained by Ocean Networks Canada [10, 11].

2: Neutrino telescopes typically use the entire earth as shielding against background noise by locking 'down', that is through the earth making them sensitive to the hemisphere opposite to their location.

[8]: Boehmer et al. (2019), 'STRAW (STRings for Absorption length in Water): pathfinder for a neutrino telescope in the deep Pacific Ocean'

[9]: Rea et al. (2021), 'P-ONE second pathfinder mission: STRAW-b'

[10]: Agostini et al. (2020), 'The Pacific Ocean Neutrino Experiment'

[11]: Malecki (2024), 'Pacific Ocean Neutrino Experiment'

Despite their massive experimental setup typically encompassing cubic kilometers of volume, neutrino telescopes have to be able to detect very faint signals. Using the apparent area as a rough estimate while ignoring scattering and absorption, already at a distance of 10 m, we expect only about 10 photons from a single Cherenkov track to even reach a spherical detector of 50 cm in diameter.[3] A detailed understanding of the photon propagation to the detector is thus obviously needed. Since analytical solutions are usually infeasible, one relies on simulations instead.

3: A typical Cherenkov track produces roughly 3,500 photons per meter the particle traveled. See Subsection 2.2.2 on page 6.

This thesis aims to create a software framework capable of simulating light propagation tailored explicitly towards the oceanic setting of P-ONE using modern hardware such as GPUs and hardware-accelerated ray tracing. Starting with a brief introduction into the field of neutrino astronomy, we then investigate and describe the effects on light as it propagates through ocean water and finally interacts with detectors, and whether these are worthwhile to include in the simulation. Particular focus thereby lies on polarization as it appears to be currently neglected in other neutrino telescopes.[4] After introducing the algorithms used for the simulation, we finally present results produced by it. Following this introduction as **Chapter 1**, the remaining outline is described below:

4: For instance, to our best knowledge neither IceCube nor Baikal-GVD mention polarization in their reports on optical properties [12, 13].

[12]: Ackermann et al. (2006), 'Optical properties of deep glacial ice at the South Pole'

[13]: Ryabov et al. (2021), 'Monitoring of optical properties of deep lake water'

Chapter 2 gives a brief introduction to the topic of neutrino astronomy: Starting with an investigation of the neutrino flux spectrum and its sources, we then give a short description of the working principles of neutrino telescopes in general, followed by a detailed one on P-ONE.

In **Chapter 3**, we develop the light model used in the simulation while investigating which effects are worthwhile to include. This includes a radiometric description of light, its propagation speed, refraction and polarization.

Chapter 4 presents the physical models that determine the propagation of light through a medium and its interaction with it, such as refraction at interfaces, scattering and absorption.

Chapter 5 focuses on polarization by introducing the Stokes-Mueller formalism as the typical model describing it and extending the concepts and effects of Chapter 4 to respect polarization.

Following the physical models, **Chapter 6** introduces the methods and algorithms implemented in the simulation: Path integrals reformulate the propagation problem in a more manageable way, which can be solved using the Monte Carlo methods shown afterwards. With unidirectional and bidirectional path tracing, two algorithms based on this concept are presented.

Chapter 7 presents results from simulations using the developed software. Starting with a test on energy conservation to see whether it produces correct results, we then simulate and investigate the propagation of light through ocean water and conclude with a full simulation of a potential P-ONE configuration.

To conclude, **Chapter 8** briefly summarizes this thesis and gives an outlook on possible future work.

Neutrino Astronomy 2

2.1 Neutrino Sources 3
2.2 Neutrino Telescopes 5
2.3 P-ONE 9

Introduced by Wolfgang Pauli in 1930 as a 'desperate remedy' to fix the seemingly violation of energy and momentum conservation observed in the radioactive beta decay [14], neutrinos managed to increasingly attract the interest of scientists and became, at the latest with the discovery of the blazar TXS-0506+056 as a point source, an established part of astronomy [4].

[14]: Pauli (1985), *Scientific Correspondence with Bohr, Einstein, Heisenberg a.o.*

[4]: IceCube Collaboration et al. (2018), 'Neutrino emission from the direction of the blazar TXS 0506+056 prior to the IceCube-170922A alert'

Since neutrinos exclusively interact via the weak force, they show only a very low cross section, making them hard to detect. Ironically, this is also the exact reason they are interesting to astronomers. Whereas cosmic rays are deflected by magnetic fields and γ-rays absorbed by dust, neutrinos pass these obstacles unhindered, allowing to probe otherwise unreachable regions of the universe.

The goal of this chapter is not to give a thorough introduction to the field of neutrino astronomy, as it is not the topic of this thesis, but rather a short summary intended as motivation for it. A detailed description of the subject is given, for example, by Spurio et al. [2]. We assume the reader is familiar with neutrinos, at least at a fundamental level and start right off with a brief summary of neutrino sources relevant to the corresponding astronomy, followed by an overview of the working principles of neutrino telescopes. We conclude with an introduction to P-ONE as a concrete instance of neutrino telescope, as it is also the target application of this thesis.

[2]: Spurio (2014), *Particles and Astrophysics*

2.1 Neutrino Sources

Vitagliano et al. [15] gave an excellent review of neutrino sources producing fluxes dominant at earth compiled into the *grand unified neutrino spectrum* (GUNS) covering energies from meV up to PeV, as shown in

[15]: Vitagliano et al. (2020), 'Grand unified neutrino spectrum at Earth: Sources and spectral components'

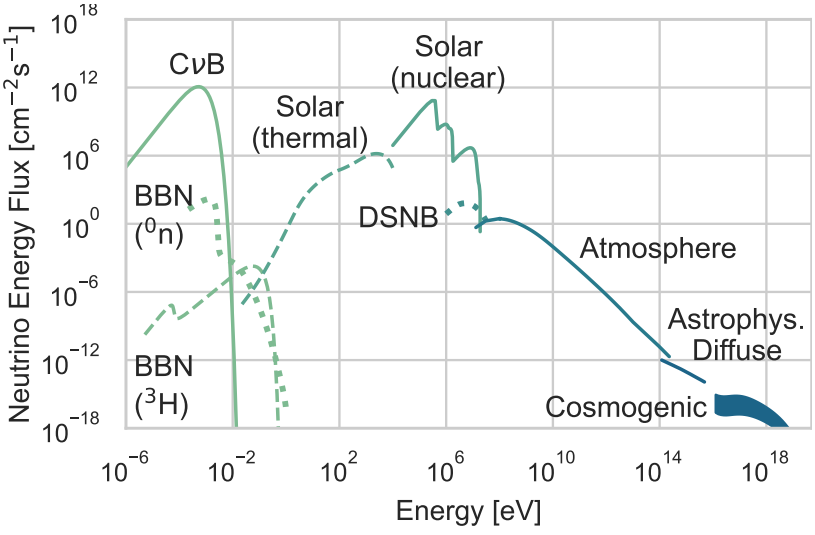

Figure 2.1: Subset of the Grand Unified Neutrino Spectrum (GUNS) containing only the astrophysical sources including the cosmic neutrino background (CνB), decay of elements created in the big bang nucleosynthesis (BBN) and the diffuse supernova neutrino background (DSNB). Created from data provided by Vitagliano et al.[15]

Figure 2.1. To make this chapter self-contained, a very brief summary of the astronomical sources presented in the aforementioned paper is in the following given without going into the details of their corresponding physical model.

Early Universe

The low energy end of the spectrum ($\lesssim 1\,\mathrm{eV}$) is dominated by processes dating back to the early universe, namely the *cosmic neutrino background* (CνB) and the decaying of unstable elements produced in the *Big Bang Nucleosynthesis* (BBN). The CνB is similar to the cosmic microwave background (CMB) consisting of neutrinos that froze out roughly 1 s after the big bang and thus much earlier than the photons of the CMB (∼400 000 yr [16]). After red-shifting to lower energies due to the universe's expansion, today its density is expected to be around $112\,\mathrm{cm}^{-3}$. Radioactive decay after the BBN of mainly free neutrons and tritium produced fewer neutrinos, but these are younger and thus experienced less red shift, allowing them to become dominant at energies above the CνB.

[16]: Bartelmann (2012), 'Development of Cosmology: From a Static Universe to Accelerated Expansion'

Solar Processes

The Sun, due to its proximity to earth, dominates the intermediate energy ranges (eV to MeV) with neutrinos produced by either nuclear or thermal processes. The former consists of various reaction chains fusing four protons into a single helium nucleus while releasing two electron neutrinos. However, we expect a mixture of all three flavors due to flavor oscillations at earth. In contrast to that, thermal processes such as Compton, plasmon decay and bremsstrahlung produce not only neutrinos of all flavors but also anti-neutrinos.

Supernovae

While supernova explosions (SN) in our proximity are a highly anticipated event releasing massive amounts of energy in mostly neutrinos during the span of a few seconds, it is a transient signal and thus technically not part of the neutrino spectrum. However, since we expect a few SN per second in the observable universe, their signals combine into the *diffuse supernova neutrino background* (DSNB) dominating between 10 and 25 MeV.

Atmosphere

In Earth's atmosphere, neutrinos are produced as the nuclei it consists of interact with the charged particles from cosmic rays mainly due to the creation and decaying of kaon ($K \to \mu + \nu_\mu$) and pions ($\pi \to \mu + \nu_\mu$) as well as the subsequently created muons ($\mu \to e + \nu_e$).[1] For energies up to 10^{20} eV, one expects a ratio between electron and muon neutrinos of $\nu_\mu/\nu_e \simeq 2$, whereas for higher energies ν_μ dominates.

1: For better readability, we dropped the notation of (anti)matter.

High Energy Neutrino Sources

At high energies (TeV to PeV), neutrinos are produced by the interaction of cosmic rays as they propagate to the Earth or already within their sources through e.g. proton-proton or proton-photon ($p + \gamma \rightarrow \Delta \rightarrow n + \pi^+$; $p + \gamma \rightarrow K^+ + \Lambda/\Sigma$) reactions similar in principle to the generation of atmospheric neutrinos as decay products of mainly muons and kaons. Most neutrinos at these energies are expected to originate from outside our galaxies. Among the cosmic ray sources, the most promising ones for neutrino production are active galactic nuclei (AGN), gamma-ray bursts (GRB) and star-forming galaxies (SFG). However, so far, only for AGNs exist known associations, making them currently the most popular in neutrino astronomy. Alternatively, the cosmic rays of the highest possible energy (up to 1×10^{20} eV), so-called ultra-high-energy cosmic rays (UHECR), can interact with photons dispersed in the universe, such as the CMB either via photodisintegration or photo-pion interactions creating unstable products. The neutrinos produced by their decay are called *cosmogenic* neutrinos. This process strongly suppresses the flux of UHECR, creating a feature in their spectrum known as the *Greisen-Zatsepin-Kuzmin* (GZK) cutoff.

2.2 Neutrino Telescopes

Currently, there are several operational neutrino telescopes such as IceCube at the South Pole [3], KM3NeT in the Mediterranean Sea [5] and Baikal-GVD in Lake Baikal in southeast Russia [6]. New ones complementing them are currently proposed or in development, including P-ONE [10]. The distinguishing characteristic separating them from other neutrino detectors is the capability to reconstruct tracks with a resolution much better than 1° [2].

[3]: Karle et al. (2003), 'IceCube — the next generation neutrino telescope at the South Pole'

[5]: Katz (2006), 'KM3NeT: Towards a km3 Mediterranean neutrino telescope'

[6]: Avrorin et al. (2022), 'Deep-Underwater Cherenkov Detector in Lake Baikal'

[10]: Agostini et al. (2020), 'The Pacific Ocean Neutrino Experiment'

This section aims to introduce the physical concepts describing the detection of neutrinos, as well as the working principle of neutrino telescopes, including their design requirements and the challenges they are facing.

[2]: Spurio (2014), *Particles and Astrophysics*

2.2.1 Neutrino Interactions

Neutrinos interact hardly with matter and only via the weak force. Whereas at 1 TeV, γ-rays show a mean free path in water of $\lambda \approx 42$ m, for neutrinos it is $\lambda \approx 2 \times 10^9$ m. At roughly 200 TeV, their mean free path is about the same as earth's diameter [2]. Figure 2.2 shows a plot of the corresponding cross sections. The most important channels are the neutral current (NC, Equation 2.1a) and charged current (CC, Equation 2.1b):

$$\nu_l + N \rightarrow \nu_l + X \tag{2.1a}$$

$$\nu_l + N \rightarrow l + X \tag{2.1b}$$

where $l = e, \mu, \tau$ stands for the lepton flavour and X for secondary particles [2]. Alternatively, at around 6.3 PeV, there is a resonance for the production of W^- bosons via a pair of an electron and anti-electron neutrino predicted by Glashow [17] (thus known as *Glashow resonance*)

[17]: Glashow (1960), 'Resonant Scattering of Antineutrinos'

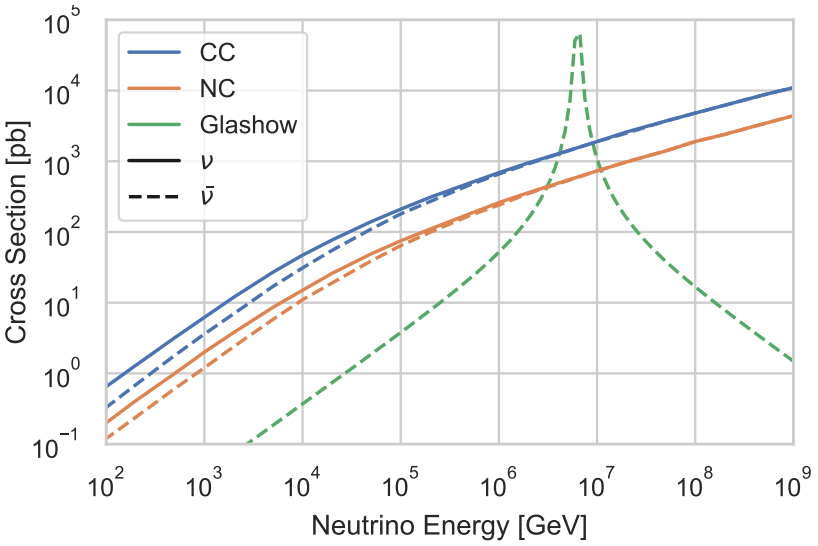

Figure 2.2: Cross sections for interactions of neutrinos with matter via NC and CC [19] as well as the Glasshow resonance [20]. Solid lines refer to neutrinos, dashed to anti-neutrinos.

and first measured by IceCube in 2021 [18]:

$$\bar{\nu}_e + e^- \rightarrow W^- \rightarrow X \tag{2.2}$$

CC and NC interactions, as well as the Glasshow resonance, create hadronic showers. The leptons produced by CC, however, behave differently depending on their flavor: Electrons create additional electromagnetic shower. Similarly, tau leptons travel a short distance and induce a second hadronic shower as they decay, which is called a *double bang* signal. Muons, on the other hand, travel for a long distance, manifesting in a track signal, which allows a more precise direction estimate and can even be detected if the event happens outside the detector volume [2]. Figure 2.3 shows an illustration.

Neither hadronic showers nor leptons are directly measured by neutrino telescopes. Instead, one relies on the light they produce via Cherenkov radiation, whose working mechanism is explained in the following section.

2.2.2 Cherenkov Radiation

In 1934, Cherenkov [21] published a paper after carrying out various experiments to determine the cause of blue light emitted by transparent objects under certain radiation. This effect is now known as *Cherenkov radiation*. He concluded that it is not caused by luminescence as previously believed, but rather fast charged particle, a result Frank and Tamm [22] derived mathematically using classic theory of electromagnetism. Their work was honored in 1958 when they received the Nobel Prize [23, 24].

[18]: Aartsen et al. (2021), 'Detection of a particle shower at the Glashow resonance with IceCube'

[19]: Cooper-Sarkar et al. (2011), 'The high energy neutrino cross-section in the Standard Model and its uncertainty'

[20]: Barger et al. (2014), 'Glashow resonance as a window into cosmic neutrino sources'

[2]: Spurio (2014), *Particles and Astrophysics*

[21]: Cherenkov (1934), 'Visible luminescence of pure liquids under the influence of γ-radiation'

[22]: Frank et al. (1937), 'Coherent visible radiation of fast electrons passing through matter'

[23]: Katz (2020), 'Cherenkov light imaging in astroparticle physics'

[24]: Jelley (1955), 'Cerenkov radiation and its applications'

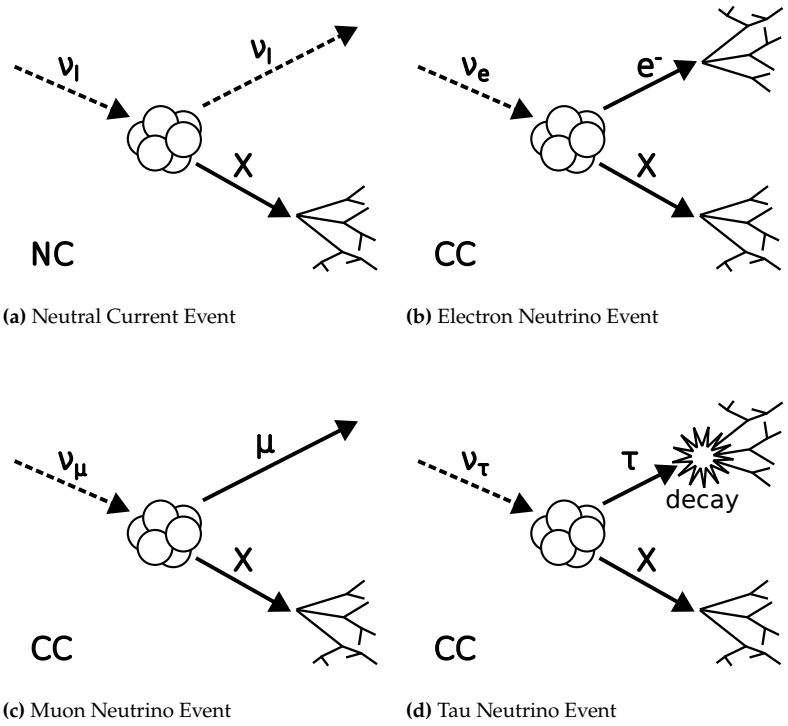

(a) Neutral Current Event

(b) Electron Neutrino Event

(c) Muon Neutrino Event

(d) Tau Neutrino Event

Figure 2.3: Illustration of the different neutrino interactions with mater via neutral current (NC) and charged current (CC). Electrons produce electromagnetic, secondary particles (X) hadronic showers. Solid lines create Cherenkov radiation, dashed ones not.

When charged particles travel through a dielectric, they polarize it locally. Due to symmetry, the electric field cancels out at large distances and no radiation is created: The induced wavelets at the atoms interfere destructively. If, however, the speed of the particle exceeds the phase speed of light in that medium,[2] its atoms can no longer keep up with the polarization, allowing for constructive interference of the wavelets, producing a light cone as shown in Figure 2.4 with an opening angle given by the *Cherenkov relation*

$$\cos\theta = \frac{c}{vn} \tag{2.3}$$

where v is the particle's speed and n the refractive index of the medium. Therefore, if n varies for different wavelengths, the corresponding radiation can be observed under distinct angles. For high energetic particles ($v \approx c$) in water ($n \approx 1.33$ [25]), for example, one observes light at $\theta \approx 41°$. In addition, the light is completely linearly polarized with their electric field lying in the plane spanned by the propagation direction of the particle and photon [24].

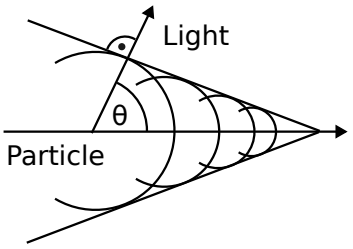

Figure 2.4: Construction of the Cherenkov cone using Huygens principle. Center of spherical wavelets travel with the particle's speed whereas their radii grow slower at the medium's phase velocity.

2: See Section 3.2.

[25]: Millard et al. (1990), 'An index of refraction algorithm for seawater over temperature, pressure, salinity, density, and wavelength'

[24]: Jelley (1955), 'Cerenkov radiation and its applications'

The spectral distribution energy or number of photons emitted via Cherenkov radiation per distance traveled is given by the *Frank-Tamm formula* [26]:

$$\frac{\partial^2 Q}{\partial x \partial \lambda} = \pi c^2 e^2 \mu_o \frac{1}{\lambda^3}\left(1 - \frac{1}{\beta^2 n^2(\lambda)}\right) \tag{2.4a}$$

$$\frac{\partial^2 N}{\partial x \partial \lambda} = 2\pi\alpha \frac{1}{\lambda^2}\left(1 - \frac{1}{\beta^2 n^2(\lambda)}\right) \tag{2.4b}$$

where $\alpha \approx 1/137$ is the fine-structure constant and μ_0 the magnetic permeability of vacuum.[3] The number of emitted photons scales inversely

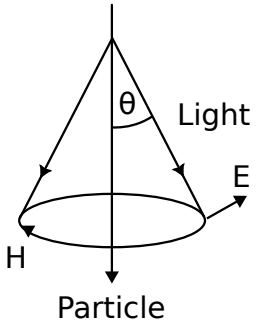

Figure 2.5: Illustration of the Cherenkov cone including its polarization. The electric field is normal to the cone surface, the magnetic field tangential. Adapted from [24].

with λ^{-2}. Most photons are thus emitted at shorter wavelengths. While integrating these formulas λ has to be limited to the range where the condition $v > c/n(\lambda)$ is fulfilled. Water, for instance, has minimal attenuation between 300 nm and 600 nm [27] where we expect a high energetic particle to produce roughly 3.5×10^4 photons per meter.

Finally, we want to convert the Frank-Tamm formula to give radiance instead. We assume the Cherenkov radiation at a given position along the track to be a perfect pulse thus the derivation after time gives a Dirac delta. Next, we note that a surface element $\mathrm{d}A$ on the cone of the wavefront that has already traveled a distance r from its origin is given by $\mathrm{d}A = \sin\theta\pi r\mathrm{d}A\mathrm{d}\phi$. Thus, the radiance emitted by Cherenkov radiation is

$$L = \frac{\partial Q}{\partial t \partial A \partial \omega \partial \lambda} = \frac{1}{\sin\theta\pi r}\frac{1}{2\pi}\frac{\partial Q}{\partial x \partial \lambda}\delta(\omega - \omega_c)\delta(t - t_c) \tag{2.5}$$

where the Dirac delta defines the light pulse and Cherenkov cone respectively. Notable here is that radiance shrinks only with r^{-1} and not r^{-2} as one would expect for isotropic light sources.

2.2.3 Neutrino Telescope Characteristics

Considering the abysmal low cross sections shown in Figure 2.2, it is evident that in order to have any real chance of detecting a neutrino signal, one needs accordingly large detector volumes. A characteristic parameter trying to express a detector's performance using a single number is the *effective area*, resembling the surface area a perfect detector[4] of equivalent performance would have. The expected signal rate is simply the product of particle flux and effective area [28]. IceCube, in its IC79 configuration, for instance, states at 100 TeV an effective area of ~80 m^2 [29]. Combining this with the expected neutrino flux at that energy from the GUNS [15], one thus expects ≈ 15 events per year for that specific energy. This shows that while IceCube's detector volume of 1 km^3 [3] seems impressive, it is actually at the lower end necessary for neutrino telescopes to be viable.

Due to the large detector volumes in neutrino telescopes, the individual detector modules they consist of tend to be separated at rather large distances. In KM3NeT, these modules are attached to strings separated by 90 m to 100 m, with 36 m between modules [30]. At the detector's site Riccobene et al. [31] determined an attenuation coefficient of 0.0355 m^{-1} at $\lambda = 440\,\mathrm{nm}$, resulting in a minimal attenuation of ~ 70% between modules and ~ 96% between strings. From the initial thousands of Cherenkov photons, only a few make it to modules. To still be sensitive to them one usually uses *photo multiplier tubes* (PMT) [2].

The faint signals in neutrino telescope caused by neutrinos are easily overwhelmed by background noise caused by mainly atmospheric muons traveling several kilometers in water and ice, indicating the need for considerable shielding. Usually, this is realized by locating the telescope deep below the Earth's surface, which is favorable in the deep ocean or ice. Additional background in water is the radioactive decay of ^{40}K and bioluminescence.[5] Since neutrinos hardly interact with matter, neutrino telescopes are also sensitive to signals from the opposite hemisphere,[6] giving them essentially the entire Earth as shielding from that direction [2].

[26]: Curtis D. Mobley (2022), *The Oceanic Optics Book*

3: We assumed $\mu \approx \mu_0$ which holds for many materials including water.

[27]: Smith et al. (1981), 'Optical Properties of the clearest natural waters (200-800 nm)'

4: Pefect in the sense that it detects every particle it encounters.

[28]: Heros (2020), *Probing Particle Physics with Neutrino Telescopes*

[29]: Aartsen et al. (2013), 'Search for time-independent neutrino emission from astrophysical sources with 3 years of IceCube data'

[15]: Vitagliano et al. (2020), 'Grand unified neutrino spectrum at Earth: Sources and spectral components'

[3]: Karle et al. (2003), 'IceCube — the next generation neutrino telescope at the South Pole'

[30]: Margiotta (2014), 'The KM3NeT deep-sea neutrino telescope'

[31]: Riccobene et al. (2007), 'Deep seawater inherent optical properties in the Southern Ionian Sea'

[2]: Spurio (2014), *Particles and Astrophysics*

5: Especially deep ice is much more radio pure.

6: As the cross section of neutrino interactions increase with Energy, at 200 TeV the interaction length is equal to Earth's diameter putting a soft limit on this approach.

Figure 2.6: Map showing the planned location of P-ONE in the Cascadia Basin off the shore of Vancouver Island in Canada. The neutrino telescope will be deployed at a depth of 2660 m [10]. Map published under the CC BY 4.0 DEED license [33].
Data: © OpenStreetMap contributors, SRTM, GEBCO, SONNY's LiDAR DTM, NASADEM, ESA WorldCover; Maps © Tracestrack

[33]: OpenStreetMap contributors (2024), *OpenStreetMap*

2.3 P-ONE

As the Pacific Ocean Neutrino Experiment (P-ONE) is the intended application of the simulation developed in this work, we want to give a brief overview of it. The following summarizes the more detailed description by Agostini et al. [10], Henningsen et al. [32] and Malecki et al. [11].

[10]: Agostini et al. (2020), 'The Pacific Ocean Neutrino Experiment'

[32]: Henningsen (2023), 'Pacific Ocean Neutrino Experiment: Expected performance of the first cluster of strings'

[11]: Malecki (2024), 'Pacific Ocean Neutrino Experiment'

Currently under development, P-ONE is a planned multi-cubic-kilometers neutrino telescope operating in the Cascadia Basin near Vancouver Island in Canada at a depth of 2660 m. It aims to complement existing neutrino telescopes by extending the coverage of the observed sky with respect to neutrinos in the Southern Hemisphere. Compared to Antarctic ice using deep ocean water as the detector media, one expects better angular resolution up to sub-degree precision due to the much lower scattering coefficient. Unfortunately, however, it also absorbs light more strongly, making it harder to detect.

The fundamental modules of P-ONE that are responsible for detecting the signals are the *Precision Optical Modules* (P-OM). Each consists of 16 3-inch PMTs coupled to the two enclosing 17-inch glass hemispheres via optical gel pads alongside the necessary electronics for powering and reading them out. A variation to the P-OM also exists called P-CAL, where 8 PMTs were replaced by an isotropic flasher, providing a known light source for calibration purposes and efficiency measurements.

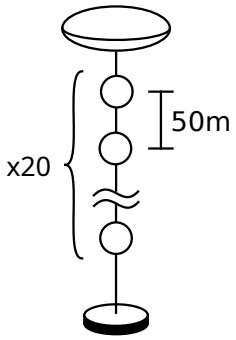

Figure 2.7: Illustration of the proposed string design of P-ONE: 20 modules are placed 50 m apart on a single line, anchored to the sea floor and erected vertically by a floating element.

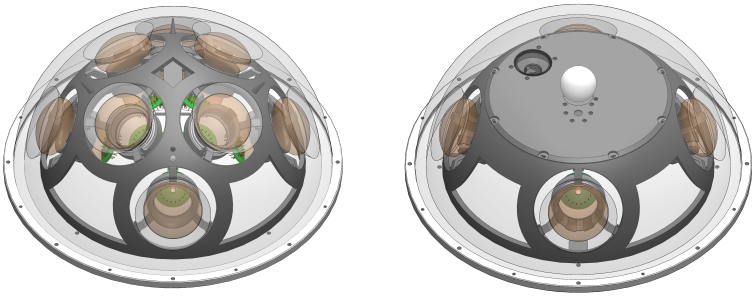

(a) Precision Optical Module (P-OM) **(b)** Calibration Module (P-CAL)

Figure 2.8: Renderings showing the hemispheres of the P-OM and P-CAL modules of P-ONE. Images by courtesy of Christian Spannfellner.

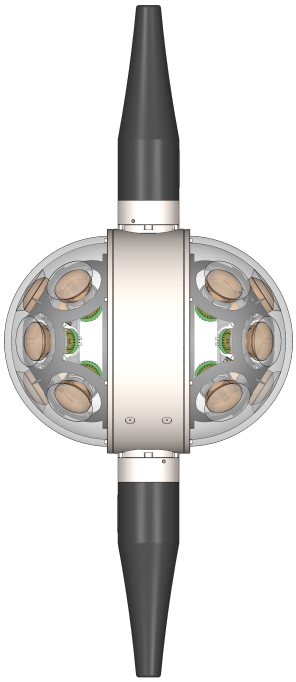

Figure 2.9: Rendering showing a P-OM attached to a string. Image by courtesy of Christian Spannfellner.

To minimize the amount of modules needed, a segmented design is proposed. In its currently proposed configuration, 20 modules[7] with 50 m in between will be installed on a single string, each anchored to the sea floor and vertically erected using a floating device. A group of 10 strings placed 80 m apart and arranged in a circle of 200 m form a *cluster*. Finally, seven of these clusters also form a circle to cover the first cubic kilometer of detector volume. At this point, it should also be mentioned that there is currently an ongoing effort to optimize the detector configuration based on machine learning [34].

The Cascadia Basin was chosen for the location as it already has an existing deep-sea infrastructure operated by Ocean Networks Canada (ONC) that provides power and a high-bandwidth fiber-optic network. The site was investigated by two successful pathfinder missions, STRAW [8] and STRAW-b [9] (*STRings for Absorption in Water*) in 2018 and 2020 respectively, measuring the optical properties of the ocean water located there.[8] Deployment of the actual neutrino telescope is planned to start in 2025.

7: Typically P-OMs, but up to three may be replaced with P-CALs.

[34]: Haack et al. (2023), 'Machine-learning aided detector optimization of the Pacific Ocean Neutrino Experiment'

[8]: Boehmer et al. (2019), 'STRAW (STRings for Absorption length in Water): pathfinder for a neutrino telescope in the deep Pacific Ocean'

[9]: Rea et al. (2021), 'P-ONE second pathfinder mission: STRAW-b'

8: See Subsection 7.2.1 on page 48

Light Model 3

3.1 Radiometric Units 11
3.2 Transient Light Propagation 12
3.3 Refraction in Media 12
3.4 Polarization Effects 13

The backbone of any light simulation is the model used to describe its behavior. Here, we mainly rely on geometric optics, ignoring the wave nature of light and using more fundamental theories only to derive effects, which will be introduced into the model phenomenologically. While these theories may be considered common knowledge among physicists, they still differ in notation between authors. Furthermore, it is a priori not apparent what effects to include, i.e. which ones contribute in a magnitude large enough to be measurable by the experiment. The goal of this chapter is, therefore, to fix notation on the one hand and to estimate which effects to include on the other hand, thus consecutively developing the light model.

3.1 Radiometric Units

Radiometry is the science of measuring electromagnetic radiation.[1] Its fundamentals are relatively intuitive, as the introduction by Mobley [26] shows. Bukshtab [35] conducted a more thorough investigation. Here we are only interested in the radiometric units.

1: Whereas *Photometry* describes how the human eye perceives light.

[26]: Curtis D. Mobley (2022), *The Oceanic Optics Book*

[35]: Bukshatb (2019), *Photometry, Radiometry, and Measurements of Optical Losses*

Starting from the definition of *flux*

$$\Phi = \frac{\mathrm{d}Q}{\mathrm{d}t} \qquad [\mathrm{W}] \tag{3.1}$$

as the change of energy per time one quickly leads to *irradiance*

$$E = \frac{\mathrm{d}\Phi}{\mathrm{d}A_\perp} \qquad \left[\frac{\mathrm{W}}{\mathrm{m}^2}\right] \tag{3.2}$$

intensity

$$I = \frac{\mathrm{d}\Phi}{\mathrm{d}\Omega} \qquad \left[\frac{\mathrm{W}}{\mathrm{sr}}\right] \tag{3.3}$$

and finally *radiance*

$$L = \frac{\mathrm{d}^2\Phi}{\mathrm{d}A_\perp \mathrm{d}\Omega} \qquad \left[\frac{\mathrm{W}}{\mathrm{m}^2\,\mathrm{sr}}\right] \tag{3.4}$$

where $\mathrm{d}A_\perp$ is the projected area perpendicular to the direction of light propagation.

Each of the previous quantities can be further made a function of the wavelength λ.[2] Some authors assign the prefix *spectral* to distinguish them from their original definition. However, since we will only be dealing with (quasi) monochromatic light, this is implicitly assumed in an attempt to not clutter notation.[3] Using spectral quantities further allows us to seamlessly switch units from watts to a photon count by dividing by the energy per photon.

2: λ always refers to the vacuum wavelength.

3: From here on, radiometric quantities are always spectral.

Conservation of energy leads to the conservation of radiance along light rays in vacuum.[4] We therefore will model light as rays carrying radiance.

4: In materia we have to account for scattering and absorption as we will later see.

Using radiance as the fundamental quantity has the additional benefit of automatically taking care of e.g. Lambert's cosine law and the inverse-square law. Both are simple geometric effects handled by the change in differential area $\mathrm{d}A_\perp$. This is especially useful in scenarios where the latter does not apply anymore: As Cherenkov radiation emits light only in constrained directions, the observed irradiance only changes inversely linear in distance.[5] For a description of Cherenkov radiation, see Section 2.2.2.

5: Per particle track length emitted light is constrained on a circle whose circumference grows linear in distance.

3.2 Transient Light Propagation

Starting from Maxwell's equation, one can derive the famous wave equations

$$\nabla^2 \boldsymbol{E} - \frac{\epsilon\mu}{c^2}\ddot{\boldsymbol{E}} = 0 \qquad \nabla^2 \boldsymbol{H} - \frac{\epsilon\mu}{c^2}\ddot{\boldsymbol{H}} = 0 \tag{3.5}$$

describing electromagnetic waves traveling at a constant speed[6]

6: Equation 3.5 describes planar waves. More complex shapes may show different behavior.

$$v_p = \frac{c}{\sqrt{\epsilon\mu}} = \frac{c}{n} \tag{3.6}$$

called the *phase velocity*, where we recognize $n = \sqrt{\epsilon\mu}$ as the *refractive index*.[7] The latter is generally a function of the wavelength known as the *dispersion relation*.

7: Some authors define n to be complex valued. Here it will always be real values.

In nature, one will never observe a perfect monochromatic electromagnetic wave. Indeed, as Fourier's theorem states, this would require the wave to be constant in the time domain, i.e. it has existed forever and will last forever. Instead, one models light rays using *wave packets* consisting of multiple wavelengths in a narrow band centered at λ. After linearization of the dispersion relation, one finds the wave packet to travel with a velocity

$$v_g = v_p - \lambda \frac{\mathrm{d}v_p}{\mathrm{d}\lambda} \tag{3.7}$$

called the *group velocity*[8] [36].

8: This, too, is not generally true, as we linearized the dispersion relation.

[36]: Born et al. (1999), *Principles of Optics*

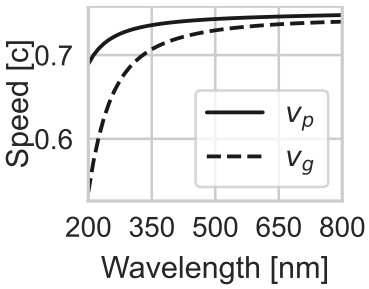

Figure 3.1: Phase and group velocity in units of c for ocean water using the model from Millard, Seavar (1999) [25]. (4.0°C, 1000.0dbar, 35.0 PSU)

[25]: Millard et al. (1990), 'An index of refraction algorithm for seawater over temperature, pressure, salinity, density, and wavelength'

[37]: Withayachumnankul et al. (2010), 'A Systemized View of Superluminal Wave Propagation'

3.3 Refraction in Media

The refractive index in ocean water is not constant but varies with temperature, salinity and pressure, as shown by Millard and Seaver [25].

The *ray equation* than predicts the light path $\boldsymbol{r}(s)$ to be curved [36]:

[36]: Born et al. (1999), *Principles of Optics*

$$\frac{\mathrm{d}}{\mathrm{d}s}\left(n\frac{\mathrm{d}\boldsymbol{r}}{\mathrm{d}s}\right) = \nabla n \tag{3.8}$$

Below depths of roughly 1000 m, one leaves the *thermocline* and reaches the *abyssal*,[9] where temperature and salinity stay practically constant [38]. Since all experiments of interest are well below that threshold, we are left with only depth as a proxy for pressure as a parameter of the refractive index.

9: There are very few isolated deep convection layer reaching depths of 2000 m.

[38]: Talley et al. (2011), *Descriptive Physical Oceanography*

Following the calculation by Robinson et al. [39], we assume the inverse refractive index to be linear in depth. Solving the ray equation results in circular light paths of varying radii depending on the initial angle to the vertical. A linear regression on the inverse refractive index ($1.0 - R^2 < 10^{-5}$) gives us a minimal curvature radius of 1,193 km or roughly a fifth of the Earth's radius. It is, therefore, safe to ignore this effect in the simulation.

[39]: Robinson et al. (2008), *Digital Imaging and Deconvolution: The ABCs of Seismic Exploration and Processing*

3.4 Polarization Effects

According to the Fresnel equation Equations 4.5 and 4.6, the PMTs used in neutrino experiments are by proxy sensitive to polarization as it affects the transmission and reflection of light at the surfaces between photocathode, glass window and surrounding media. Since Cherenkov radiation is linear polarized, as shown in Section 2.2.2, it raises the question of whether it is worthwhile to include this in the simulation.

The effect of polarization on PMT in water was investigated for a single wavelength by Moorhead [40] in his PhD thesis and later extended to a broader spectrum by Motta et al. [41]. While the latter showed that the material of the photocathode is highly dispersive, there is no reason to believe that their measurements are an exact match for the currently produced PMTs, especially since they tested only two specific models. For now we are only interested in determining whether simulating polarization is worthwhile and therefore will only use the results of the original measurement at $\lambda = 442\,\mathrm{nm}$.

[40]: Moorhead (1992), 'Reflectors in Cherenkov Detectors'

[41]: Motta et al. (2005), 'Optical properties of bialkali photocathodes'

Both of the above-mentioned works model the PMT as layers of different media consisting of the outer media, i.e. water or air, followed by glass, the photocathode and finally the vacuum inside. The photocathode is the only absorbing layer and due to its thickness, different orders of reflected light rays inside it interfere with each other. A schematic of this is shown in Figure 3.2.

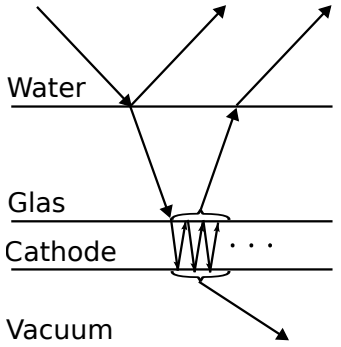

Figure 3.2: The model used by Moorhead [40] to describe the optical properties of a PMT using layers of different media. Considers for reflections first and second order, for transmission only the first. Additionally, it treats the photocathode as a thin layer, allowing for interference between different orders of reflection.

Characteristics of PMTs are usually measured for operation in air [42]. However, these depend on the surrounding media and thus differ in water for two reasons: On the one hand, there is the obvious dependency of the Fresnel equation at the outer interface on the surrounding refractive index, but there is also a more subtle one: Due to its higher refractive index water refracts light less as it enters the PMT's glass housing causing it to hit the photocathode at larger angles. This enables effects such as total internal reflection at its interface to the internal vacuum as shown

[42]: Hamamatsu Photonics K. K. (2017), *Photomultiplier Tubes*

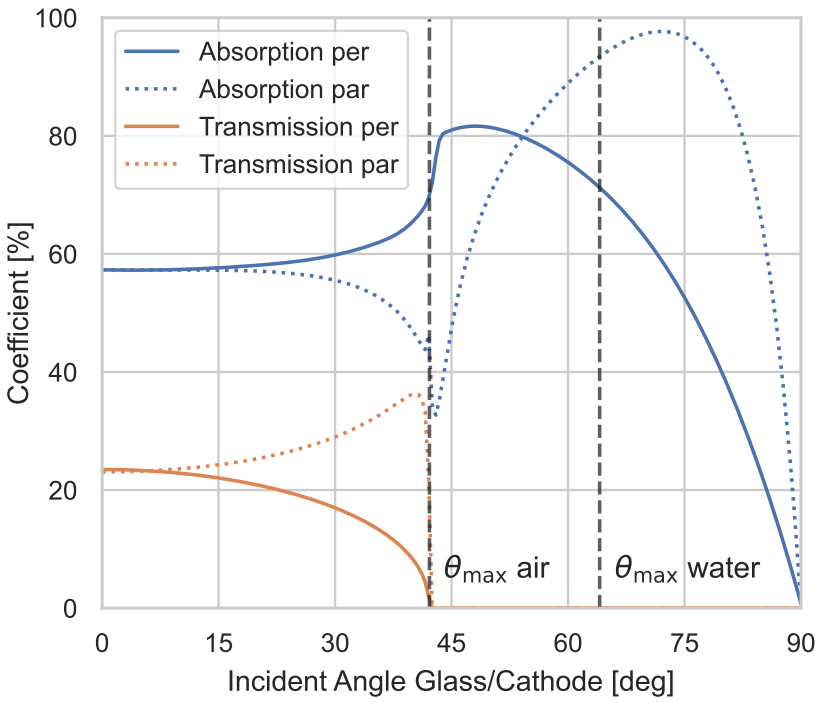

Figure 3.3: Absorption and transmission coefficients of parallel and perpendicular polarized light at the glass-photocathode interface present in PMTs for $\lambda = 442\,\text{nm}$. Reproduced from Moorhead [40]. Additionally, it includes the maximum angle of light refracted onto the interface originating from water and air.

[40]: Moorhead (1992), 'Reflectors in Cherenkov Detectors'

in Figure 3.3. Combining these effects, one can model the PMT's overall behavior.

Figure 3.4 compares the PMT model for air and water, while Figure 3.5 additionally includes a cosine factor to take the change in apparent area into account. While air shows no deviation from unpolarized light, there is a strong dependency on polarization for water, especially between 45° and 60°. These angles correspond to the separation between PMTs when distributing 6 to 8 along a circle, similar to the proposed detector modules for P-ONE.[10] The difference in signals between these PMTs in such configurations when hit by a linear polarized light front thus depends on the polarization's orientation. Usually, the PMTs are aligned alongside multiple circles, allowing in theory to deduce the light's polarization.[11]

In the end, however, it is unclear whether the polarization of the Cherenkov radiation remains sufficiently high enough until it reaches the detector and whether the effect on the PMT is strong enough to be measurable, especially considering uncertainties in the simulation. This will be investigated in Section 7.2.3. The underlying physical model to describe the propagation of polarization and its interaction with media is introduced in Chapter 5.

10: See Section 2.3 on page 9

11: We want to stress again that this result was deduced using a model for a specific type and model of a PMT at a single wavelength. To give a definitive estimate for an experiment, a better understanding of the PMTs it uses is necessary.

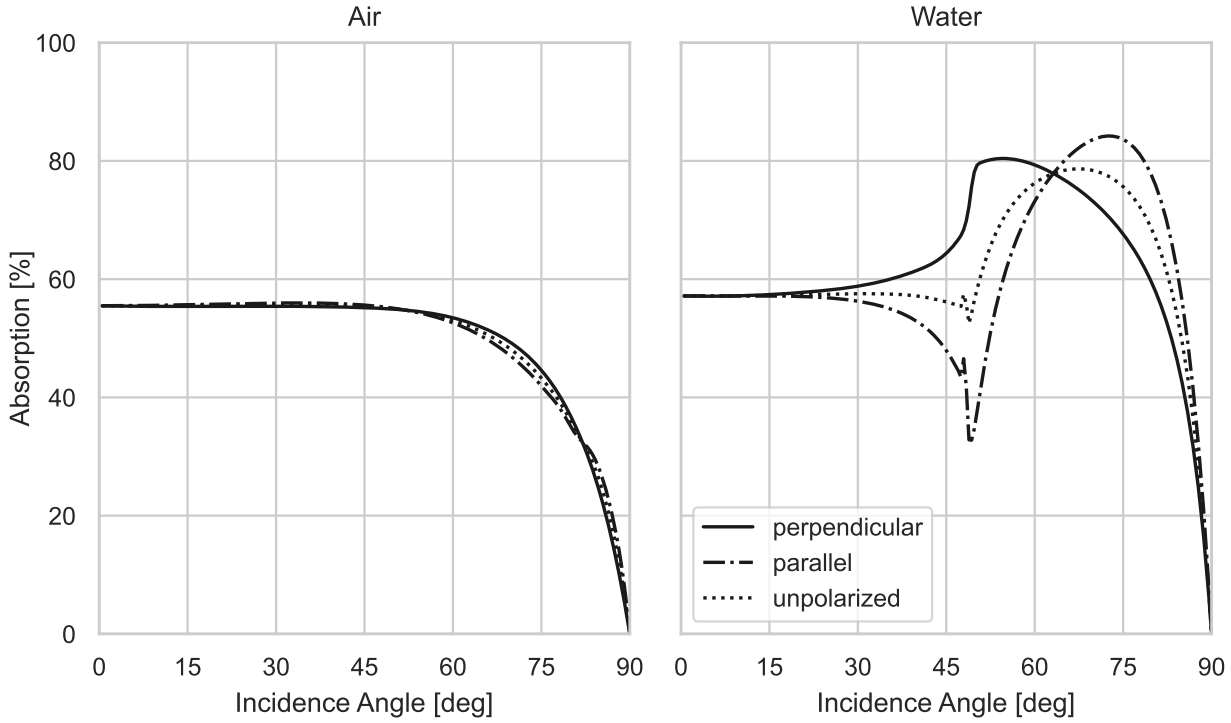

Figure 3.4: Absorption coefficients of the photocathode in PMTs for polarized light at $\lambda = 442\,\text{nm}$, comparing different behavior between PMTs placed in air and water using the model introduced by Moorhead [40].

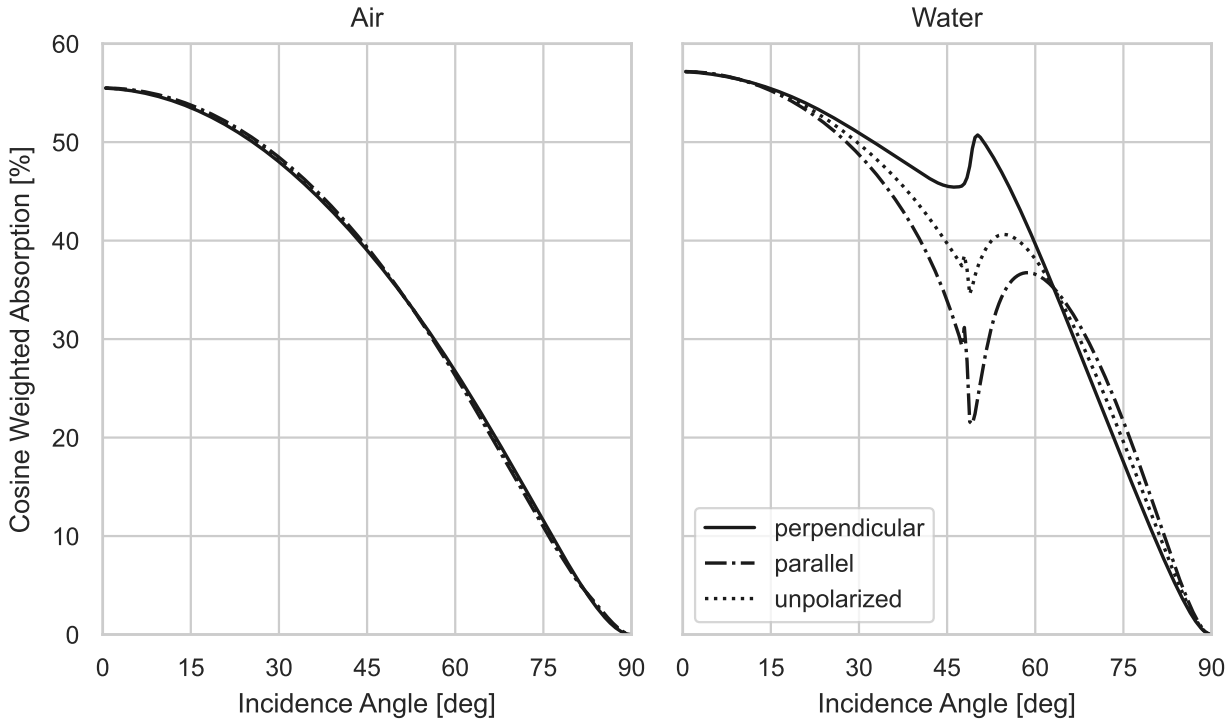

Figure 3.5: Cosine weighted version of Figure 3.4 to account for the change in apparent area. Shows a comparison of the absorption coefficient of the photocathode for PMTs placed in air and water at a wavelength $\lambda = 442\,\text{nm}$. Based on the model introduced by Moorhead [40].

Light Interaction with Media

4

4.1 At Interfaces 17
4.2 Absorption 19
4.3 Elastic Scattering 20
4.4 Inelastic Scattering 22
4.5 Equation of Transfer 23

As light travels through media, it can interact with it by either being absorbed or scattered. Additionally, rays are partially reflected and refracted at interfaces between media of different refractive indices. The physical laws governing these events are introduced in this chapter. We assume media to be homogeneous, i.e. interactions do not depend on its location. This is reasonable for the scenario we are interested in and makes the models and thus calculations much easier to compute.

Water is, of course, of special interest here as it surrounds our experiment. Unfortunately, especially for deep ocean seawater, there are not that many measurements, with Petzold being a noteworthy example [43]. Although only at a single wavelength, for pure seawater, which only contains little to no particles, there are the measurements by Smith [27]. Since water has a high variability in its optical properties depending on its constituents, the latter is hardly usable on its own for natural waters.

[43]: Petzold (1972), *Volume Scattering Functions for Selected Ocean Waters*

[27]: Smith et al. (1981), 'Optical Properties of the clearest natural waters (200-800 nm)'

There exist models that will allow us to extrapolate these measurements, but these are still only a necessary substitution and should ideally be replaced by actual in situ measurements. For deep ocean water, we expect no chlorophyll as its concentration shrinks to practically zero much earlier due to the lack of sunlight [44], making some models a bit easier.

[44]: Zhou et al. (2021), 'Feeding Ecology of Three Euphausiid Species in the North Pacific Ocean Inferred From 18S V9 Metabarcoding and Stable Isotope Analysis'

4.1 At Interfaces

The laws responsible for interactions between light and media interfaces are commonly known and restated here for completeness' sake. As incident light traveling in unit direction $\boldsymbol{i}$ encounters a surface with unit normal $\boldsymbol{n}$ pointing towards the light ray separating the current media with a refractive index of n_i from a different media with a refractive index of n_t, it gets both reflected in direction $\boldsymbol{r}$ as well as refracted (transmitted) in direction $\boldsymbol{t}$ as stated by the *law of reflection* (4.1) and *Snell's law* (4.2) respectively, which are listed in the following in their vector form:

$$\boldsymbol{r} = \boldsymbol{i} - 2(\boldsymbol{n} \cdot \boldsymbol{i})\boldsymbol{n} \tag{4.1}$$

$$\boldsymbol{t} = \eta \boldsymbol{i} - \left(\eta(\boldsymbol{n} \cdot \boldsymbol{i}) + \sqrt{k}\right)\boldsymbol{n} \tag{4.2}$$

where

$$\eta = n_i / n_t \qquad k = 1 - \eta^2 \left(1 - (\boldsymbol{i} \cdot \boldsymbol{i})^2\right) \tag{4.3}$$

For $k < 0$ *total reflection* occurs, and no light is refracted [26, 45].

[26]: Curtis D. Mobley (2022), *The Oceanic Optics Book*
[45]: Kessenich et al. (2023), *The OpenGL®Shading Language, Version 4.60.8*

Alternatively, using $\cos\theta_i = \boldsymbol{i} \cdot \boldsymbol{n}$ and $\cos\theta_t = -\boldsymbol{t} \cdot \boldsymbol{n}$, one can write Snell's law in its classic form:

$$\sin\theta_i n_i = \sin\theta_t n_t \tag{4.4}$$

The fraction of the reflected r and refracted t amplitude of the electromagnetic wave can be determined using *Fresnel formulae* for each

polarization component, where the subscript $\perp$ denotes the component perpendicular and subscript $\parallel$ the component parallel to the plane of incidence:

$$\begin{cases} r_{\parallel} = \dfrac{n_t \cos\theta_i - n_i \cos\theta_t}{n_i \cos\theta_t + n_t \cos\theta_i} \\ r_{\perp} = \dfrac{n_i \cos\theta_i - n_t \cos\theta_t}{n_i \cos\theta_i + n_t \cos\theta_t} \end{cases} \tag{4.5}$$

$$\begin{cases} t_{\parallel} = \dfrac{2n_i \cos\theta_i}{n_i \cos\theta_t + n_t \cos\theta_i} \\ t_{\perp} = \dfrac{2n_i \cos\theta_i}{n_i \cos\theta_i + n_t \cos\theta_t} \end{cases} \tag{4.6}$$

[36]: Born et al. (1999), *Principles of Optics*

For unpolarized light, one can use these formulae to obtain the *reflectivity* and *transmissivity* [36]:

$$R = \frac{1}{2}(r_{\parallel}^2 + r_{\perp}^2) \tag{4.7}$$

$$T = 1 - R \tag{4.8}$$

Finally, since refraction changes the amount of solid angle rays are distributed over, figuratively speaking changing the density of rays, for refracted radiance we need to carry an additional factor [46]:

$$L_t = \frac{n_t^2}{n_i^2} T L_i \tag{4.9}$$

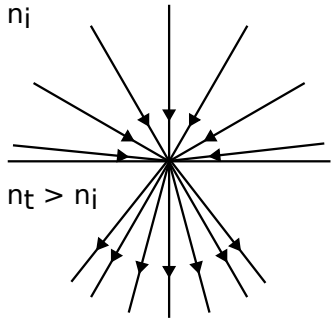

Figure 4.1: Refraction of light rays into a denser medium compresses the same amount of energy into a shallower solid angle.

Materials in the real world rarely show perfect specular reflection and transmission as predicted by the Fresnel terms. Although we mainly deal with glass, which shows such a behavior, we still want to introduce the models used to describe arbitrary materials. Nicodemus et al. [47] defined the relation f_r between incident irradiance E_i and reflected radiance L_r called the *bidirectional reflectance distribution function* (BRDF)[1]:

$$f_r(\boldsymbol{\omega}_i, \boldsymbol{\omega}_r) = \frac{\mathrm{d}L_r(\boldsymbol{\omega}_r)}{\mathrm{d}E_i(\boldsymbol{\omega}_i)} = \frac{\mathrm{d}L_r(\boldsymbol{\omega}_r)}{L_i(\boldsymbol{\omega}_i)\cos\theta_i \mathrm{d}\boldsymbol{\omega}_i} \tag{4.10}$$

[47]: Nicodemus et al. (1977), *Geometrical Considerations and Nomenclature for Reflectance*

1: We deviate from the original notation and follow Pharr et al. [46]

[46]: Pharr et al. (2023), *Physically based rendering*

[48]: Finck et al. (2015), 'Parallelized multichannel BSDF measurements'

[49]: Ngan et al. (2005), 'Experimental Analysis of BRDF Models'

Analogously, one can define the *bidirectional transmission distribution function* (BTDF) f_t. Each distribution function is responsible for a different hemisphere defined by the surface normal, allowing us to combine them into the *bidirectional scatter distribution function* (BSDF) f. In its simplest form, it only depends on the incident and scattered angles, but may also depend on e.g. position, wavelength or polarization and thus capture complex effects like anisotropy or interferences in thin films. While there exist analytical models to describe common BSDF, it still requires a considerable effort to measure them prior to fitting [46, 48, 49].

Using the definition of the BSDF and the conservation of energy, one can derive a corresponding representation for specular transmission and reflection [46]:

$$\begin{aligned} \mathrm{d}L_o(\boldsymbol{\omega}_o) &= f(\boldsymbol{\omega}_o, \boldsymbol{\omega}_i) L_i(\boldsymbol{\omega}_i) |\cos\theta_i| \mathrm{d}\boldsymbol{\omega}_i \\ &= \left[R\delta(\boldsymbol{\omega}_o - \boldsymbol{r}(\boldsymbol{\omega}_i)) + \frac{n_t^2}{n_i^2} T\delta(\boldsymbol{\omega}_o - \boldsymbol{t}(\boldsymbol{\omega}_i)) \right] L_i(\boldsymbol{\omega}_i) \mathrm{d}\boldsymbol{\omega}_i \end{aligned} \tag{4.11}$$

$$f(\boldsymbol{\omega}_o, \boldsymbol{\omega}_i) = R\frac{\delta(\boldsymbol{r}(\boldsymbol{\omega}_i) - \boldsymbol{\omega}_o)}{|\cos\theta_r|} + \frac{n_t^2}{n_i^2} T\frac{\delta(\boldsymbol{t}(\boldsymbol{\omega}_i) - \boldsymbol{\omega}_o)}{|\cos\theta_t|} \tag{4.12}$$

While it may seem superfluous to introduce a new formalism only to end up where we started, we still wanted to show how to proceed when one wants to include more complex interface interactions than specular ones. For this reason, we will also use the BSDF in the simulation algorithm instead of the Fresnel terms.

4.2 Absorption

Absorption is the most basic interaction possible inside a medium. Radiance gets attenuated as part of its energy is absorbed, or equivalently, in the particle picture, photons are absorbed by chance as they travel through the media. Both pictures result in the same equation known as the *Beer-Lambert law*:

$$L = L_0 \exp\left(-\mu_a(\lambda) \cdot d\right) \tag{4.13}$$

where $\mu_a(\lambda)[\mathrm{m}^{-1}]$ [2] is the *absorption coefficient* as function of wavelength and d the distance traveled inside the medium.

2: Some authors use $a(\lambda)$ instead.

Instead of μ_a, some authors indicate the absorption capability of a media via a complex refractive index $n^* = n + i\kappa$. Starting from the wave equation of Maxwell's equation Equation 3.5, on can easily verify the following relation [26]:

$$\mu_a = \frac{4\pi\kappa}{\lambda} \tag{4.14}$$

[26]: Curtis D. Mobley (2022), *The Oceanic Optics Book*

To model more complex media like seawater, it is often useful to split

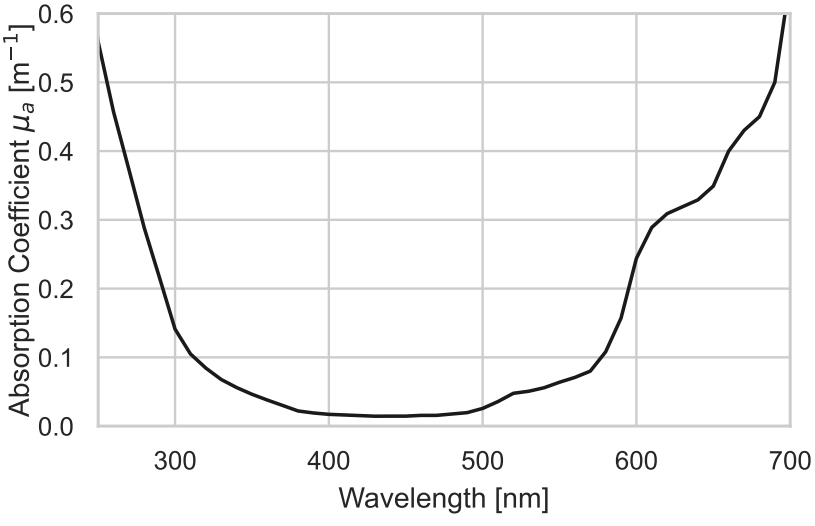

Figure 4.2: Absorption coefficient μ_a of pure water as measured by Smith [27].

[27]: Smith et al. (1981), 'Optical Properties of the clearest natural waters (200-800 nm)'

the total absorption coefficient into a sum of the contribution of pure seawater and its constituents such as chlorophyll, dissolved organic matter or detritus. One could, therefore, write the total absorption coefficient as

$$\mu_{a,\text{total}} = \mu_{a,\text{water}} + \mu_{a,\text{chl}} + \mu_{a,\text{DOM}} + \mu_{a,\text{det}} \tag{4.15}$$

where, as mentioned earlier, $\mu_{a,\text{water}}$ can be taken from Smith's measurement and the chlorophyll's to be zero. The remaining ones can be modeled using the following equation [50]:

$$\mu_{a,i} = \mu_{a,i}(\lambda_0) \cdot \exp[-S_i \cdot (\lambda - \lambda_0)] \tag{4.16}$$

[50]: Mobley (1994), *Light and Water*

4.3 Elastic Scattering

As photons travel through media, they may change their direction as they interact with it. If the photon still has the same energy after scattering, it is called *elastic*. In the radiance picture, this manifests in the overall available energy not decreasing. Since this is like absorption, a probabilistic process, it is similarly parameterized by a *scattering coefficient* $\mu_s(\lambda)[\text{m}^{-1}]$.[3] Complementary, the *phase function* $\tilde{\beta}(\theta)[\text{sr}^{-1}]$ describes the angular distribution of scattered light, where θ is the angle between the incident and scattered direction.[4] These two can be multiplied to obtain the *Volume Scattering Function* (VSF) $\beta(\theta, \lambda)[\text{m}^{-1}\,\text{sr}^{-1}]$.

3: Some authors use $b(\lambda)$ instead.

4: We only model isotropic media. For anisotropic ones, $\tilde{\beta}$ depends on both direction.

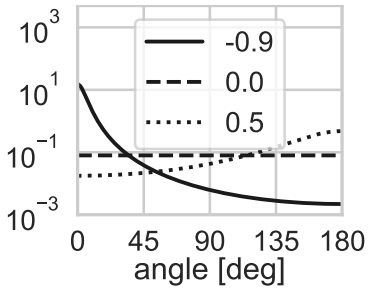

Figure 4.3: Plot of the Henyey-Greenstein phase function for different asymmetry parameter g.

There are multiple analytic models of the phase function, where the most widely known is the *Henyey-Greenstein* phase function [51]:

$$\tilde{\beta}_{\text{HG}}(\theta) = \frac{1}{4\pi} \frac{1 - g^2}{(1 + g^2 - 2g\cos\theta)^{3/2}} \tag{4.17}$$

parameterized by its *asymmetry parameter* g. While being mathematically easy may have contributed to its popularity, it was originally developed to model interstellar dust and thus might not fit the data well. Some authors try to mitigate this by linear interpolating between two versions of the phase function with different asymmetry parameters [26].

[51]: Henyey et al. (1941), 'Diffuse radiation in the Galaxy.'

[26]: Curtis D. Mobley (2022), *The Oceanic Optics Book*

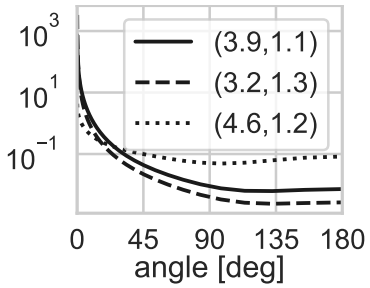

Figure 4.4: Plot of the Fournier-Forand phase function for parameter pairs (μ, n).

A phase function developed for the exact scenario of scattering in ocean water is the *Fournier-Forand* phase function [52]:

$$\begin{aligned}\tilde{\beta}_{\text{FF}}(\theta) = {} & \frac{1 - \delta_{180}^{\nu}}{16\pi(\delta_{180} - 1)\delta_{180}^{\nu}}(3\cos^2\theta - 1) \\ & + \frac{\left[\nu(1-\delta) - (1-\delta^{\nu}) + [\delta(1-\delta^{\nu}) - \nu(1-\delta)]\sin^{-2}\left(\frac{\theta}{2}\right)\right]}{4\pi(1-\delta)^2\delta^{\nu}}\end{aligned} \tag{4.18}$$

where

$$\nu = \frac{3 - \mu}{2} \quad \text{and} \quad \delta = \frac{4}{3(n-1)^2}\sin^2\left(\frac{\theta}{2}\right) \tag{4.19}$$

and δ_{180} is δ evaluated for $\theta = 180°$. It is based on an approximation to Mie theory[5] by first replacing suspended particles with spheres of the same volume and common refractive index n, and then assuming the cumulative distribution of spheres with a certain radius follows an exponential distribution with a rate μ, i.e. $\#\{r_i \geq R\} \propto R^{-\mu}$ where r_i is the i-th sphere's radius [26].

[52]: Fournier et al. (1999), 'Computer-based underwater imaging analysis'

5: Mie theory describes scattering at spherical particles with diameter comparable to the wavelength, but can also be used to derive Rayleigh scattering for smaller particles. It is rather complicated and thus outside the scope of this thesis.

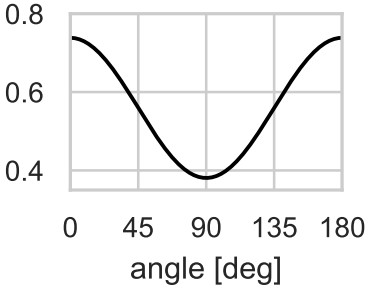

Figure 4.5: Plot of the phase function as predicted by the Einstein-Smoluchowski theory [26].

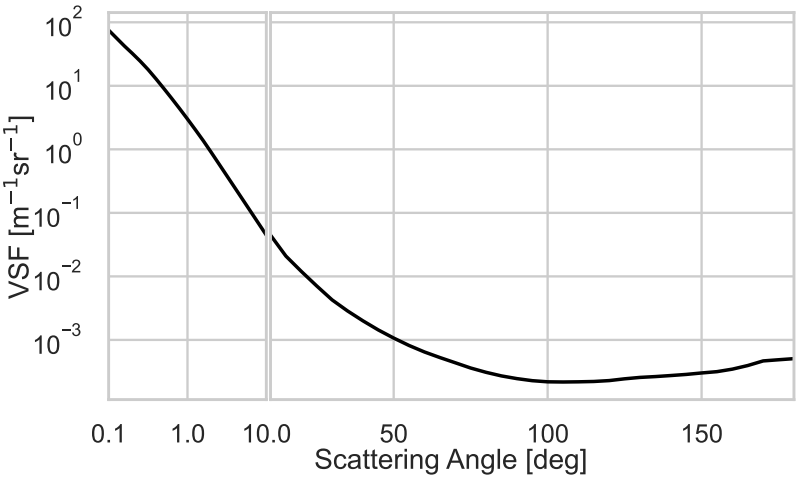

Figure 4.6: Measurement of the VSF in the Tongue of the Ocean at a depth of roughly 1,900 m for a wavelength of $\lambda = 530.0\,\text{nm}$ [43].

[43]: Petzold (1972), *Volume Scattering Functions for Selected Ocean Waters*

Even pure (ocean) water shows scattering caused by thermodynamic fluctuations, as described by the Einstein-Smoluchowski theory. The exact formula is not shown here since we will not be using it and thus, we do not want to include a large list of thermodynamic variables needed to calculate it. Instead, Figure 4.5 shows a plot of the predicted phase function [26, 53, 54].

[26]: Curtis D. Mobley (2022), *The Oceanic Optics Book*

[53]: Smoluchowski (1908), 'Molekular-kinetische Theorie der Opaleszenz von Gasen im kritischen Zustande, sowie einiger verwandter Erscheinungen'

[54]: Einstein (1910), 'Theorie der Opaleszenz von homogenen Flüssigkeiten und Flüssigkeitsgemischen in der Nähe des kritischen Zustandes'

All the previous models assume an ideal scenario they can predict, matching the actual one to a varying degree. Ideally, one obtains measurements of the scattering coefficient and phase function in situ. Unfortunately, hardly any measurements in the deep ocean exist. One notable example is the measurement by Petzold, as shown in Figure 4.6. By integrating the VSF over the unit sphere one obtains the scattering coefficient. However, since Petzold measured at $\lambda = 530.0\,\text{nm}$, one obtains it only for that specific wavelength.

Kopelevich and Mezhericher developed a model for a VSF parameterized by the concentration of small mineral particles ν_s [ppm] ($< 1\,\mu\text{m}$) and large biological particles ν_l [ppm] ($> 1\,\mu\text{m}$), assuming the former have a refractive index relative to water of 1.15 the later 1.03 [55, 56]. We are not interested in this VSF per se, but want to use it to fit the total spectrum of μ_s to the measured VSF. As shown by Mobley, one can first fit both concentrations

[55]: Kopelevich (1983), 'Small-parameter model of optical properties of sea water'

[56]: Kopelevich et al. (1983), 'Calculations of spectral characteristics of light scattering by sea water'

$$\nu_s = -1.4 \cdot 10^{-4}\beta(1^\circ, 550.0\,\text{nm}) + 10.2\beta(45^\circ, 550.0\,\text{nm}) - 0.002 \quad (4.20)$$

$$\nu_l = 2.2 \cdot 10^{-2}\beta(1^\circ, 550.0\,\text{nm}) - 1.2\beta(45^\circ, 550.0\,\text{nm}) \quad (4.21)$$

to then obtain a model for the scattering coefficient

$$\mu_s(\lambda) = 0.0017\left(\frac{550}{\lambda}\right)^{4.3} + 1.34\nu_s\left(\frac{550}{\lambda}\right)^{1.7} + 0.312\nu_l\left(\frac{550}{\lambda}\right)^{0.3} \quad (4.22)$$

where λ has units [nm] and μ_s [m^{-1}] [50].

[50]: Mobley (1994), *Light and Water*

Applied to the measurements by Petzold[6], we obtain values for the concentration of small particles of $\nu_s = 0.012\,22\,\text{ppm}$ and for large particles of $\nu_l = 0.064\,20\,\text{ppm}$ respectively.[7] Figure 4.7 shows the modeled values for the scattering coefficient and compares it to measurements of pure (i.e. little to no particles) seawater [27] and expected Raman scattering (see next section). The large difference between Petzold's

6: We assume the VSF to be similar at 530 nm and 550 nm as μ_s is rather flat there.

7: These values should probably not be used outside the context of the model.

[27]: Smith et al. (1981), 'Optical Properties of the clearest natural waters (200-800 nm)'

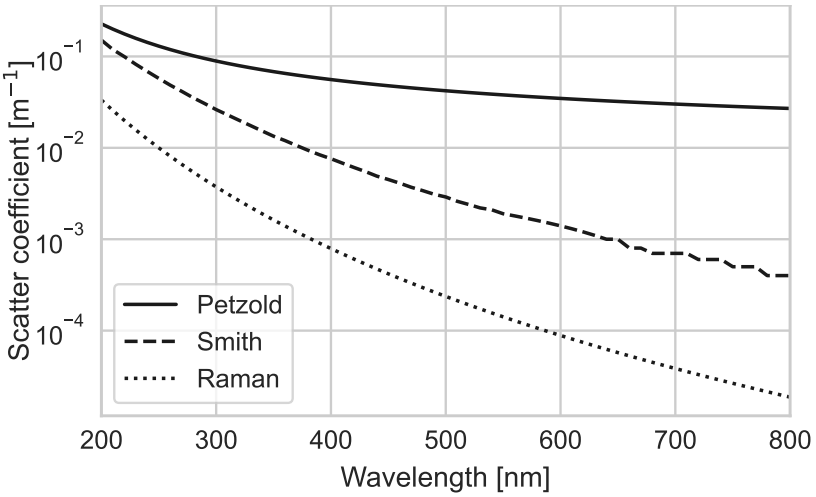

Figure 4.7: Scattering coefficients modeled Petzold's measurements, Smith's measurement of pure seawater and modeled Raman scattering.

measurement of deep ocean water and Smith's for pure seawater indicates a high variability in the scattering coefficient for natural waters attributed to its constituents making actual in situ measurements favorable.

4.4 Inelastic Scattering

Inelastic scattering is similar to its elastic counterpart, with the key difference that the available energy is no longer conserved, namely photons are shifted to longer wavelengths, thus their energy is reduced. The model describing this process also has a distinct scattering coefficient and phase function, but includes a *wavelength distribution function* $f(\lambda, \lambda')$ governing the change from the excitation wavelength λ' to the emission wavelength λ.

In oceans there are usually three sources of fluorescence stated: chlorophyll, dissolved organic matter and water itself in an effect called *Raman scattering*. At the depths we want to operate, we do not expect any chlorophyll, and as literature suggests, Raman is the dominant inelastic scattering here, allowing us to focus solely on it. While all components of seawater may show Raman scattering, it is dominated by water and thus may be modeled by only taking that contribution into account [26, 57].

[26]: Curtis D. Mobley (2022), *The Oceanic Optics Book*
[57]: Pasteris et al. (2004), 'Raman Spectroscopy in the Deep Ocean: Successes and Challenges'

Bartlett et al. measured the scattering coefficient of Raman scattering for seawater and was able to fit a power law $\mu_{\text{Raman}}(\lambda') = 2.7(2) \times 10^{-4}\,\text{m}^{-1} \cdot (488\,\text{nm}/\lambda')^{5.5\pm0.4}$, which is drawn in Figure 4.7 [58].

[58]: Bartlett et al. (1998), 'Raman Scattering by Pure Water and Seawater'

For Raman scattering, $f(\lambda, \lambda')$ can be conveniently described by a distribution of a shift in wavenumber $f(k)$ independent of the excitation wavelength.

$$f_R(\lambda, \lambda') = f_R\left(\frac{1}{\lambda'} - \frac{1}{\lambda}\right) \cdot \Theta(\lambda - \lambda') \tag{4.23}$$

where Θ is the Heaviside function, ensuring that the emission wavelength is longer than the excitation wavelength [26]. Walrafen modeled it as the sum of four Gaussians around $3400\,\text{cm}^{-1}$, as shown in [59]. Also included is the distribution of wavelengths shifts for different excitation wavelengths.

[59]: Walrafen (1967), 'Raman Spectral Studies of the Effects of Temperature on Water Structure'

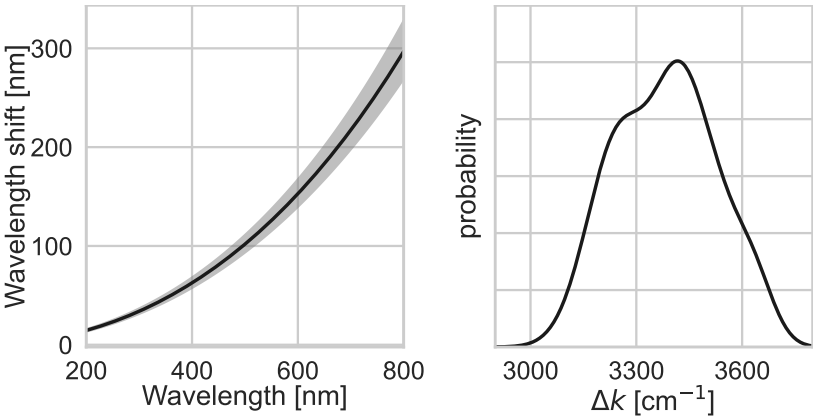

Figure 4.8: Plots describing Raman scattering. Wavelength shift including the 90% quantile on the left, distribution of wavenumber shift on the right.

With the information gathered so far, we can already make a statement about the importance of Raman scattering for the simulation. There is only a large effect for red light where its scattering coefficient is two to three orders of magnitude smaller than the total. To make matters worse, Cherenkov radiation peaks on the spectrum's blue side, making red light less important (see Subsection 2.2.2 on page 6). While in theory Raman scattering makes UV radiation available to the detectors by shifting its wavelength to ranges that can pass the glass sphere, it would most likely require too many scatterings to do so and thus hardly any light would actually reach it this way. Therefore, we will not include Raman scattering in the simulation.

4.5 Equation of Transfer

Putting all previously introduced building blocks regarding light interactions with matter together leads to the *Equation of Transfer*[8] describing the propagation of radiance through a scene as it interacts with it. A complete mathematical investigation, as done by Chandrasekhar [60], is lengthy and not the goal here. Instead, we want to present its final form and only motivate it phenomenological following the derivation shown by Pharr et al. [46].

8: Also known as rendering equation.

[60]: Chandrasekhar (1960), *Radiative Transfer*

[46]: Pharr et al. (2023), *Physically based rendering*

Radiance is described as a vector field, a function assigning each position $\boldsymbol{p}$ and direction $\boldsymbol{\omega}$ a radiance $L(\boldsymbol{p}, \boldsymbol{\omega})$. Consider a light ray entering a differential volume at position $\boldsymbol{p}$ traveling in unit direction $\boldsymbol{\omega}$ carrying in initial radiance L_i and leaving it again at a different position $\boldsymbol{p} + \boldsymbol{\omega} \cdot s$ carrying a radiance L_o. We now want to describe the change in radiance as light interacts with the media:[9]

9: The dependence on λ is implicit to not clutter notation.

$$\mathrm{d}L(\boldsymbol{p}, \boldsymbol{\omega}) = L_o(\boldsymbol{p}, \boldsymbol{\omega}) - L_i(\boldsymbol{p} + \boldsymbol{\omega} \cdot s, \boldsymbol{\omega}) \tag{4.24}$$

While propagating along its direction, light rays get attenuated by a media through absorption and scattering as described by μ_a and μ_s, respectively. These coefficients are usually added up to form the *attenuation coefficient* or *extinction coefficient* $\mu_t = \mu_a + \mu_s$[10], resulting again int the well known Beer-Lambert law

10: Some authors also use $c = a + b$.

$$\mathrm{d}L(\boldsymbol{p}, \boldsymbol{\omega}) = -\mu_t L(\boldsymbol{p} + \boldsymbol{\omega} \cdot s, \boldsymbol{\omega})\mathrm{d}s \tag{4.25}$$

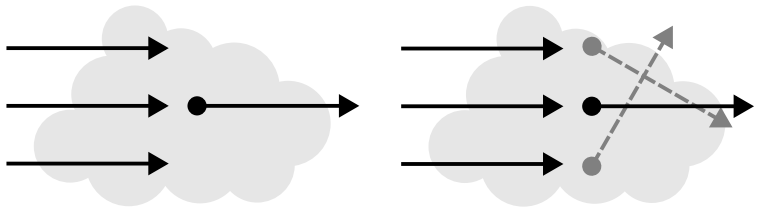

(a) Absorption **(b)** Out Scattering

Figure 4.9: Interactions in media reducing the radiance of a light ray.

Scattering, despite attenuating, can also intensify the radiance of light rays. At a fixed position, light rays traveling in different directions mix according to the media's phase function in a process called *in-scattering* forming a source term:

$$L_s(\boldsymbol{p}, \boldsymbol{\omega}) = \mu_s \int_\Omega \tilde{\beta}(\boldsymbol{\omega} \circ \boldsymbol{\omega}') L(\boldsymbol{p}, \boldsymbol{\omega}') \mathrm{d}\boldsymbol{\omega}' \tag{4.26}$$

To model emitting media, one can add an emission term $L_e(\boldsymbol{p}, \boldsymbol{\omega})$ describing the added radiance at $\boldsymbol{p}$ in direction $\boldsymbol{\omega}$ to the source term.

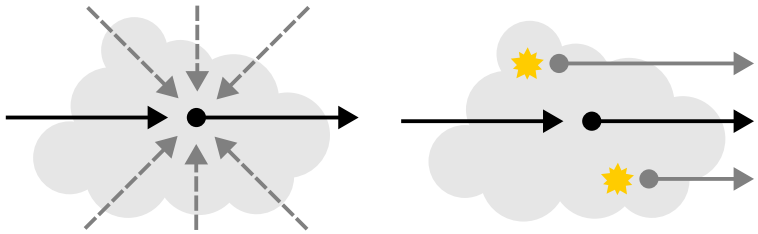

(a) In Scattering **(b)** Emission

Figure 4.10: Interactions in media enhancing the radiance of a light ray.

By combining the attenuation and source term, one finally obtains the integro-differential form of the equation of transfer:

$$\frac{\partial}{\partial s} L(\boldsymbol{p}, \boldsymbol{\omega}) = -\mu_t L(\boldsymbol{p}, \boldsymbol{\omega}) + L_s(\boldsymbol{p}, \boldsymbol{\omega}) \tag{4.27}$$

The equation of transfer does not account for interfaces between media, which must be introduced as boundary conditions. For example, assume that along a line $\boldsymbol{p} + \boldsymbol{\omega} \cdot s$ exists an interface at $s = s_0$. The radiance at a different point along the line at $s = s_1$ can then be calculated as

$$L(\boldsymbol{p}(s_1), \boldsymbol{\omega}) = \int_{s_0}^{s_1} \frac{\partial}{\partial s} L(\boldsymbol{p}, \boldsymbol{\omega}) \mathrm{d}s \tag{4.28}$$

Contribution from reflection and transmission at the interface can be introduced by modifying the source term at $p(s_0)$ to use the BSDF instead of the phase function:[11]

$$L_s(\boldsymbol{p}(s_0), \boldsymbol{\omega}) = \int_\Omega L(\boldsymbol{p}, \boldsymbol{\omega}') f(\boldsymbol{\omega}, \boldsymbol{\omega}') |\cos\theta| d\boldsymbol{\omega}' \tag{4.29}$$

where $\cos\theta$ is the cosine between the light ray's direction and the surface normal handling Lambert's cosine law.

11: In our case, since the BSDF is specular, this reduces to the addition of transmitted and reflected radiance.

In real-world scenarios, we will not measure the radiance directly but the response of a sensor detecting it, e.g. an electric current or a deposited charge. Mathematically, this is described by the *measurement equation*

$$I = \int W_e(\boldsymbol{p}, \omega) L(\boldsymbol{p}, \omega) \mathrm{d}A(\boldsymbol{p}) \mathrm{d}\omega \tag{4.30}$$

relating a measurement I to the incident radiance by first multiplying it with the sensor-specific *responsivity*[12] $W_e(\boldsymbol{p}, \omega)$ carrying the appropriate unit to convert radiance to the unit of measurement and then integrating it over the sensor surface and solid angle.

12: The naming reminds of the previously mentioned emission term on purpose. As we will see in a bit, in the adjoint method the sensor emits importance.

Veach formulated in his PhD thesis [61] the equation of transfer in terms of operators acting on the radiance and finally used the measurement equation to define adjoint operators acting on the responsivity instead, i.e. instead of transporting radiance emitted from a light source through a scene towards a sensor, the adjoint method transports *importance* emitted from a sensor to the light sources. One can thus reformulate the equation of transfer to use importance $W(\boldsymbol{p}, \omega)$ instead:

[61]: Veach (1997), 'Robust Monte Carlo Methods for Light Transport Simulation'

$$\frac{\partial}{\partial s} W(\boldsymbol{p}, \omega) = -\mu_t W(\boldsymbol{p}, \omega) + W_s(\boldsymbol{p}, \omega) \tag{4.31}$$

$$W_s(\boldsymbol{p}, \omega) = W_e(\boldsymbol{p}, \omega) + \int_\Omega \tilde{\beta}(\boldsymbol{\omega} \circ \boldsymbol{\omega}') W(\boldsymbol{p}, \boldsymbol{\omega}') \mathrm{d}\boldsymbol{\omega}' \tag{4.32}$$

While the transport of importance seems to behave just like for radiance, this is not generally true. Reformulating Equation 4.29 to use importance instead requires a subtle change, where we change the order of ω and ω':

$$W_s(\boldsymbol{p}, \omega) = \int_\Omega W(\boldsymbol{p}, \boldsymbol{\omega}') f(\boldsymbol{\omega}', \boldsymbol{\omega}) |\cos\theta| d\boldsymbol{\omega}' \tag{4.33}$$

The BSDF is generally not required to be symmetric under the exchange of its arguments.[13] In fact, this is already the case for the specular interfaces we wish to model.

13: In theory there can also be asymmetric VSF, but these are not considered here.

Veach showed that for any physically valid BSDF f, the following relation holds:

$$\frac{f(\omega', \omega)}{n'^2} = \frac{f(\omega, \omega')}{n^2} \tag{4.34}$$

where n and n' are the refractive indices of the incident and outgoing ray respectively. Applying this to Equation 4.9, we see that the extra factor n_t^2/n_i^2 for refracting radiance cancels out when transporting importance instead.[14]

14: Since this factor applies to both entering and leaving a medium, erroneously applying or omitting this factor cancels out if both source and sensor are in the same medium.

The challenge in using the equation of transfer not only stems from the boundary conditions, but also from referencing itself, making it impossible to solve in closed form analytically besides in the simplest scenarios. Transforming it into a more manageable form is the goal of Section 6.1 on page 33. There, we will also consider that light has a finite propagation speed.

5 Polarization

After determining in Section 3.4 that we should incorporate polarization into the simulation, making it a rather novel approach, this chapter introduces the necessary mathematical tools. We start with the Stokes vector representation of polarization and Mueller matrices modelling interactions altering it. The chapter finishes by extending the Equation of Transfer to include polarization effects.

5.1 Stokes-Mueller Formalism 27
5.2 Media Interaction 28
5.3 Vector Radiative Transfer Equation 31

We will only provide a minimal introduction to the concepts of the Stokes-Mueller formalism. A more detailed one can be found in various textbooks (e.g. [62, 63]).

[62]: Novikova et al. (2023), 'Polarized Light'
[63]: Kattawar et al. (2016), 'Polarization of light in the atmosphere and ocean'

5.1 Stokes-Mueller Formalism

Starting from the wave equation Equation 3.5 derived from Maxwell's equation, a particular solution results in monochromatic planar waves. Let z denote the direction the wave propagates, then we can write the wave as:

$$\boldsymbol{E} = E_x e^{i(\omega t - kz + \delta_x)} \hat{\boldsymbol{e}}_x + E_y e^{i(\omega t - kz + \delta_y)} \hat{\boldsymbol{e}}_y \tag{5.1}$$

Using $\delta = \delta_x - \delta_y$ the Stokes vector $\boldsymbol{S}$ is than:[1]

$$\boldsymbol{S} = \begin{pmatrix} I \\ Q \\ U \\ V \end{pmatrix} = \begin{pmatrix} E_x^2 + E_x^2 \\ E_x^2 - E_y^2 \\ 2E_x E_y \cos\delta \\ 2E_x E_x \sin\delta \end{pmatrix} \tag{5.2}$$

1: Some authors define V using the opposite sign.

Each component of the Stokes vector can be summarized as follows: I is the total radiance, Q describes the linear polarization with respect to the axes, U the linear polarization with respect to the diagonal and V describes the circular polarization. Between the components, the following relation holds:

$$I^2 = Q^2 + U^2 + V^2 \tag{5.3}$$

which can be used to define the *degree of polarization* ρ:

$$\rho = \frac{\sqrt{Q^2 + U^2 + V^2}}{I} \qquad (0 \leq \rho \leq 1) \tag{5.4}$$

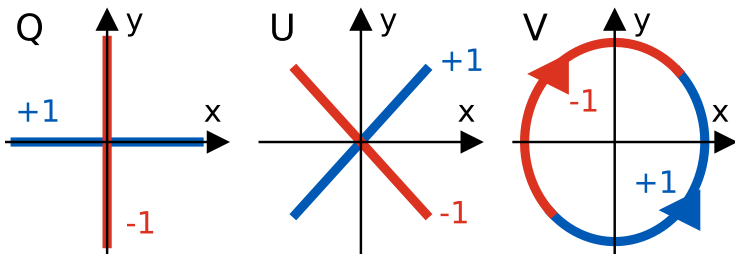

Figure 5.1: Illustration of the polarization components of a Stokes vector with $I = 1$ where each is drawn as a polarization ellipse.

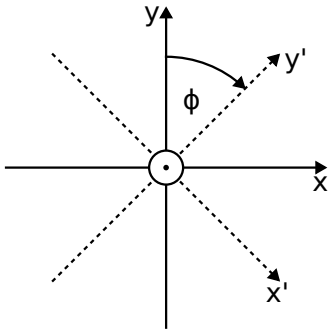

Figure 5.2: Illustration of rotating a Stokes vector. Light propagates out of plane and the angle ϕ is defined to be clockwise.

Analogously, one can define degree of linear (ρ_l) and circular (ρ_c) polarization.

Based on its definition, one can see that the specific representation of the Stokes vector depends on the particular choice of a coordinate system with the only requirement that $\hat{\boldsymbol{e}}_x$ and $\hat{\boldsymbol{e}}_y$ are perpendicular to $\hat{\boldsymbol{e}}_z$ and each other. Either axis can thus parameterize the set of possible reference frames. Now assume $\hat{\boldsymbol{e}}_y$ and $\hat{\boldsymbol{e}}'_y$ identify two different reference frames for the same light ray. Let ϕ be the clockwise rotation around $\hat{\boldsymbol{e}}_z$ that transforms the former into the latter, then the Stokes vector transforms according to:

$$\boldsymbol{S}' = \begin{pmatrix} I' \\ Q' \\ U' \\ V' \end{pmatrix} = \begin{bmatrix} 1 & 0 & 0 & 0 \\ 0 & \cos 2\phi & -\sin 2\phi & 0 \\ 0 & \sin 2\phi & \cos 2\phi & 0 \\ 0 & 0 & 0 & 1 \end{bmatrix} \begin{pmatrix} I \\ Q \\ U \\ V \end{pmatrix} = \mathbb{R}(\phi)\boldsymbol{S} \tag{5.5}$$

As light interacts with media its Stokes vector may change. Similar to $\mathbb{R}(\phi)$ this change is described by a 4x4 matrix $\mathbb{M}$ called *Mueller matrix*[2]

$$\boldsymbol{S}' = \begin{pmatrix} I' \\ Q' \\ U' \\ V' \end{pmatrix} = \begin{bmatrix} M_{11} & M_{12} & M_{13} & M_{14} \\ M_{21} & M_{22} & M_{23} & M_{24} \\ M_{31} & M_{32} & M_{33} & M_{34} \\ M_{41} & M_{42} & M_{43} & M_{44} \end{bmatrix} \begin{pmatrix} I \\ Q \\ U \\ V \end{pmatrix} = \mathbb{M}\boldsymbol{S} \tag{5.6}$$

which is often normalized to M_{11}:

$$\mathbb{M} = M_{11} \begin{bmatrix} 1 & m_{12} & m_{13} & m_{14} \\ m_{21} & m_{22} & m_{23} & m_{24} \\ m_{31} & m_{32} & m_{33} & m_{34} \\ m_{41} & m_{42} & m_{43} & m_{44} \end{bmatrix} \tag{5.7}$$

Usually, Mueller matrices are defined to a specific reference frame, e.g. the scattering plane or plane of incidence. To transform between them, one can again use $\mathbb{R}(\phi)$:

$$\mathbb{M}' = \mathbb{R}(\phi)\mathbb{M}[\mathbb{R}(\phi)]^{-1} \tag{5.8}$$

5.2 Media Interaction

As discussed in Chapter 4, we are interested in three distinct media interactions: Absorption, volume scattering as well as the transmission and reflection at interfaces.

For unpolarized light, absorption is the only way media can affect light rays as they travel through it without changing their direction, whereas for polarized light it can also solely alter the polarization while keeping the energy constant. Unfortunately, the naive extension to the Beer-Lambert law Equation 4.13 of replacing the scalar extinction coefficient μ_t with a corresponding Mueller matrix is not generally applicable. Take, for instance, a waveplate introducing a phase shift of 180° (i.e. a half-wave plate): The corresponding Mueller matrix describing the change in polarization of light as it travels through it is $\mathrm{diag}(1, 1, -1, -1)$, which obviously cannot be produced by a matrix exponential. However, for

2: Some authors also consider $\mathbb{R}(\phi)$ to be a Mueller matrix. Strictly speaking, it does not change the Stokes vector itself, but only its representation.

the type of media we are interested in, such as ocean water, the naive approach does work and we can replace the extinction coefficient μ_t by corresponding extinction matrix $\mathbb{K}$ [26, 64]:

[26]: Curtis D. Mobley (2022), *The Oceanic Optics Book*
[64]: Franssens (2014), 'Modelling polarization dependent absorption: The vectorial Lambert-Beer law'

$$\mathbb{K} = \mu_t \begin{bmatrix} 1 & 0 & 0 & 0 \\ 0 & 1 & 0 & 0 \\ 0 & 0 & 1 & 0 \\ 0 & 0 & 0 & 1 \end{bmatrix} \tag{5.9}$$

Unlike absorption, the generalization of scattering to polarized light is fortunately much easier and essentially consists of replacing the VSF with the corresponding *phase matrix*[3] $\mathbb{P}$, where we recognize P_{11} as the VSF $\beta(\theta, \lambda)$. Assuming the suspended particles in the medium causing scattering are mirror-symmetric and randomly oriented, the normalized phase matrix takes the form

3: In literature often also just called Mueller matrix.

$$\mathbb{P} = \beta(\theta, \lambda) \begin{bmatrix} 1 & p_{12}(\theta) & 0 & 0 \\ p_{12}(\theta) & p_{22}(\theta) & 0 & 0 \\ 0 & 0 & p_{33}(\theta) & p_{34}(\theta) \\ 0 & 0 & -p_{34}(\theta) & p_{44}(\theta) \end{bmatrix} \tag{5.10}$$

with the reference frame denoted by $\hat{\boldsymbol{e}}_y$ being perpendicular to the plane of scattering.

We notice that the wavelength dependency of the phase matrix is entirely described by the VSF, which can be further split off into the scattering coefficient $\mu_s(\lambda)$, as shown in Section 4.3 [26].

Similar to VSF, there are hardly any measurements of the phase matrix, with Voss and Fry [65] being a notable example. Their measurements indicated that $p_{34} \approx 0$ and $p_{33} \approx p_{44}$, further reducing the degrees of freedom. Kokhanovsky [66] derived a physically motivated fit on these measurements, extending them to the full range of 180°. Both the measurements and the fit are plotted in Figure 5.3.

[65]: Voss et al. (1984), 'Measurement of the Mueller matrix for ocean water'
[66]: Kokhanovsky (2003), 'Parameterization of the Mueller matrix of oceanic waters'

Using the Fresnel formulae Equation 4.5 and Equation 4.6 in combination with the definition of the Stokes vector, one can derive the Mueller matrices for reflection

$$\mathbb{M}_R = \frac{1}{2} \begin{bmatrix} r_\parallel^2 + r_\perp^2 & r_\parallel^2 - r_\perp^2 & 0 & 0 \\ r_\parallel^2 - r_\perp^2 & r_\parallel^2 + r_\perp^2 & 0 & 0 \\ 0 & 0 & 2r_\parallel r_\perp & 0 \\ 0 & 0 & 0 & 2r_\parallel r_\perp \end{bmatrix} \tag{5.11}$$

and transmission

$$\mathbb{M}_T = \frac{1}{2} \frac{n_t^3 \cos\theta_t}{n_i^3 \cos\theta_i} \begin{bmatrix} t_\parallel^2 + t_\perp^2 & t_\parallel^2 - t_\perp^2 & 0 & 0 \\ t_\parallel^2 - t_\perp^2 & t_\parallel^2 + t_\perp^2 & 0 & 0 \\ 0 & 0 & 2t_\parallel t_\perp & 0 \\ 0 & 0 & 0 & 2t_\parallel t_\perp \end{bmatrix} \tag{5.12}$$

where both are defined in the reference frame defined by $\hat{\boldsymbol{e}}_y$ being perpendicular to the plane of incidence [67].

[67]: Garcia (2012), 'Fresnel boundary and interface conditions for polarized radiative transfer in a multilayer medium'

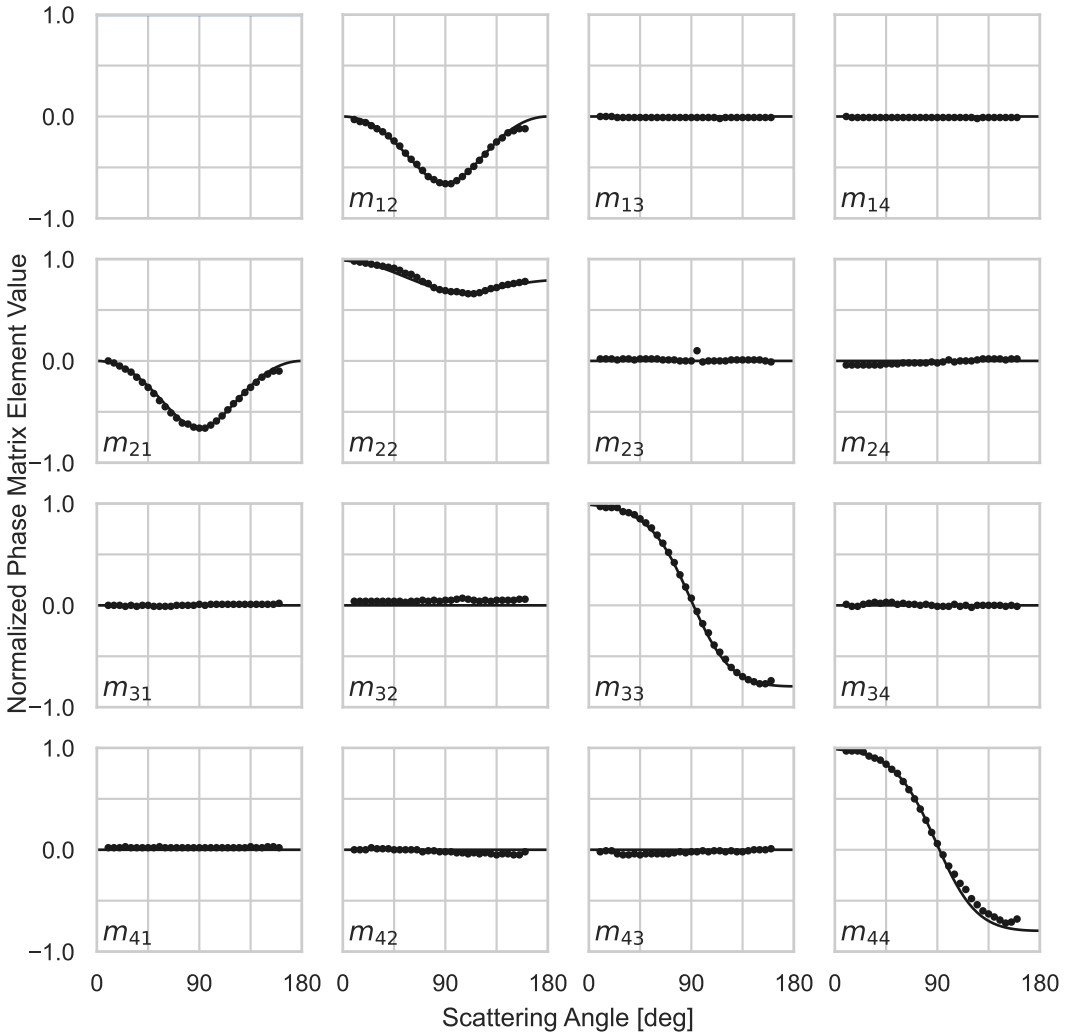

Figure 5.3: Normalized phase matrix of scattering in ocean water measured by Voss et al. [65] superimposed with the fitted model by Kokhanovsky [66] used to extend the measurements to the full range of 180°. ($p(90°) = 0.66$, $\theta_0 = 0.25\,\mathrm{rad}$, $\alpha = 4\,\mathrm{rad}^{-1}$, $\xi = 25.6$)

5.3 Vector Radiative Transfer Equation

Transforming the equation of transfer into its polarized version requires minimal alterations with almost all necessary parts already established in this chapter. The only missing one is the polarized emission term $\mathbf{\Sigma}$ after which we can finally write the *Vector Radiative Transfer Equation* (VRTE):

$$\frac{\partial}{\partial s}\boldsymbol{S}(\boldsymbol{p},\boldsymbol{\omega}) = -\mu_t \boldsymbol{S}(\boldsymbol{p},\boldsymbol{\omega}) + \boldsymbol{S}_s(\boldsymbol{p},\boldsymbol{\omega}) \tag{5.13}$$

$$\boldsymbol{S}_s(\boldsymbol{p},\boldsymbol{\omega}) = \int_\Omega \mathbb{R}(\alpha)\mathbb{P}(\boldsymbol{\omega}\circ\boldsymbol{\omega'})\mathbb{R}(\alpha')\boldsymbol{S}(\boldsymbol{p},\boldsymbol{\omega'})\mathrm{d}\omega' + \mathbf{\Sigma}(\boldsymbol{p},\boldsymbol{\omega}) \tag{5.14}$$

In the VRTE, we made the need to perform the scattering in the reference frame of the plane of scattering explicit by introducing two rotation matrices $\mathbb{R}(\alpha)$ and $\mathbb{R}(\alpha')$ responsible for first transforming the reference frame of the inscattering light to the scattering plane and then transforming it to a common one before integrating the contributions [26, 68].

[26]: Curtis D. Mobley (2022), *The Oceanic Optics Book*
[68]: Novikova et al. (2023), 'Polarized-Sensitive Monte Carlo'

The measurement equation can be extended similarly: We first redefine the sensor sensitivity to return a covector mapping the Stokes vector into a scalar measurement.[4] Note that the sensitivity is also defined with respect to a specific reference frame which may require an additional rotation to match it with the Stokes vector. Summarizing this into a formula, we write the measurement equation as

4: Or use a tensor instead for a higher dimensional measurment.

$$I = \int W_e^T(\boldsymbol{p},\boldsymbol{\omega})\mathbb{R}\boldsymbol{S}(\boldsymbol{p},\boldsymbol{\omega})\mathrm{d}A\mathrm{d}\omega \tag{5.15}$$

where we again inserted explicitly a rotation matrix and noted the covector as column vector via the transpose to make the requirements explicit. A mathematically more rigorous derivation was done by e.g. Mojzik et al. [69].

[69]: Mojzík et al. (2016), 'Bi-Directional Polarised Light Transport'

When transporting importance[5] instead of radiance, one has to keep in mind that matrix multiplications are not commutative and thus has to apply the Mueller matrices from the right to the covector.

5: See Section 4.5 on page 23

Finally, the remarks from Section 4.5 on page 23 regarding the equation of transfer still applies, as the VTE is equally challenging to solve analytic. Luckily, due to their similarities, the alternate form introduced in Section 6.1 on page 33 can also be applied to the VTE using the same transformations used for its derivation.

6 Simulation Algorithm

This chapter first introduces the mathematical tools required for the simulation algorithms, namely path integrals, making the equation of transfer manageable and Monte Carlo as a method to evaluate them. It finishes by describing the implementation of the algorithms that are actual used.

6.1 Path Integrals 33
6.2 Monte Carlo Method 35
6.3 Unidirectional Path Tracing 37
6.4 Bidirectional Path Tracing 42

6.1 Path Integrals

Due to the recursive definition of the Equation of Transfer, it is hard to use in algorithms and must first be transformed into a more manageable form. A rigorous mathematical derivation of it as it was done by Jakob [70] is lengthy and offers little benefits compared to a more pragmatic approach. Instead, we will abuse the notation a bit to hopefully make the underlying concept more clear. Following the derivation shown by Pharr et al. [46] we first introduce a new notation: Given two points $\boldsymbol{p}$ and $\boldsymbol{p}'$ we write the exitant radiance from the first to the latter as

[70]: Jakob (2013), 'Light Transport on Path-Space Manifolds'

[46]: Pharr et al. (2023), *Physically based rendering*

$$L(\boldsymbol{p}' \to \boldsymbol{p}) = L(\boldsymbol{p}', \boldsymbol{\omega}) \tag{6.1}$$

with $\boldsymbol{\omega} = \widehat{\boldsymbol{p} - \boldsymbol{p}'} = \boldsymbol{p} - \boldsymbol{p}'/(||\boldsymbol{p} - \boldsymbol{p}'||)$ being the unit direction from $\boldsymbol{p}'$ to $\boldsymbol{p}$. Similarly, for the phase function describing the scattering at a location $\boldsymbol{p}_n$ of a light ray originating at $\boldsymbol{p}_{n-1}$ into the direction of $\boldsymbol{p}_{n+1}$, we write:

$$\tilde{\beta}(\boldsymbol{p}_{n-1} \to \boldsymbol{p}_n \to \boldsymbol{p}_{n+1}) = \tilde{\beta}(\widehat{\boldsymbol{p}_n - \boldsymbol{p}_{n-1}} \circ \widehat{\boldsymbol{p}_{n+1} - \boldsymbol{p}_n}) \tag{6.2}$$

The formerly implicit condition of two points needing to be mutually visible in order to be able to apply the equation of transfer is next made explicit by introducing the visibility function $V(\boldsymbol{p}' \leftrightarrow \boldsymbol{p})$ returning 1, if the positions are mutually visible, i.e. not obstructed by any interfaces, and 0 otherwise. Further, we define $T_r(\boldsymbol{p}' \to \boldsymbol{p}) = \exp\left(-\mu_t \cdot ||\boldsymbol{p} - \boldsymbol{p}'||\right)$ as a shorthand notation for beam transmittance.

A crucial part of forming the path integrals is transforming the source term from an integral over solid angles to an integral over points in the volume $\mathrm{d}\boldsymbol{\omega} = \mathrm{d}V/||\boldsymbol{p} - \boldsymbol{p}'||^2$. We combine this with the visibility term and beam transmittance to create the geometric term G

$$G(\boldsymbol{p}' \leftrightarrow \boldsymbol{p}) = V(\boldsymbol{p}' \leftrightarrow \boldsymbol{p}) T_r(\boldsymbol{p} \to \boldsymbol{p}') \frac{1}{||\boldsymbol{p} - \boldsymbol{p}'||^2} \tag{6.3}$$

which finally allows us to rewrite the equation of transfer as

$$\begin{aligned} L(\boldsymbol{p}' \to \boldsymbol{p}) &= L_e(\boldsymbol{p}' \to \boldsymbol{p}) T_r(\boldsymbol{p}' \to \boldsymbol{p}) \\ &\quad + \int_V \mu_s \tilde{\beta}(\boldsymbol{p}'' \to \boldsymbol{p}' \to \boldsymbol{p}) L(\boldsymbol{p}'' \to \boldsymbol{p}') G(\boldsymbol{p}'' \leftrightarrow \boldsymbol{p}') \mathrm{d}V(\boldsymbol{p}'') \end{aligned} \tag{6.4}$$

where $L_e(\boldsymbol{p}' \to \boldsymbol{p})$ accounts for any emitted radiance from $\boldsymbol{p}'$ to $\boldsymbol{p}$, i.e. light sources.

Right now, the path integral does not handle scattering at interfaces. To include this, we replace the phase function and geometric term by their generalized counterparts $\hat{f}$ and $\hat{G}$, respectively, distinguishing between points in media and on interfaces. Consider a path segment $\boldsymbol{p}'' \to \boldsymbol{p}' \to \boldsymbol{p}$ with $\boldsymbol{p}$ and $\boldsymbol{p}'$ positioned on surfaces, as depicted in Figure 6.1. We first define

$$\hat{f}(\boldsymbol{p}'' \to \boldsymbol{p}' \to \boldsymbol{p}) = \begin{cases} \mu_s \tilde{\beta}(\boldsymbol{p}'' \to \boldsymbol{p}' \to \boldsymbol{p}), & \text{if } \boldsymbol{p}' \in V \\ f(\boldsymbol{p}'' \to \boldsymbol{p}' \to \boldsymbol{p}), & \text{if } \boldsymbol{p}' \in A \end{cases} \tag{6.5}$$

where f is the BSDF as described in Section 4.1 on page 17 reformed similar to Equation 6.2. Starting again at the original integral of the source term over solid angles and note that $d\boldsymbol{\omega} = |\cos\theta_p|/||\boldsymbol{p} - \boldsymbol{p}'||^2 dA$ for $\boldsymbol{p}$ positioned on surfaces with $\cos\theta_p$ being the incident angle the ray $\boldsymbol{p}' \to \boldsymbol{p}$ makes with the surface $\boldsymbol{p}$ lies on. Additionally, if the scatter point $\boldsymbol{p}'$ is on a surface, we gain an extra $|\cos\theta_{p'}|$ from the dA of the incident radiance (Lambert's cosine law).[1] Taking this into account, the generalized geometric term becomes

1: See also the definition of the BSDF in Equation 4.10.

$$\hat{G}(\boldsymbol{p} \leftrightarrow \boldsymbol{p}') = V(\boldsymbol{p} \leftrightarrow \boldsymbol{p}') T_r(\boldsymbol{p} \to \boldsymbol{p}') \frac{C_p(\boldsymbol{p}, \boldsymbol{p}') C_{p'}(\boldsymbol{p}, \boldsymbol{p}')}{||\boldsymbol{p} - \boldsymbol{p}'||^2} \tag{6.6}$$

$$C_p(\boldsymbol{p}, \boldsymbol{p}') = \begin{cases} |\cos\theta_p|, & \text{if } \boldsymbol{p} \in A \\ 1, & \text{otherwise} \end{cases}$$

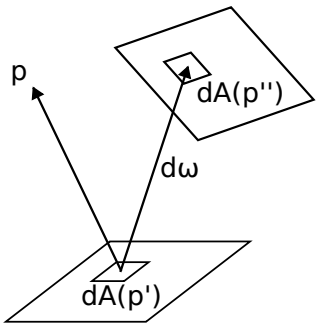

Figure 6.1: Depiction of a path segment including surface elements.

Rewriting Equation 6.4 using the previously introduced generalized terms results in

$$L(\boldsymbol{p}' \to \boldsymbol{p}) = L_e(\boldsymbol{p}' \to \boldsymbol{p}) T_r(\boldsymbol{p}' \to \boldsymbol{p}) + \int \hat{f}(\boldsymbol{p}'' \to \boldsymbol{p}' \to \boldsymbol{p}) L(\boldsymbol{p}'' \to \boldsymbol{p}') \hat{G}(\boldsymbol{p}'' \to \boldsymbol{p}') \mathrm{d}\mu(\boldsymbol{p}'') \tag{6.7}$$

where $\mathrm{d}\mu(\boldsymbol{p})$ is either $\mathrm{d}A$ or $\mathrm{d}V$ depending on the location of $\boldsymbol{p}$.[2]

The final step is to iteratively insert Equation 6.7 into itself, resulting in an infinite sum of integrals with each term responsible for light paths of a certain constant length:

$$L(\boldsymbol{p}_1 \to \boldsymbol{p}_0) = \sum_{n=1}^{\infty} P(\bar{p}_n) \tag{6.8}$$

$$P(\bar{p}_n) = \underbrace{\int \cdots \int}_{n-1} L_e(\boldsymbol{p}_n \to \boldsymbol{p}_{n-1}) T(\bar{p}_n) \, \mathrm{d}\mu(\boldsymbol{p}_2) \ldots \mathrm{d}\mu(\boldsymbol{p}_n) \tag{6.9}$$

$$T(\bar{p}_n) = \prod_{i=1}^{n-1} \hat{f}(\boldsymbol{p}_{i+1} \to \boldsymbol{p}_i \to \boldsymbol{p}_{i-1}) \hat{G}(\boldsymbol{p}_{i+1} \leftrightarrow \boldsymbol{p}_i) \tag{6.10}$$

2: Mathematically more precise is $\mathrm{d}\mu$ defined on the Cartesian product of V and A, thus ensuring the integral always has the same metric regardless of the location of $\boldsymbol{p}''$.

Equation 6.9 can now be integrated using standard numeric integration techniques, preferably Monte Carlo, as described in Section 6.2. Additionally, the sum in Equation 6.8 allows an intuitive partition of the calculation as the integrals are independent. This can for example be exploited when calculating the direct lighting $P(\bar{p}_1)$ contribution by directly sampling the light source and detector instead of simulating paths.[3]

3: Although beneficial, the formula itself does not care if the paths are simulated or randomly assembled.

Since scattering reduces the radiance along a path, later terms contribute less to the result. Thus by truncating the infinite sum to an appropriate length depending on the specific setup simulated, the equation becomes computable while introducing only a negligible error.

Finally, we take the finite speed of light into account. As described in Section 3.2 on page 12, light propagates at the group velocity v_g. Let $v_g(\boldsymbol{p} \to \boldsymbol{p}')$ be the group velocity of the medium the path segment $\boldsymbol{p} \to \boldsymbol{p}'$ lies in, we can calculate the total propagation time t of the light along a path using the following equation:

$$t(\boldsymbol{p}_n \to \boldsymbol{p}_0) = \sum_{i=1}^{n} \frac{||\boldsymbol{p}_n - \boldsymbol{p}_{n-1}||}{v_g(\boldsymbol{p}_n \to \boldsymbol{p}_{n-1})} \tag{6.11}$$

6.2 Monte Carlo Method

Monte Carlo methods refer to a set of numerical tools based on random sampling to solve stochastic problems dating back to the 1940s, where it was developed at Los Alamos to perform neutronic calculations [71, 72]. While it applies to a wide range of tasks, we will only use it to calculate the integrals of the previous section.

[71]: Metropolis et al. (1949), 'The Monte Carlo Method'
[72]: Avneet Sood et al. (2021), 'Neutronics Calculation Advances at Los Alamos: Manhattan Project to Monte Carlo'

This section starts by introducing Monte Carlo integration loosely based on Lemieux [73], followed by more advanced techniques improving its performance.

[73]: Lemieux (2009), *Monte Carlo and Quasi-Monte Carlo Sampling*

6.2.1 Monte Carlo Integration

Given a function $f(x)$ and N samples x_i sampled from a uniform distribution $U(D)$ over the domain D with Lebesgue measure $vol(D)$,

$$Q_N = \frac{vol(D)}{N} \sum_{i=1}^{N} f(x_i) \qquad x_i \sim U(D) \tag{6.12}$$

is an unbiased estimator for the integral of $f(x)$ over D, that is its expected value $\mathbb{E}[Q_N]$ converges to the corresponding integral $I[f]$:

$$\begin{aligned} \mathbb{E}[Q_N] &= \frac{vol(D)}{N} \sum_{i=1}^{N} \mathbb{E}[f(x_i)] \\ &= vol(D) \int_D \frac{f(x)}{vol(D)} \mathrm{d}x = \int_D f(x) \mathrm{d}x = I[f] \end{aligned} \tag{6.13}$$

Usually, one chooses D to be the d-dimensional unit hypercube[4] $[0, 1)^d$ using appropriate transformation and thus $vol(\mathrm{D}) = 1$.

4: We deliberately chose the half-open interval to match the algorithms producing random numbers.

Furthermore, the central limit theorem states that the error in the estimate converges to a normal distribution at a rate $O(N^{-1/2})$:

$$\lim_{N \to \infty} \frac{Q_N - I[f]}{\sigma / \sqrt{N}} = N(0, 1) \tag{6.14}$$

where σ^2 is the variance of f and thus intrinsic to it.

To improve the performance of the estimator, one tries to replace f with a different function of the same integral but smaller variance in a method called *variance reduction technique*. A common example of such a technique is *importance sampling*, where the samples are not drawn uniformly but from a distribution p similar to the integrand:[5]

$$\int f(x)\mathrm{d}x = \int \frac{f(x)}{p(x)} p(x)\mathrm{d}x = \mathbb{E}_{x\sim p}\left[\frac{f(x)}{p(x)}\right] \tag{6.15}$$

5: Indeed, it is so common that some authors already define the Monte Carlo integral including it.

While there exist deterministic alternatives to Monte Carlo integration, these typically scale poorly with the dimensionality of the integral. For example, the trapezoidal shows an error scaling with $O(N^{-2/d})$, thus outperforming Monte Carlo only for small d [73].

[73]: Lemieux (2009), *Monte Carlo and Quasi-Monte Carlo Sampling*

6.2.2 Multiple Importance Sampling

A problem that may arise using importance sampling is that there is not one suitable distribution to sample from but multiple, each handling different parts of the integrand best. Veach developed a way to combine these distributions, which he named *multiple importance sampling* (MIS) [61].

[61]: Veach (1997), 'Robust Monte Carlo Methods for Light Transport Simulation'

We consider again the integration of f over D as defined previously. Let $p_1, \ldots, p_k$ be a set of k different distributions allowing to sample from and evaluating at any $x \in D$, each having a corresponding weighting function $w_i(x)$. Further, n_i is the number of samples X_{ij} drawn from each p_i respectively. Veach showed that

$$F = \sum_{i=1}^{k} \frac{1}{n_i} \sum_{j=1}^{n_i} w_i(X_{ij}) \frac{f(X_{ij})}{p_i(X_{ij})} \tag{6.16}$$

is an unbiased estimator for $I[f]$ given that:

$$f(x) \neq 0 \quad \Rightarrow \quad \sum_{i=1}^{k} w_i(x) = 1 \tag{6.17a}$$

$$p_i(x) = 0 \quad \Rightarrow \quad w_i(x) = 0 \tag{6.17b}$$

For MIS to improve the performance of the Monte Carlo integral, the weighting functions w_i have to be chosen such that the variance of F is decreased compared to f. Veach introduced different weighting functions and gave mathematical proof for their performance. Here we will only show the definitions of the ones we used, namely the *balance heuristic*

$$w_i(x) = \frac{n_i p_i(x)}{\sum_j n_j p_j(x)} \tag{6.18}$$

and the *power heuristic*[6]

$$w_i(x) = \frac{(n_i p_i(x))^\beta}{\sum_j (n_j p_j(x))^\beta} \tag{6.19}$$

6: Veach recommends $\beta = 2$

An interesting benefit from multiple importance sampling is that it allows

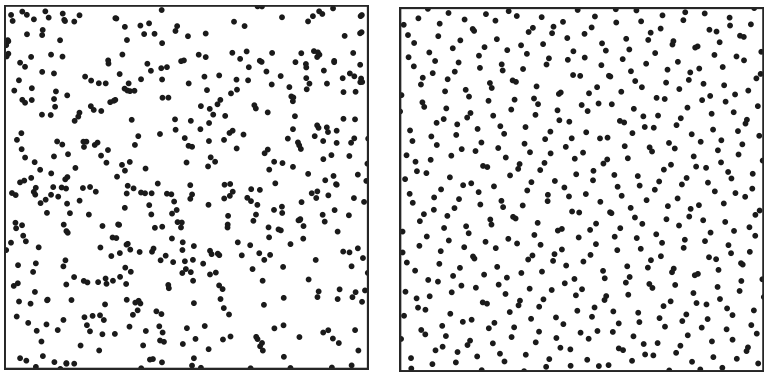

(a) Pseudo-random (Philox) **(b)** Scrambled Sobol

Figure 6.2: Comparison of random numbers sampled from a pseudo-random function (Philox) and from scrambled Sobol sequence. While both are random, one can clearly see that the latter cover the area more evenly.

certain p_i to not cover certain regions of the domain D as long as there is always at least one distribution able to sample from it. One can therefore use MIS to add specialized sampling for a certain part of D.[7]

7: We will use it to sample scatter directions from both the phase function and detector position.

6.2.3 Randomized Quasi Monte Carlo

In order to create random samples for the Monte Carlo method, one needs a source of randomness. Usually, one uses a pseudo-random number generator (PRNG) like e.g. Philox,[8] that while being a deterministic algorithm, produces a sequence of numbers that appear to be random [74, 75].

8: Mersenne Twister is still considered the gold standard but should not be used anymore. Vigna gives a great overview into the matter.

[74]: Vigna (2019), *It is high time we let go of the Mersenne Twister*

[75]: Salmon et al. (2011), 'Parallel random numbers: As easy as 1, 2, 3'

As Figure 6.2a shows, classic PRNG tend to cover the unit hypercube unevenly producing both dense and sparse spots. Depending on the shape of the integrand, this might lead to over-sample regions with vanishing contributions while ignoring the important ones. Instead, one can use so-called *low-discrepancy sequences*,[9] like the Sobol sequence [76], that are specifically constructed to circumvent this problem. If used in Monte Carlo, it is usually called *Quasi-Monte Carlo* (QMC). It has been shown that QMC often has a higher convergence rate of up to $\mathcal{O}(N^{-1})$ compared to the usual $\mathcal{O}(N^{-1/2})$.

9: Discrepancy is a measure on how clustered points are. We will not give a formal definition as it is an intuitively easy to grasp concept.

[76]: Sobol' (1967), 'On the distribution of points in a cube and the approximate evaluation of integrals'

A downside to QMC is that we lose the ability to estimate the error of the integral easily. It can be recovered by randomizing the points in the sequence for which a variety of methods exist, e.g. Owen-scrambling [77] as shown in Figure 6.2b. To differentiate from classic (Q)MC, this approach is called *Randomized Quasi-Monte Carlo* (RQMC). Additionally, for RQMC empirically an even higher convergence rate of up to $\mathcal{O}(N^{-3/2})$ has been observed [73, 78].

[77]: Owen (2003), 'Variance with alternative scramblings of digital nets'

[73]: Lemieux (2009), *Monte Carlo and Quasi-Monte Carlo Sampling*

[78]: L'Ecuyer (2016), 'Randomized Quasi-Monte Carlo: An Introduction for Practitioners'

6.3 Unidirectional Path Tracing

Of the two algorithms featured in this thesis, the *unidirectional path tracing* (UDPT) algorithm is the simpler one. Its core idea follows the one presented by Pharr et al. [46], but its actual design deviates from it. Conceptually the most significant difference is that this algorithm starts not at the sensor building paths towards light sources, but the other way around. The reasoning behind this decision is twofold: For one, it

[46]: Pharr et al. (2023), *Physically based rendering*

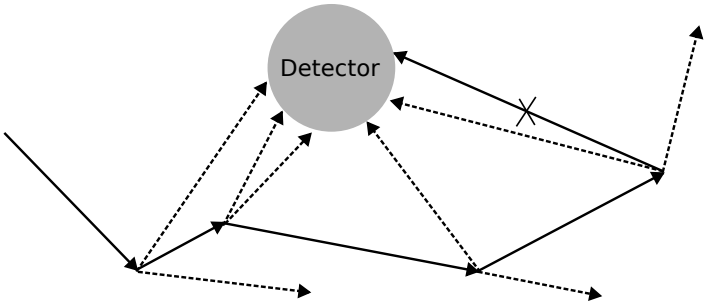

Figure 6.3: Illustration of the MIS used in the path sampling of UDPT. As a light path is constructed (solid lines), only at scatter events inside a volume two separate directions based on the phase function and detector position are sampled and extended until the detector is hit if possible (dashed lines). Hits that happened by chance like the last one have to be ignored.

makes it easier to define new light sources: Starting from the detector, one would need a light sampling function parameterized on the current ray's position[10], whereas in our case, the light itself starts the ray. Perhaps surprising, in the context of the equation of transfer, this means that we are transporting importance instead of radiance since we start at the light source and recursively solve for the incident importance.[11] There is a subtle change in handling specular transmission attached to it as described in Section 4.5. Adding polarization and finite light speed have been discussed in Section 5.3 and Section 6.1 respectively.

10: E.g. for Cherenkov radiation one would have to determine if a given point is reached by its cone.

11: A more intuitive reasoning is that we simulate ballistic photons, which carry energy instead of radiance.

6.3.1 Iterative Path Construction

The key insight from the path integrals is that while the individual integrals are independent of each other, we can still reuse parts of an already traced path. By incrementally building a light path, we can create for each volume scatter event an alternative path, where the next path segment is connected to the detector.[12] This also allows us to incorporate MIS, using both the phase function and detector position to sample the direction for the connecting segment, as illustrated in Figure 6.3, effectively decreasing the variance of the estimator and thus increasing the algorithm's performance. When using this approach, we have to ignore detector hits that are traced by chance, i.e. not by MIS, as this is not part of the estimator.

12: We always focus on a single detector per run to avoid the need to sort paths.

If the last event was an interface interaction, there is no point in sampling a direction based on the detector position, as the specular BSDF will always return zero. Instead, we try to extend either the reflected or transmitted ray to the detector.[13] The MIS weight is in this case trivially one.[14]

13: If we would also consider non-specular BSDF, the approach would be analog to the volume scattering approach.

14: Due to the delta distribution in the specular BSDF, only for the direction sampled from it the corresponding probability is non-zero. Looking at the requirements of MIS weights in Equation 6.17, this results in all other samples having a weight of zero. Subsequently, the BSDF sample needs a weight of one for all weights to sum up to one.

Starting at the light source, a new ray is initialized by sampling its radiance distribution. To the tracing algorithm this is a black-box function, to which it only has to provide a stream of random numbers, allowing it to be easily replaced. The ray contains the current state of the sampled light path, that is position, direction, elapsed time, wavelength, but also radiance and probability of the path, which are already combined in a *contribution* term[15] as expected by MC integration. If polarization is simulated, rays also include a Stokes vector and a unit vector $\hat{\boldsymbol{e}}_y$, indicating the corresponding reference frame, as discussed in Chapter 5.

15: In our implementation we split it into a linear and logarithmic part to minimize the use of logarithm and exponential function. The intention here is to reduce expensive calculations and to increase precision.

Propagation of the ray happens by iteratively sampling the next path segment and updating its state. First, a distance to the next scatter event is sampled, which is subsequently used to perform a ray query[16] against the scene. If a hit occurs, the sample probability is adjusted[17] and the intersection with the interface is simulated, otherwise scattering. If the medium the ray currently propagates does not scatter, a constant maximum distance is used instead. If no interface was hit, the ray is considered to be lost and the propagation stops. Rays outside a boundary box defining the limits of the simulation are treated similarly.

16: Ray queries checks for any surfaces in a given direction that are at most a certain distance away. See Section A.2 for a more detailed description.

17: For a hit the probability is to sample *at least* a distance d.

In the reference algorithm of Pharr et al. [46] to sample a segment's distance, one would importance sample the attenuation term (see Equation 4.13), i.e. an exponential function with parameter μ_t. We instead follow the suggestion of Jarabo et al. [79] and use a different, constant[18] term $\bar{\mu}$ for the exponential distribution to achieve a uniform distribution in the time spread of our light paths.

[46]: Pharr et al. (2023), *Physically based rendering*

[79]: Jarabo et al. (2014), 'A Framework for Transient Rendering'

18: In the previous approach μ_t may vary depending on medium and wavelength.

Interfaces show different behaviors upon interactions depending on their material. If it is marked as a detector and the tracing was initiated by MIS as described earlier, a hit is created, which is a non-zero contribution to the MC estimate. Hits contain the elapsed time and a measurement according to the measurement equation using a given sensor responsivity as described in Section 4.5. In addition, materials dictates how rays are updated, e.g. allowing or forbidding transmission and reflection. They can also be marked as absorbers stopping further light propagation or as medium border transitioning rays between media without refraction.

Volume scattering, on the other hand, is more straightforward: A new direction for the next segment is importance sampled from the medium's phase function. Simultaneously, two other directions are sampled for MIS: One is from the phase functions, and the other is based on the detector position, where we approximate the detector surface by an encapsulating sphere and sample a direction based on the visible hemisphere. These are used to prematurely finish a light path by extending them until they hit the detector, if possible.

For the computation to finish in finite time, we cannot create samples for all the infinite many integrals and instead stop propagating once we reach a maximum path length.[19] Since each event - be it volume scatter or interface interaction - attenuates the radiance substantially, we expect longer paths to contribute less to the final estimate. The bias introduced by this should, therefore, be minimal.[20] In the reference algorithm, the bias is reduced by randomly stopping the propagation earlier in a method known as *Russian roulette* [46]. This tends, as Jarabo et al. [79] pointed out, to sparse out samples for later arrival times, and thus, it was not implemented here. We can, however, stop propagation early when we expect consecutive samples to have zero or negligible contribution. In this implementation that assumption is fulfilled if a ray leaves a boundary box enclosing the detector geometry or its currently elapsed time crosses a maximum.

19: Path length refers to the amount of events or vertices and not the travelled distance.

20: Longer paths contribute more likely to later arrival times, so there is trade-off in choosing the maximal path length.

As already mentioned in Section 6.1, we can handle certain path lengths individually. Consecutively, these must be ignored in the iterative path construction, that is generating no hits. This makes the most sense for direct lighting, i.e. direct connections from the light source to the detector, as this does not require any path sampling. Instead, one tries to

extend the sampled light rays from the source until it hits the detector. Specialized sampling functions of the light source can further increase the performance of this approach.

Algorithm 1: Iterative Path Construction (*simplified*)

```
ray ← sampleLight()
allowHit ← AllowDirectLight
for 1..L_max do
    d ← sampleDistance()
    hit ← trace(ray, d)
    if hit then
        if hitDetector and allowHit then
            saveHit()
        end
        scatterInterface(ray)
        allowHit ← true
    else
        MISDetector(ray)
        scatterVolume(ray)
        allowHit ← false
    end
end
```

A nice side effect of using this approach of iteratively constructing paths is that all integrals in the MC simulation get the same amount of samples.[21] Take for instance, that we want to simulate N rays up to a path length $L_{\max}$. We will generate at most $N \cdot L_{\max}$ samples, but regardless of the actual distribution of samples generated, that is ignoring zero contributions, we can always sum all samples up and divide by N.

21: If a ray gets absorbed we immediately know subsequent samples will have zero contribution and thus do not need to explicitly sample them.

Finally, we bin the samples based on their elapsed time to generate light curves, i.e. measurement as a function of time. Mathematically, this is equivalent to applying a rectangular window to the measurement equation and reusing the same samples for different windows.

6.3.2 Path Contribution

Going back to the path integral formalism of Section 6.1, we write the probability of a specific path as the product of the probability of its path segments. Path segments are sampled as described earlier, with the only exception being the first segment's direction, which is sampled by the light source instead. We can thus write[22]

22: We omit MIS here to not clutter notation.

$$p(\boldsymbol{p}_0 \to \boldsymbol{p}_n) = p(\boldsymbol{p}_0 \to \boldsymbol{p}_1) \prod_{i=1}^{n-1} p(\boldsymbol{p}_{i-1} \to \boldsymbol{p}_i \to \boldsymbol{p}_{i+1}) \tag{6.20}$$

$$\begin{aligned} p(\boldsymbol{p}_{i-1} \to \boldsymbol{p}_i \to \boldsymbol{p}_{i+1}) = & p(\boldsymbol{\omega}_{i-1} \to \boldsymbol{\omega}_i) p(||\boldsymbol{p}_i - \boldsymbol{p}_{i+1}||) \\ & \cdot C_{\boldsymbol{p}_{i+1}}(\boldsymbol{p}_i, \boldsymbol{p}_{i+1}) / ||\boldsymbol{p}_i - \boldsymbol{p}_{i+1}||^2 \end{aligned} \tag{6.21}$$

$$p(d) = \begin{cases} \bar{\mu} e^{-\bar{\mu} d} & \text{if no hit} \\ e^{-\bar{\mu} d} & \text{if hit} \end{cases} \tag{6.22}$$

where the fractions stem from the Jacobian needed to transform the probability distributions from points in space to solid angles.

The factor $p(\boldsymbol{p}_0 \to \boldsymbol{p}_1)$ needs further clarification. In the algorithm, the direction and distance of the first segment is also sampled independently. To factorize it, however, we need to carry the corresponding Jacobian, which depends on the light source. A pencil beam, for instance, would require a Jacobian of simply $C_{\boldsymbol{p}}$, whereas an isotropic light source requires $C_{\boldsymbol{p}'}/r^2$. Luckily, the same Jacobian also appears on the emitted radiance and thus cancels when calculating the path's contribution.

Summarizing our mathematical consideration, a path's contribution is determined by the following equation

$$\begin{aligned}\frac{L(\boldsymbol{p}_0 \to \boldsymbol{p}_n)}{p(\boldsymbol{p}_n \to \boldsymbol{p}_0)} =& \frac{L_e(\boldsymbol{p}_0 \to \boldsymbol{p}_1)}{p(\boldsymbol{p}_0 \to \boldsymbol{p}_1)} \prod_{i=1}^{n-1} \frac{\hat{f}(\boldsymbol{\omega}_{i-1} \to \boldsymbol{\omega}_i)}{p(\boldsymbol{\omega}_{i-1} \to \boldsymbol{\omega}_i)} \frac{T_r(d_i)}{p(d_i)} \\ & \times V(\boldsymbol{p}_i \leftrightarrow \boldsymbol{p}_{i+1}) C_{\boldsymbol{p}_{i+1}}(\boldsymbol{p}_i, \boldsymbol{p}_{i+1})\end{aligned} \tag{6.23}$$

$$\frac{L_e(\boldsymbol{p}_0 \to \boldsymbol{p}_1)}{p(\boldsymbol{p}_0 \to \boldsymbol{p}_1)} = \frac{L_e(\boldsymbol{\omega}_0; \boldsymbol{p}_0) T_r(d_0)}{p(\boldsymbol{p}_0) p(\boldsymbol{\omega}_0) p(d_0)} \tag{6.24}$$

which finally needs to be multiplied by the sensor responsivity to form a complete MC sample. Note that the cosine dictated by Lambert's cosine law is included but cancels with the Jacobian of the probability for the path segment. An isotropic responsivity would therefore be constant one, regardless of the incident angle.

A substantial part of the fraction present in the product on the right side of Equation 6.23 cancel when applying importance sampling:[23]

$$\frac{\hat{f}(\boldsymbol{\omega}_{i-1} \to \boldsymbol{\omega}_i)}{p(\boldsymbol{\omega}_{i-1} \to \boldsymbol{\omega}_i)} \frac{T_r(d_i)}{p(d_i)} = e^{(\bar{\mu} - \mu_t) d_i} \cdot \begin{cases} \bar{\mu} & \text{if } \boldsymbol{p}_i \in A \\ \mu_s & \text{if } \boldsymbol{p}_i \in V \end{cases} \tag{6.25}$$

Similarly, ray queries can be considered to importance sample the visibility function V, effectively canceling it [46]. Additionally, as we only consider specular interface interaction, the cosine of the $C_{\boldsymbol{p}_{i+1}}(\boldsymbol{p}_i, \boldsymbol{p}_{i+1})$ term cancels with the one in the BSDF noted in Equation 4.12.

MIS can be added to the path contribution formula by appending an additional path segment $\boldsymbol{p}_n \to \boldsymbol{p}_{n+1}$

$$\frac{L(\boldsymbol{p}_0 \to \boldsymbol{p}_{n+1})}{p(\boldsymbol{p}_0 \to \boldsymbol{p}_{n+1})} = \frac{L(\boldsymbol{p}_0 \to \boldsymbol{p}_n)}{p(\boldsymbol{p}_0 \to \boldsymbol{p}_n)} \frac{T(\boldsymbol{p}_n \to \boldsymbol{p}_{n+1})}{p(\boldsymbol{p}_n \to \boldsymbol{p}_{n+1})} \tag{6.26}$$

$$\frac{T(\boldsymbol{p}_n \to \boldsymbol{p}_{n+1})}{p(\boldsymbol{p}_n \to \boldsymbol{p}_{n+1})} = \frac{\mu_s \tilde{\beta}(\boldsymbol{p}_{n-1} \to \boldsymbol{p}_n \to \boldsymbol{p}_{n+1}) T_r(d_{n+1})}{p_i(\boldsymbol{\omega_i})} \tag{6.27}$$

$$w_i = \frac{p_i(\boldsymbol{\omega_i})^2}{\sum_j p_j(\boldsymbol{\omega_i})^2} \tag{6.28}$$

where $p_i(\boldsymbol{\omega})$ is the i-th distribution for sampling the final direction towards the detector and w_i the MIS weights according to power heuristic. For the latter, we slightly deviated from its original definition by dropping the Jacobian from the individual probabilities to reduce complexity. Since this also satisfies the MIS condition in Equation 6.17, we still get an unbiased estimator.

23: If the material only allows for transmission or reflection, the corresponding probability will be 1. The factor from the Fresnel equation does not cancel out and needs to be applied.

[46]: Pharr et al. (2023), *Physically based rendering*

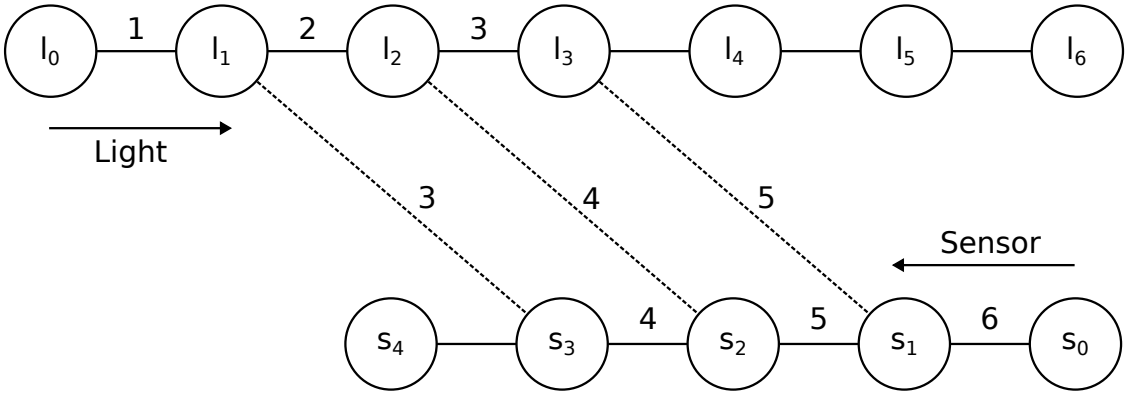

Figure 6.4: Illustration of connections between the light sub path $l_0 \to l_6$ and sensor sub path $s_0 \to s_4$ for generating light paths of length 6. Connections including l_0 or s_0 are not possible as they are part of the light source and sensor respectively, resulting in a total of 3 different light paths of that specific length.

6.4 Bidirectional Path Tracing

In the previous algorithm, we sampled the direction based on the detector position for the last segment resulting in a drastically increased hit rate compared to trying to hit the detector by chance. This approach, however, may fail if the detector is behind a surface as the ray cannot be fully extended to it.[24] Similarly, if the detector has a narrow viewing angle caused by its surroundings, most rays will not reach it either.

24: In that case one has to drop the MIS approach in the UDPT to still be usable.

Bidirectional path tracing (BDPT) tries to circumvent this problem by first sampling paths starting at the light and the sensor simultaneously and then connecting the generated sub-paths to create complete light paths. The algorithm was first introduced by Lafortune and Willems [80] and later independently by Veach [61] using the path integral formalism.[25] Here we build upon the implementation of Pharr et al. [81].

[80]: Lafortune et al. (1993), 'Bi-directional path tracing'

[61]: Veach (1997), 'Robust Monte Carlo Methods for Light Transport Simulation'

25: See Section 6.1.

[81]: Pharr et al. (2016), *Physically Based Rendering*

Constructing the individual sub-paths can again be done using algorithm 1, although with some minor tweaking: To start a ray at the sensor, we obviously need a separate sampling function. Propagating these, there is also a slight change in handling interfaces, as explained in Section 4.5. In case polarization is simulated, the ray carries a Mueller matrix instead of a Stokes vector.[26]

26: Since matrix multiplication is not commutative, in the implementation one has to pay attention to the order of the product changing depending on direction. See Section 5.3.

In our implementation, connecting two vertices from the light and sensor sub-path is only possible if both are scatter events and are in the same volume. Vertices on interfaces are not eligible as we only consider specular interactions. The corresponding BSDF consists of Dirac deltas and is thus zero almost everywhere, including the direction in which the other vertex lies. Given a light sub-path $\boldsymbol{l}_0 \to \boldsymbol{l}_n$ and a sensor sub path $\boldsymbol{s}_0 \to \boldsymbol{s}_m$, where the index 0 indicates their respective starts, we can calculate the contribution of the connected light path to the measurement:[27]

27: I is the measurement as defined in Equation 4.30

$$\begin{aligned}\frac{I}{p(I)} =& \frac{L(\boldsymbol{l}_0 \to \boldsymbol{l}_n)}{p(\boldsymbol{l}_0 \to \boldsymbol{l}_n)} \frac{W(\boldsymbol{s}_0 \to \boldsymbol{s}_m)}{p(\boldsymbol{s}_0 \to \boldsymbol{s}_m)} \cdot T_r(||\boldsymbol{l}_n - \boldsymbol{s}_m||) \\ & \mu_s^2 \tilde{\beta}(\boldsymbol{l}_{n-1} \to \boldsymbol{l}_n \to \boldsymbol{s}_m) \tilde{\beta}(\boldsymbol{l}_n \to \boldsymbol{s}_m \to \boldsymbol{s}_{m-1})\end{aligned} \tag{6.29}$$

Algorithm 2: Bidirectional Path Tracing (*simplified*)

```
ray ← sampleLight()
vertices ← ∅
for i ← 1..L_light do
    traceSegment()
    vertices[i] ← saveVertex(ray)
    updateRay(ray)                  // handles media interaction
end
ray ← sampleSensor()
for 1..L_sensor do
    traceSegment()
    for i ← 1..L_light do
        connect(ray, vertices[i])   // creates hit if successful
    end
    updateRay(ray)
end
```

In the reference implementation, there are also methods for connecting a sub-path to the light source or sensor respectively, which deviate from this formula. However, this is not included as we do not have a method to sample the light source from a given point and assume we cannot reliably sample the sensor from the light path.

Special care is needed if polarization is simulated: We apply the additional phase matrix corresponding to the two added scatterings to the respective sub paths and apply a suitable rotation in between to ensure both share the same reference frame. The final Stokes vector is then simply the product of the light paths Stokes vector and the Mueller matrix of the sensor sub-path.

Veach [61] proposed reweighing the final light paths of the same length using MIS to reduce variance and increase performance. This requires a substantial amount of bookkeeping in the algorithm making its implementation prone to errors. It is thus not included. However, we still want to retain the property of all individual path integral estimators sharing the same normalization factor to obviate the need to keep track of the samples' path lengths. We achieve this by dividing a sample's contribution by the number of possible ways to create a complete path of the same length before saving it.[28] This includes connections with interface vertices, although their contribution is trivially zero and thus not sampled as stated earlier. Given the maximum path length of the light sub-path L_l and sensor sub-path L_s, the number of possible connections to create a path of length L is

[61]: Veach (1997), 'Robust Monte Carlo Methods for Light Transport Simulation'

28: Conceptually, this equivalent to a constant MIS weight.

$$L_0 \coloneqq \max(L - L_l - 1, 1) \tag{6.30a}$$
$$S_0 \coloneqq \max(\min(L_s, L - L_0 - 1), 0) \tag{6.30b}$$
$$N = \min(L_l - L_0 + 1, S_0) \tag{6.30c}$$

Since we lack the capability of evaluating the light source and sensor distribution needed for creating a connection with $\boldsymbol{l}_0$ or $\boldsymbol{s}_0$, the minimal path length is three. To be able to create light paths of length one (direct lighting) and two, we can additionally create hits when the light sub-path hits the detector by chance, increasing the number of possible connections

for a given path length less or equal L_l by one. This approach, however, suffers likely from high variance. Alternatively, one can use the UDPT algorithm without MIS separately for path lengths of up to two and let it create more samples than the BDPT to compensate for the variance.[29]

29: Depending on the experiment setup, we might also conclude there is no contribution from shorter light paths and ignore them all together.

In the implementation of the algorithm, we first sample the light sub-path and store the corresponding vertices. Afterwards, we start tracing the sensor sub-path and eagerly try to connect its vertices with all stored light sub-path vertices without storing them. Unfortunately, the implementation has not yet been completed at the time of this writing.

7 Simulations

After introducing the physical models necessary to describe the propagation of polarized light through a medium, and algorithms that allow us to estimate it, we created a software framework implementing a corresponding simulation.

In this chapter, we first convince ourselves that the simulation is indeed correct and use it afterward to investigate the specific scenario of light propagation in deep oceanic water.

7.1 Light Propagation and Energy Conservation 45
7.2 Oceanic Water Simulation 48
7.3 P-ONE Demonstrator . . . 52

7.1 Light Propagation and Energy Conservation

It is difficult to verify that the simulation converges to the physically correct result without relying on experimental data, as there are hardly any experimental setups to which an analytical solution exists. Instead, we first simulate a setup where we expect to detect all photons. This not only allows us to check for energy conservation but also some early investigation on the impact of different parameters on the light propagation.

A very simplistic setup is used here: Inside a spherical detector of radius 30 m an isotropic light source producing a perfect monochromatic unpolarized delta pulse is placed at its center. Due to the monochromaticity, no dispersion effects are present; A medium with constant properties is thus sufficient. This further allows us to determine the expected absorption needed to check for overall energy conservation by determining the traveled distance of a photon via the elapsed time. We further use the Henyey-Greenstein phase function as it is easier to interpret with its single parameter alongside Kokhanovsky's model of the phase matrix, as shown in Figure 5.3. The latter is not that important as we expect no observable polarization effects due to the setup's unpolarized light source and symmetry.

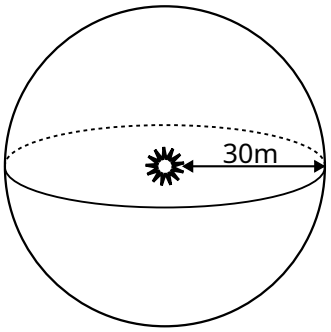

Figure 7.1: Illustration of the setup used to test for energy conservation: Spherical detector of 30 m radius with an isotropic unpolarized light source placed in its center.

For the start, we focus on the simulated scattering behavior. The first test varies the scattering coefficient while no absorption is present. A second run then sets it to $\mu_a = 0.05\,\mathrm{m}^{-1}$. Further, we chose $g = 0.0$ as parametrization of the Henyey-Greenstein phase function specifying uniform scattering behavior. To ensure the light curves are fully converged, we simulated 100 batches with 2 million paths, each up to 120 scattering events.[1] The results are shown in Figure 7.2.

From the simulated light curves without absorption, we can check for energy conservation by summing up the bins of the histograms, resulting in a fraction of detected photons above 99.9% for each of them. The slight difference to perfect detection is expected and caused by the missing contributions from paths longer than 120 scattering events. In case of absorption, we multiply the bins with a factor $\exp(\mu_a t v_g)$ to remove absorption, leading to similar results.[2] Including polarization in the simulation resulted only in a small difference, most likely caused by the finite numerical precision.

1: Normally we do not need that many samples and large paths. However, the simulation's design does not allow using MIS inside the detector and thus was disabled. Especially $\mu_s = 0.2\,\mathrm{m}^{-1}$ required this configuration.

2: Applying this factor to the bins instead of individual samples obviously introduces some error, as the distances do not match perfectly. Doing it the other way, results in values matching the one without scattering within errors expected from finite numerical precision.

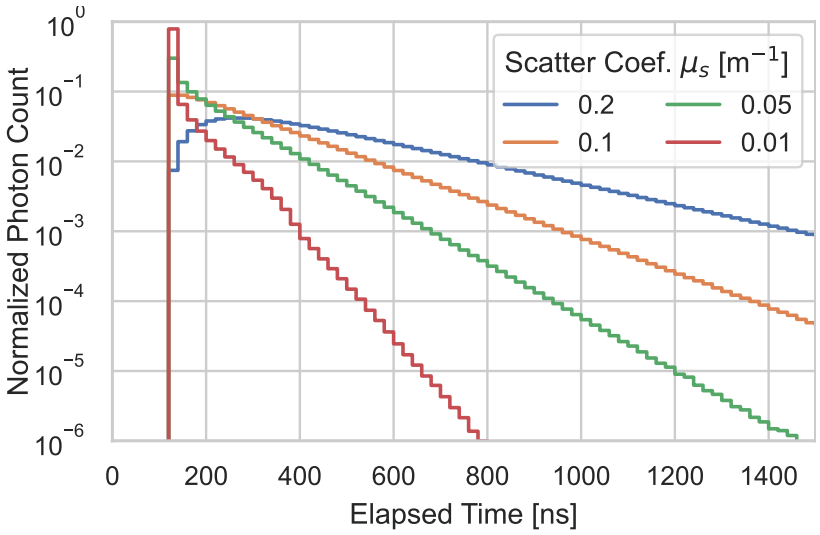

(a) Simulated light curves for varying scattering coefficients without absorption.

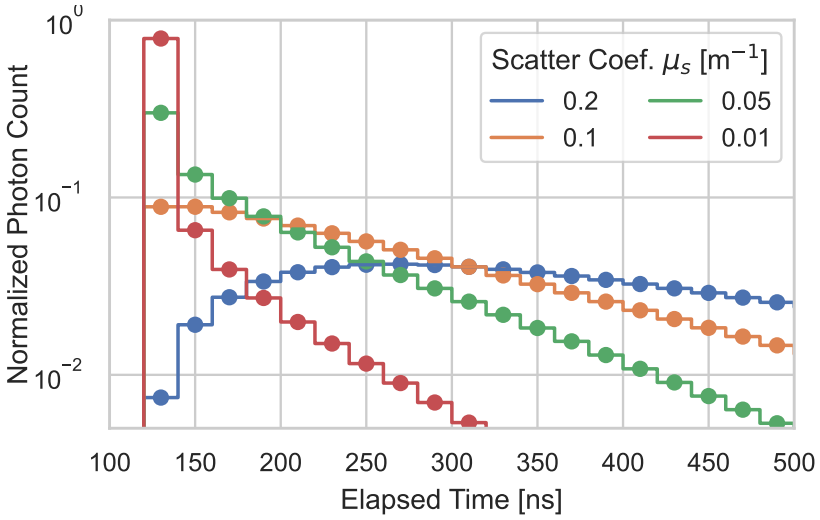

(b) Same light curve as above, but zoomed into earlier times. Added dots for better readability.

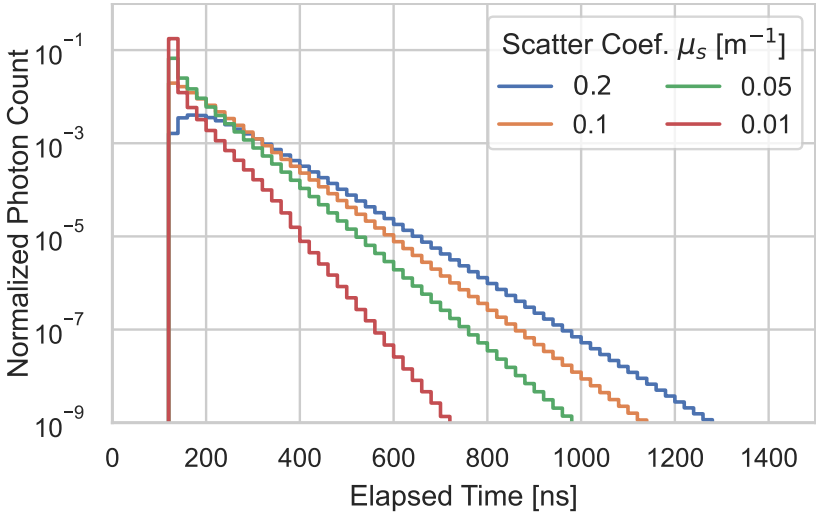

(c) Simulated light curves for varying scattering coefficients with a shared absorption coefficient of $\mu_a = 0.05\,\mathrm{m}^{-1}$.

Figure 7.2: Simulation of an unpolarized monochromatic light source inside a 30 m spherical detector producing a perfect delta pulse for varying scattering coefficients. The medium inside is dispersion-free with a (group) refractive index of $n = 1.33$. Scattering is described using the Henyey-Greenstein phase function with $g = 0$ indicating uniform scattering.

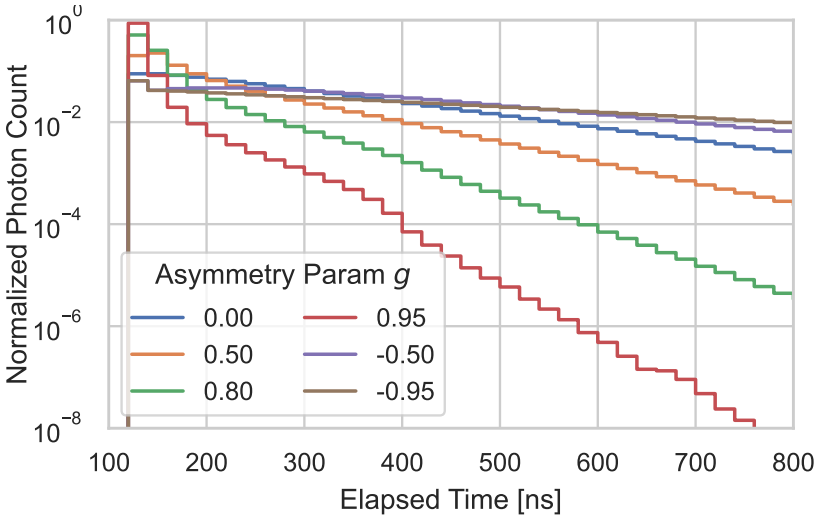

(a) Simulated light curves for varying asymmetry parameter g of the Henyey-Greenstein phase function.

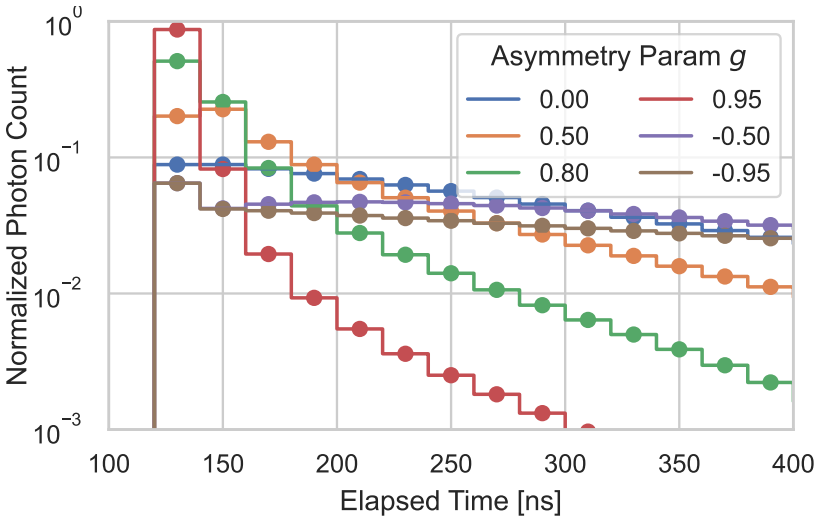

(b) Same light curve as above, but zoomed into earlier times. Added dots for better readability.

Figure 7.3: Simulation of an unpolarized monochromatic light source inside a 30 m spherical detector producing a perfect delta pulse for varying asymmetry parameter g. The medium inside is dispersion-free with a (group) refractive index of $n = 1.33$, a scattering coefficient of $\mu_s = 0.1\,\mathrm{m}^{-1}$ and no absorption $\mu_a = 0.0\,\mathrm{m}^{-1}$.

Even this simple setup allows us to make some statements about the effects of varying scattering and absorption coefficients on light propagation: Increasing the former flattens the light curve while increasing the latter both steepens and shrinks it. This is not surprising, as absorption reduces the available energy at later times, whereas scattering causes it to spread over time and distance. More interesting are the changes at the earliest hit times, as shown in Figure 7.2b. For small scattering coefficients, we observe a light pulse indicating that the distance between light source and detector was too short for the initial delta pulse to fully 'dissolve'. This effect shrinks with increasing scattering coefficient and is even reversed for large ones, where the light curve initially rises.

Next, we want to test our implementation for different phase functions by varying the asymmetry factor g of the Henyey-Greenstein phase function. The corresponding light curves are shown in Figure 7.3. As expected, we once more observed well above 99.9% of the photons thus verifying the simulation. Including polarization effects resulted again only in minimal

differences.

A useful property of the Henyey-Greenstein phase function is that its asymmetry factor g is also the cosine of the expected scattering angle: Positive values correspond to a bias to forward scattering and negative to backward scattering. Comparing with the simulated light curves in Figure 7.3, we see, that a bias to forward scattering moves the hits to earlier times, thus steepening the light curve, whereas backward scattering moves them to later times, effectively flattening it. It appears, however, that the steepening effect is more prominent than the flattening one.

7.2 Oceanic Water Simulation

After convincing ourselves that the implementation is correct, we want to use it to simulate the light propagation in oceanic water as found at the site of the proposed P-ONE neutrino telescope. The focus of this section is to develop a water model suitable for its simulation, use it to produce light curves for a single spherical detector, and conclude with a study on polarization effects on the detector.

7.2.1 Water Model

Since we will need it later, we want to create a model for the oceanic water at the Cascadia Basin, the future location of the P-ONE neutrino telescope. To our best knowledge, there is currently no definite model specific to that location available, so we must create our own. For the scattering coefficient, we will use the model based on Kopelevich and Mezhericher (Equation 4.22 on page 21), whereas for the absorption coefficient, we add to the pure water absorption measured by Smith an exponential correction as described in Section 4.2 on page 19. We repeat the formulas for better readability:[3]

$$\mu_s(\lambda) = 0.0017 \left(\frac{550}{\lambda}\right)^{4.3} + 1.34\nu_s \left(\frac{550}{\lambda}\right)^{1.7} + 0.312\nu_l \left(\frac{550}{\lambda}\right)^{0.3} \tag{7.1}$$

$$\mu_s(\lambda) = \mu_{a,\text{water}}(\lambda) + \mu_{a,0} \cdot \exp(-b \cdot (\lambda - 550)) \tag{7.2}$$

With the pathfinder experiment *STRAW* [8], some measurements of the optical properties at four different wavelengths already exist [82]. However, these do not separate absorption from scattering, reporting only the total attenuation coefficient.[4] Trying to numerically fit our model on the data results in zero scattering, which is not plausible as it undercuts the minimum expected scattering of pure water. While there exist measurements for other neutrino telescopes, such as KM3NeT [84] and Baikal-GVD [13], these appear to show very different optical properties and are thus not applicable to our case. Similarly, Petzold's [43] measurement, while including the deep Pacific Ocean, also shows larger coefficients than what was measured by STRAW. Instead, we will try to derive a model based on assumptions derived from the aforementioned data.

3: Again, λ has unit [nm] and μ_s [m^{-1}].

[8]: Boehmer et al. (2019), 'STRAW (STRings for Absorption length in Water): pathfinder for a neutrino telescope in the deep Pacific Ocean'

[82]: Bailly et al. (2021), 'Two-year optical site characterization for the Pacific Ocean Neutrino Experiment (P-ONE) in the Cascadia Basin'

4: In fact it is rather difficult to break down such measurements into absorption and scattering. The Baikal-GVD, for instance, has a dedicated contraption for measuring scattering [83].

[83]: Dvornicky (2023), 'Monitoring of optical properties of deep waters of Lake Baikal in 2021-2022'

[84]: Anassontzis et al. (2011), 'Light transmission measurements with LAMS in the Mediterranean Sea'

[13]: Ryabov et al. (2021), 'Monitoring of optical properties of deep lake water'

[43]: Petzold (1972), *Volume Scattering Functions for Selected Ocean Waters*

Petzold's measurement at three different depths of the Pacific Ocean suggest that the overall shape of the VSF is reasonably constant and differs between measurements only by a scaling factor α. As a first step, we therefore apply a scaling factor to his data[5] and then use it to determine v_s and v_l as shown in Section 4.3 on page 20. Both Anassontzis et al. and Rjabov et al. report a ratio between μ_s and μ_t in the region at 530 nm between approximately 15.0% and 20.0%, whereas Petzold finds about 25.0%. We will later tune the scaling factor to match a ratio of roughly 20.0% at this wavelength.

5: We use the data from Station 9. See Figure 4.6 on page 21

Once we determined μ_s, we subtracted it from the STRAW measurements to get an estimate for μ_a. After further subtracting the absorption of pure water, we can fit the exponential correction on the residuals. Repeating this for different α, we find model values that give us the desired ratio as listed in Table 7.1.

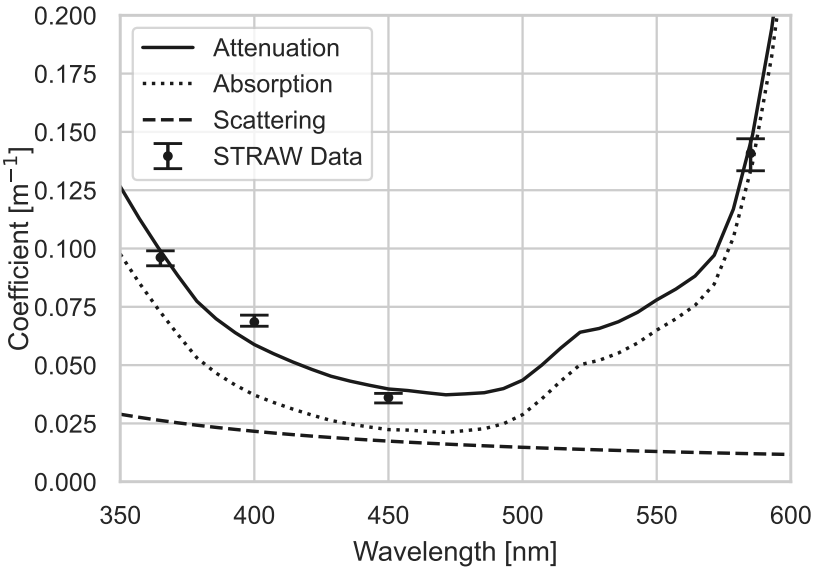

Param	Value
v_s	0.003 076 ppm
v_l	0.022 91 ppm
$\mu_{a,0}$	0.001 199 m^{-1}
b	0.018 78 nm^{-1}
α	0.3569

Table 7.1: Parameters for the model of deep Pacific Ocean water.

Figure 7.4: Model for absorption and scattering coefficients in the deep Pacific Ocean based on measurements by STRAW [82] and Petzold [43]. Tuned to give a ratio between μ_a and μ_s of roughly 80:20 at 530 nm.

[82]: Bailly et al. (2021), 'Two-year optical site characterization for the Pacific Ocean Neutrino Experiment (P-ONE) in the Cascadia Basin'

[43]: Petzold (1972), *Volume Scattering Functions for Selected Ocean Waters*

The model's scattering phase function is derived from the same VSF we used to determine the model parameters. Finally, the scattering phase matrix is the one measured by Voss [65], as shown in Figure 5.3 on page 30.

[65]: Voss et al. (1984), 'Measurement of the Mueller matrix for ocean water'

As a final remark, we want to emphasize that the model was created out of necessity based on limited data and makes no claim to be accurate. Ideally, it should be replaced by in-situ measurements.

7.2.2 Propagation Simulation

After developing a model of the optical properties, we first want to study its effects on light propagation. Mimicking the in-situ experiments to determine the optical properties, such as the calibration module in P-ONE [85], we simulate an isotropic spherical light source[6] alongside a spherical detector with a radius of 50 cm placed at varying distances. To make the interpretation easier, we model the time and wavelength spread of the light source to be perfect using a delta distribution. If one instead wants to take the finite precision of the light source into account, one needs to either fold its time spread into the light curves or incorporate it into the light model used by the simulation. Henningsen

[85]: Stacho et al. (2023), 'Development of Calibration Light Sources for the Pacific Ocean Neutrino Experiment'

6: The real light source is necessarily not perfectly isotropic as its mounting structure blocks certain viewing angles. Since the scattering in water is highly forward biased, this should have a negligible effect as long as the line of sight to the detector is far away from these angles.

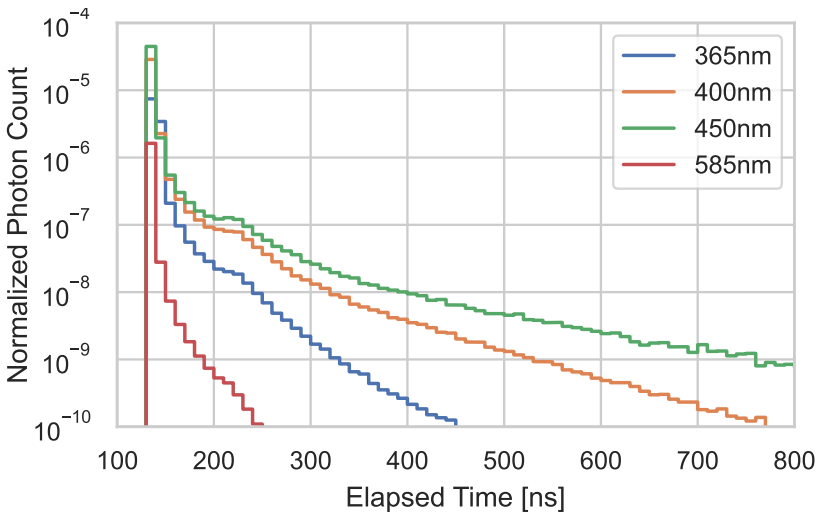

(a) At a fixed distance $d = 30\,\mathrm{m}$ for varying wavelengths.

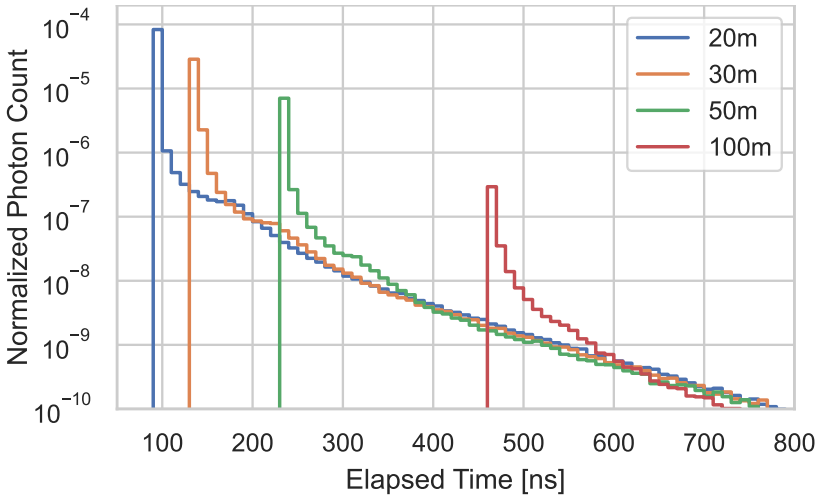

(b) At a fixed wavelength $\lambda = 400.0\,\mathrm{nm}$ for varying distances.

Figure 7.5: Simulation of an isotropic spherical light source in water as modeled in Section 7.2.1 detected by a spherical target with a radius of 50 cm. Spread in time and wavelength are modeled by a delta distribution. Light curves produced both for varying wavelength and distance.

[86]: Henningsen (2018), 'Optical Characterization of the Deep Pacific Ocean: Development of an Optical Sensor Array for a Future Neutrino Telescope'

[86], for example, reports for the flash in STRAW a Gaussian spread with a full width at half maximum (FWHM) between roughly 4 and 8 ns, depending on wavelength.

Figure 7.5 shows the simulated light curves. Varying the wavelength while keeping the distance fixed results in similar effects as seen in Figure 7.2 due to the attenuation coefficient being a function of the wavelength. The height of the initial peak scales with corresponding attenuation coefficient (see Figure 7.4) in line with expectations.

Comparing the light curves at different distances, we see that even at 100 m there is still a peak observable, although it has started to spread in time. Since the scattering is mostly forward, the light beams 'dissolve' only slowly. While both absorption and scattering cause the attenuation of the peak height, the spread of the peak is exclusively caused by the latter. Therefore, in theory, it is possible to recover both coefficients by performing measurements at different distances.[7]

7: Using a different setup, this has been shown by Ryabov et al. [13].

[13]: Ryabov et al. (2021), 'Monitoring of optical properties of deep lake water'

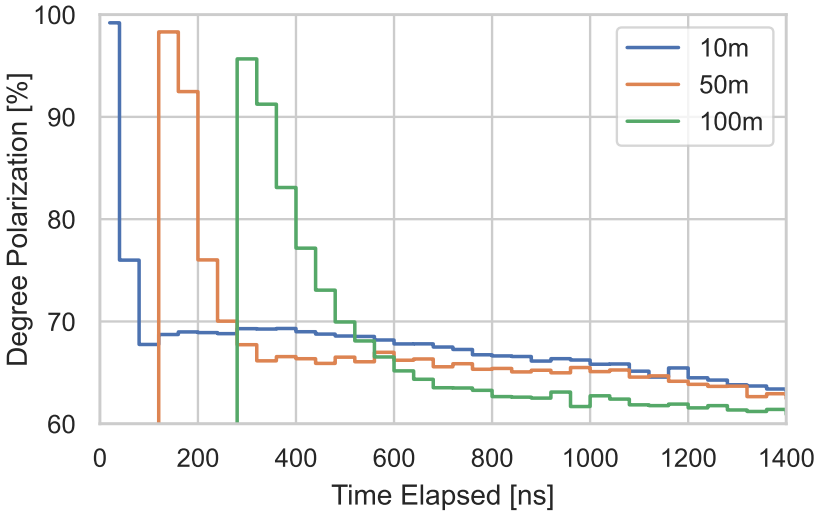

Figure 7.6: Observed polarization degree of light originating from a Cherenkov track created by a particle traveling at the speed of light at various distances to the detector as a function of time. The particle track is 200 m long with a minimal distance to the detector at its midpoint marking also the zero time point. The labels describe this shortest distance.

7.2.3 Polarization Study

After showing in Subsection 2.2.2 on page 6 that Cherenkov tracks as the main source of light in neutrino telescopes are fully linear polarized, and in Section 3.4 on page 13 that PMTs are sensitive to it at certain angles, we still have to investigate whether polarization survives the propagation in water. An easy first test is to check how much polarization makes it from a Cherenkov track to a detector. We measure this using the degree of polarization (Equation 5.4 on page 27) as this is independent of the chosen reference frame of the Stokes vector. Figure 7.6 shows unsurprisingly that the initial light peak is highly polarized with a broadening for larger distances similar to those in Figure 7.5. However, even after the initial pulse, the light remains at a high degree of polarization.

As shown in Section 3.4 on page 13, PMTs in water are only sensitive to polarization at an incident angle of around 45°. While this seems to be disadvantageous at first glance, it can actually be exploited. Since the optical modules in P-ONE consist of multiple PMTs, each facing a different direction, chances are that for a polarized light front, some of them observe it at this angle while others do not. In the best case, at least two PMTs are sensitive to the polarization, with their orientation being perpendicular to each other when projected to the plane of the light front. Then, in their respective plane of incidence, the horizontal and perpendicular components are effectively swapped, allowing, in theory, to directly determine the polarization.[8]

Finally, to see if there is a chance to measure the orientation of the polarization as described earlier, we want to simulate a Cherenkov track producing a linear polarized light front hitting a spherical detector and check the polarization at locations observing this front at an incidence angle of around 45°. The setup is illustrated in Figure 7.7: An up-going particle track at the speed of light is oriented such that the light front hits the front of the detector sphere normal to its surface. The distance between the track and the detector is about 5 m at the closest point. We record the Stokes vector in the local plane of incidence around three different points on the sphere, each satisfying the conditions mentioned above for an angular distance up to 22.5°. The missing fourth point was

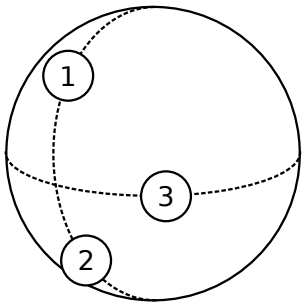

Figure 7.7: Setup for simulating the anisotropy of the received light from a Cherenkov track at a spherical detector. The Q parameter of the Stokes vector is measured separately for the shown locations. Simulated light stems from a Cherenkov track going upwards and oriented such that the light front is normal to the sphere's surface at the cross.

8: Remember, that Cherenkov light is fully linear polarized (see Subsection 2.2.2 on page 6) and scattering in Ocean water does not introduce any circular polarization (see Figure 5.3 on page 30).

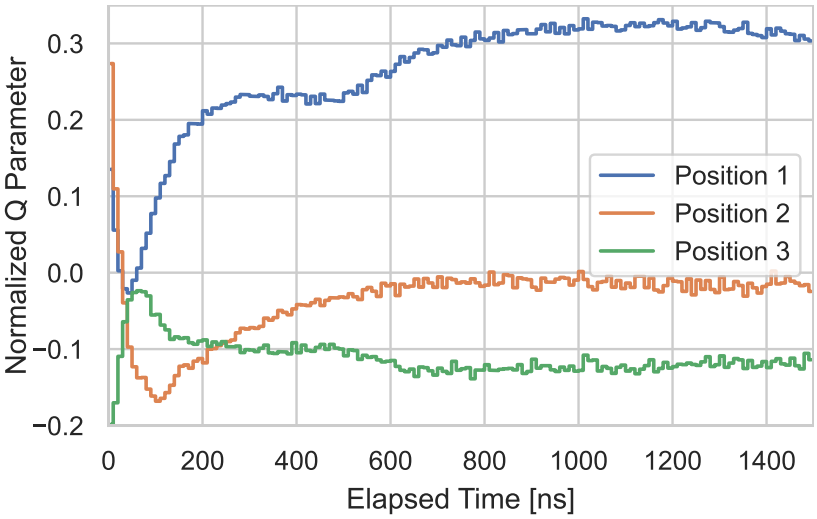

Figure 7.8: Simulated Q parameters of the local Stokes vector at the positions described in Figure 7.7 as a function of time.

9: See Figure 7.5.

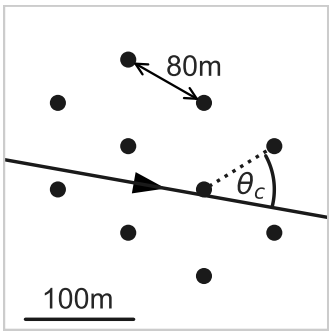

Figure 7.9: Preliminary design of the P-ONE demonstrator (P-ONE 10) according to Henningsen [32] showing the individual positions of the strings with 80 m in between. Dashed line is the simulated Cherenkov track chosen such that a certain P-OM blocks another one (θ_C denotes the Cherenkov angle).

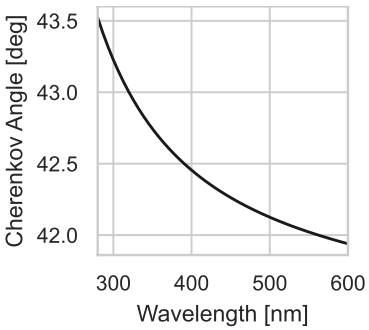

Figure 7.10: Cherenkov angles in water as function of wavelength.

10: See Section 2.3 on page 9

[32]: Henningsen (2023), 'Pacific Ocean Neutrino Experiment: Expected performance of the first cluster of strings'

11: Due to dispersion, the exact angle becomes a function of wavelength. See Figure 7.10.

omitted as it is expected to produce the same results as the third due to symmetry.

Figure 7.8 shows the results of the simulation: For the early light peaks,[9] there is a large difference in polarization between positions 2 and 3. Since these peaks contain most of the detected light, there is a good chance to be able to determine the polarization in real detectors. Even at later times, there is still a noticeable difference in polarization between the different locations. However, as we typically expect less light at later times, this is most likely less relevant.

As a final remark on the polarization study, we want to emphasize that this is a relatively simple test to determine whether the simulation of polarization is worthwhile at all. More sophisticated simulations involving a better understanding of the specific PMTs used are necessary to reach a final conclusion.

7.3 P-ONE Demonstrator

Finally, this section includes a simulation of a single horizontal Cherenkov track as it is detected by a preliminary design of the P-ONE demonstrator (P-ONE 10) consisting of 10 strings totaling in 200 P-OMs[10] according to the design shown by Henningsen [32]. We will use this setting to investigate the impact the self-shadowing in the neutrino telescope caused by cables and other P-OMs blocking each other's line of sight to the light source. For this reason, we chose a Cherenkov track of a particle traveling at the speed of light passing a specific P-OM at a distance of 5 m, as shown in Figure 7.9, and aligned it such that the line of sight to the P-OM behind is under an angle of roughly 42.5° corresponding to opening angle of the Cherenkov cone at 400 nm.[11] Figure 7.9 illustrates the setup.

To consider the finite optical window of the glass hemispheres enclosing the P-OMs, we limit the wavelength to a range of 320 nm to 700 nm. The P-OM themselves are not simulated. The produced light curves describe the total amount reaching them, ignoring any intrinsic efficiency

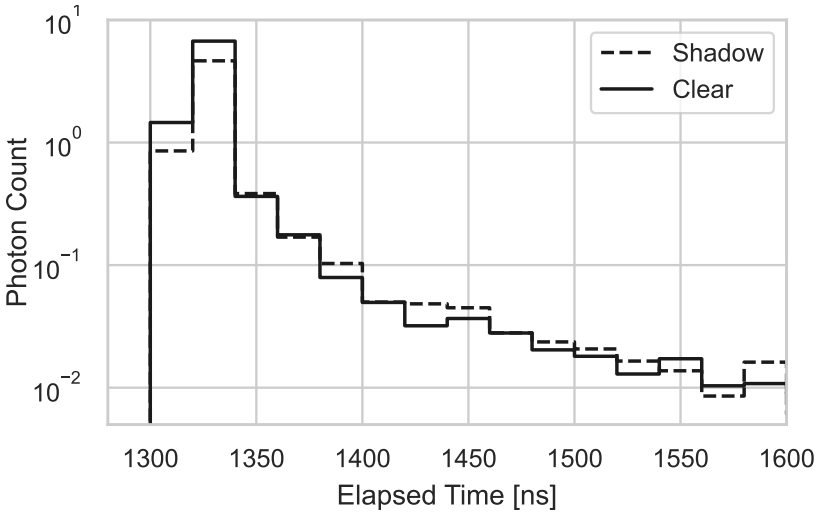

Figure 7.11: Light curves for the shadowed P-OM comparing the impact of including shadowing into the simulation.

and geometric effects. The model describing the ocean water's optical properties is once again the one derived in Section 7.2.1.

Figure 7.12 shows an illustration of the simulation results. As expected, only the P-OMs close to the particle track receive light in a noteworthy amount. Already at two P-OMs below or above, hardly any light is observed. However, the illustration is not enough to draw a conclusion about the impact of shadowing in the detector. Comparing their corresponding light curves shown in Figure 7.11, we see that shadowing causes the initial peak carrying most of the light to shrink, whereas the diffuse rest remains the same. Putting this into numbers, the total amount of received light in this simulation shrinks from about 9.1 to 6.5 photons. Thus, shadowing has a measurable impact in certain situations, making it worthwhile to include in simulations.

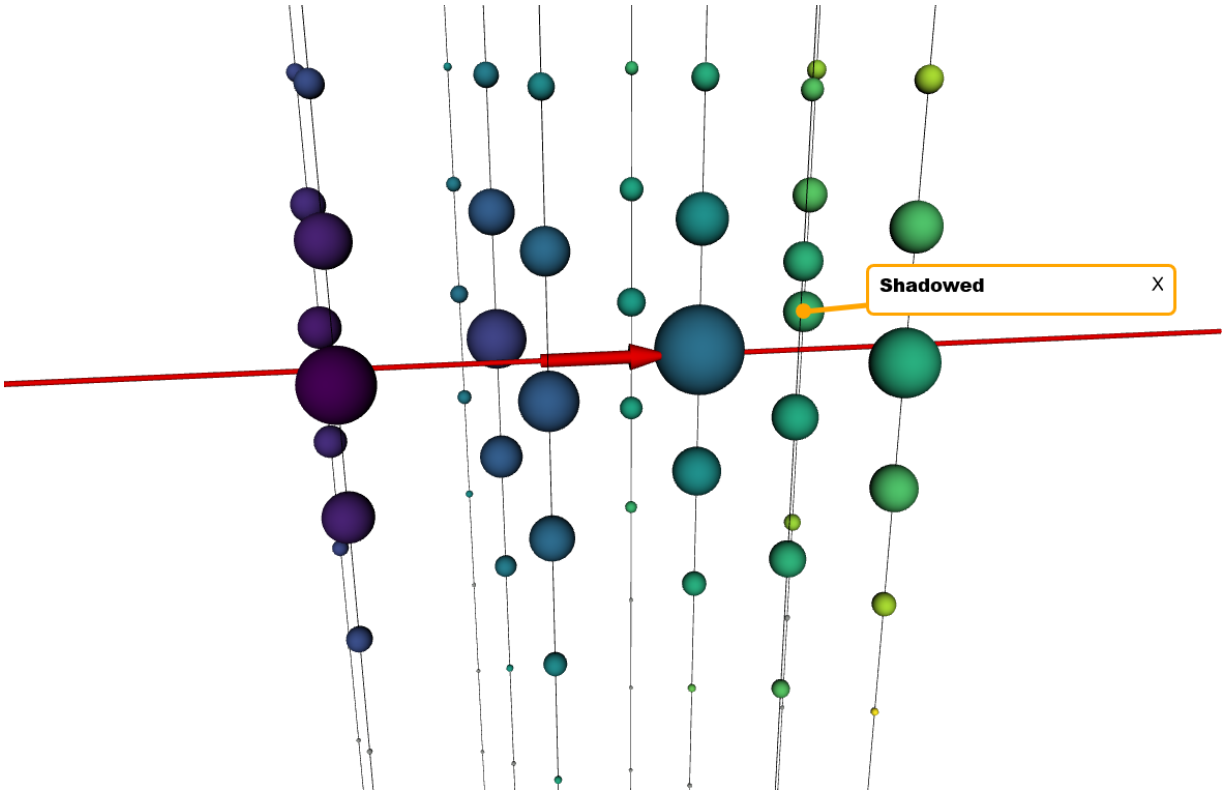

(a) Front view

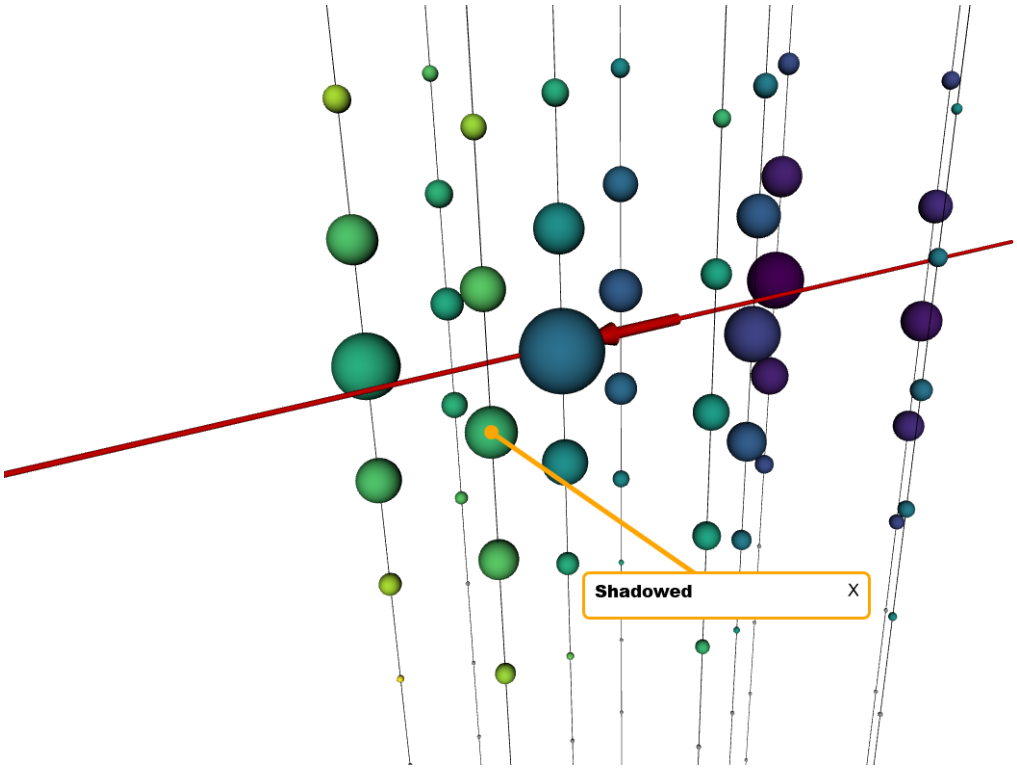

(b) Back view

Figure 7.12: Illustration of the simulated Cherenkov track detected by the preliminary P-ONE demonstrator setup. Sphere corresponds to the individual P-OMs, with size being proportional to the logarithmic amount of received light and color corresponding to the time of the earliest light seen. Marked P-OM is expected to be in the shadow of another P-OM with respect to the Cherenkov light.

8 Conclusion

During the course of this thesis, we developed a Monte Carlo simulation for polarized light propagation tailored explicitly toward the setting of a neutrino telescope placed in the deep ocean. We started by introducing the broader topic of neutrino astronomy and the working mechanism of neutrino, where we placed a special focus on P-ONE as the main target of our simulation. As the Cherenkov light used as a proxy to detect neutrinos in the telescope is compared to the latter's size rather faint in the regime of single photons detected, we concluded that a good understanding of the light propagation is essential, thus motivating this work.

A substantial part was dedicated to introducing and investigating the effects influencing light propagation and whether these are large enough to be worthwhile to add to the simulation. Besides the classic ones, such as the Fresnel terms describing interactions at boundaries between media, absorption and scattering, we also include polarization effects. In contrast, refraction within the ocean water and inelastic scattering were deemed negligible. Including polarization effects in PMT based detectors is unusual as they are typically reported to be insensitive to it. As we showed, however, this changes when operating in water at incidence angles around 45°, making it interesting to multi PMT setups such as the P-OM found in P-ONE.

Starting from the Equation of Transfer, a physical model describing the propagation of radiance through a medium, we derived path integrals as a more suitable version of it for application with the later introduced Monte Carlo methods. More sophisticated alterations of the classic Monte Carlo were shown with Multiple Importance Sampling and Randomized Quasi Monte Carlo. Combining the physical model with the computational methods, we presented two algorithms for simulating light propagation: Unidirectional Path Tracing starting from the light source, and Bidirectional Path Tracing combining two light paths starting from both the light source and detector. However, the latter is not yet operational.

To verify the algorithm, it was first tested by means of energy conservation for different media. Finally, simulations were performed to investigate the propagation of light originating from Cherenkov tracks in ocean water as well as shadowing in the preliminary demonstrator setup of P-ONE. For this, a water model based on the LiDAR data of STRAW-b was developed. Both polarization and shadowing were shown to produce a measurable effect in these simulations, although their respective setup was chosen to emphasize these effects.

In this thesis, we laid the groundwork for a sophisticated simulation of the propagation of light from Cherenkov tracks in P-ONE. Because of its unspecific design, it can, in theory, also be applied to other experiments. However, there is still room for improvement in future work: To produce more accurate estimates in P-ONE, a better understanding of the properties of the ocean water and PMTs are necessary. Likewise, the algorithm

itself is not perfect. Since ray tracing is an active field of research, there is a continuous stream of newer and better algorithms one might want to implement in newer versions of the simulation.

GPGPU Programming A

A.1 GPU Execution Model . . 57
A.2 Hardware Accelerated Ray Tracing 58

Although GPUs were initially designed to render images, their massively parallel architecture makes them favorable for algorithms being able to take advantage of it, including MC simulations such as the one presented in this thesis. In fact, among the ten best contestants in the TOP500 supercomputer ranking, only one does not utilize GPUs [87]. Additionally, modern GPUs possess dedicated hardware to accelerate the calculation of intersections between geometric rays and polygon meshes [88], which is a crucial part of the algorithms presented in Chapter 6.

[87]: Strohmaier et al. (2023), *November 2023 | TOP500*

[88]: Marrs et al. (2021), *Ray Tracing Gems II*

Neither a description of GPU architectures nor an introduction to *General Purpose Computation on Graphics Processing Unit* (GPGPU) fits within the scope of this thesis. Instead, we focus on the parts that influenced the design decisions of the algorithms presented in Chapter 6, namely the execution model of GPUs and hardware-accelerated ray tracing. For a thorough discussion, we refer to Hennessy et al. [89], on which the following section is based.

[89]: Hennessy et al. (2017), *Computer Architecture*

A.1 GPU Execution Model

Comparing CPUs with GPUs, their design goal is fundamentally different: CPUs are optimized for latency to finish a single task as fast as possible, GPUs, on the other hand, focus on throughput, that is, finishing in a given time as much as possible. The core ingredient to achieve this is massive parallelism: While CPUs typically have a comparably low number of cores mainly running independent threads,[1] GPUs show a massive amount in the thousands[2] grouped into units of typically 32 to 64 called *warps*[3] each executing the same instruction in lockstep. In combination with branching code paths caused by e.g. if-else instructions, hefty performance penalties can occur: Since each thread in a warp executes the same instructions, each one has to traverse all branches albeit accordingly masked. One should, therefore, try to make algorithms as linear as possible.

1: *Core* describes the physical unit, *thread* the sequence of instructions it runs and *kernel* the corresponding program.

2: The Nvidia RTX 4090 for example has 16384 cores [90].

3: Unfortunately, naming differs between GPU vendors and APIs. Here we will adopt the one introduced by Nvidia.

[90]: Nvidia (2023), *Nvidia Ada GPU Architecture*

The iterative path construction algorithm introduced in subsection 6.3.1 is notoriously bad in terms of branching: Depending on whether the next path segment intersects an interface, fundamentally different code paths are executed. Additionally, the loop responsible for creating the segments cannot be aborted early as long as a single thread in the warp is not yet finished. *Wavefront path tracing* [91] is an approach that tries to solve this by splitting the algorithm into linear kernels that handle different tasks like volume scattering or interfaces. Instead of branching, inputs for the consecutive kernels are written to memory. While this ensures maximum convergence of threads in a single warp, it also increases the pressure on memory bandwidth, making it the new bottleneck. We did not implement this approach as we expect in the simulation of neutrino telescopes mostly volume scattering and thus little branching anyway. It appears other simulation software, such as Mitsuba 3, did not either [92, 93].

[91]: Laine et al. (2013), 'Megakernels considered harmful: wavefront path tracing on GPUs'

[92]: Jakob et al. (2022), *Mitsuba 3 renderer*
[93]: Jakob et al. (2022), 'Dr.Jit: A Just-In-Time Compiler for Differentiable Rendering'

GPUs cannot access the video memory on a byte to byte basis but have to request larger blocks instead. Keeping the nature of warps in mind, it is worthwhile to organize lists of data such that individual parameters are consecutive, e.g. instead of an array of vectors, use an array for each component.[4] This ensures that a single read instruction is sufficient to provide data to all warps [46]. Even with optimized data layout, fetching data from video memory is comparably expensive.[5] This causes latency the *warp scheduler* tries to amortize by swapping the current warp with a different one while waiting for the data to be available. Therefore, to optimally utilize a GPU one needs to issue more threads than there are physical cores. In our case, this is trivially achieved by increasing the sample count of the MC estimate.

4: This is known as *structure of arrays*.

[46]: Pharr et al. (2023), *Physically based rendering*

5: Fetching a cache line typically takes 100 cycles.

A.2 Hardware Accelerated Ray Tracing

Hardware-accelerated ray tracing has existed for quite a time but only became readily available since the introduction of RTX and the Turing architecture by Nvidia in 2018 [94, 95]. Its implementation is vendor-specific but is nowadays accessible in a cross-platform and cross-vendor way by using e.g. the Vulkan API [96]. The following briefly introduces its concepts based on the Vulkan specification.

[94]: Sanzharov et al. (2020), 'Survey of Nvidia RTX Technology'

[95]: Nvidia (2018), *Nvidia Turing GPU Architecture*

[96]: The Khronos® Vulkan Working Group (2024), *Vulkan® 1.3.285*

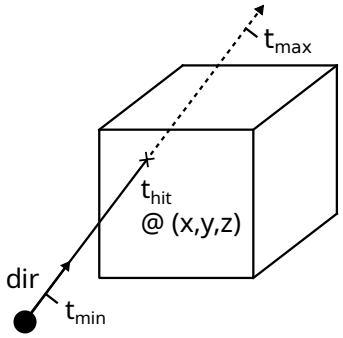

Figure A.1: Illustration of a ray tracing operation. After specifying origin, direction and a distance range $[t_{\text{min}}, t_{\text{max}}]$, ray tracing determines whether an object was hit, and if so which object was hit and the hit's position in both coordinates and distance t_{hit}.

At its core, ray tracing is essentially a method to perform ray intersections with a given scene; that is, after specifying a ray's origin, direction and length, it determines whether it intersects the scene and, if so, which part where. Vulkan provides two approaches to utilize this in software: *Ray queries* are designed as simple function calls, whereas *ray tracing pipelines* require the code to be split into parts, each responsible for different parts of the ray traversal such as ray generation, intersection and miss. In this work, we used the former as it is easier to incorporate.

In preparation for performing ray tracing operations, the scene rays are traced against is compiled into an *acceleration structure* (AS) consisting of multiple *bottom level AS* (BLAS) containing the individual polygon meshes and a single *top level AS* (TLAS) referencing BLAS with a corresponding transformation.[6] Each BLAS is assigned a consecutive ID and in addition, TLAS can also assign a custom one to each reference. We used the former to assign materials, whereas the latter is used to identify individual detectors, allowing them to share the same BLAS. The location of ray intersections is reported in the reference frame of the BLAS, i.e. without applying the transformation specified by the TLAS. However, the latter is also included to allow the calculation of the position in the scene's reference frame. This fits nicely in our model, where we define the detector's response function as independent of the actual detector position and orientation.

6: Transformations are specified as matrices and contain beside scaling and rotation, also translation.

While all this is also possible to implement in a classic fashion on CPUs or GPUs, it is quite a complex computation. In hardware accelerated ray tracing this is baked into a dedicated part of GPU, allowing it not only to perform this task much faster, but also its main cores to perform other calculations simultaneously [95].

Source Code B

This work resulted in two distinct software packages, both published under the MIT license:

Hephaistos

Hephaistos is a GPGPU framework based on the Vulkan API, providing the underlying layer to control and access the GPU in a cross-platform and cross-vendor manner similar to CUDA. Although it was motivated by the development of the simulation software, its design makes no assumption on the specific task, allowing it to be used for different tasks, too. It is written in C++ and provides Python bindings. For the latter, prebuilt binaries for all common platforms are available. Its source code can be found under the following address:

`https://github.com/tkerscher/hephaistos`

Theia

Theia is a framework for simulating polarized light, implementing the methods shown in this work, making it its main product. It is written in Python using Hephaistos for GPU acceleration. Its source code can be found under the following address:

`https://github.com/tkerscher/theia`

Bibliography

[1] Alexus McLeod. *Astronomy in the Ancient World: Early and Modern Views on Celestial Events*. Springer International Publishing, 2016 (cited on page 1).

[2] Maurizio Spurio. *Particles and Astrophysics. A Multi-Messenger Approach*. Springer Cham, Oct. 2014 (cited on pages 1, 3, 5, 6, 8).

[3] A. Karle et al. 'IceCube — the next generation neutrino telescope at the South Pole'. In: *Nuclear Physics B - Proceedings Supplements* 118 (2003). Proceedings of the XXth International Conference on Neutrino Physics and Astrophysics, pp. 388–395. DOI: https://doi.org/10.1016/S0920-5632(03)01337-9 (cited on pages 1, 5, 8).

[4] IceCube Collaboration et al. 'Neutrino emission from the direction of the blazar TXS 0506+056 prior to the IceCube-170922A alert'. In: *Science* 361.6398 (2018), pp. 147–151. DOI: 10.1126/science.aat2890 (cited on pages 1, 3).

[5] U.F. Katz. 'KM3NeT: Towards a km3 Mediterranean neutrino telescope'. In: *Nuclear Instruments and Methods in Physics Research Section A: Accelerators, Spectrometers, Detectors and Associated Equipment* 567.2 (2006). VLVnT2, pp. 457–461. DOI: https://doi.org/10.1016/j.nima.2006.05.235 (cited on pages 1, 5).

[6] A.V. Avrorin et al. 'Deep-Underwater Cherenkov Detector in Lake Baikal'. In: *Journal of Experimental and Theoretical Physics* 134.4 (Apr. 2022), pp. 399–416. DOI: 10.1134/s1063776122040148 (cited on pages 1, 5).

[7] Lisa Johanna Schumacher et al. 'PLEνM: A global and distributed monitoring system of high-energy astrophysical neutrinos'. In: *Proceedings of 37th International Cosmic Ray Conference — PoS(ICRC2021)*. ICRC2021. Sissa Medialab, July 2021. DOI: 10.22323/1.395.1185 (cited on page 1).

[8] M. Boehmer et al. 'STRAW (STRings for Absorption length in Water): pathfinder for a neutrino telescope in the deep Pacific Ocean'. In: *Journal of Instrumentation* 14.02 (Feb. 2019), P02013–P02013. DOI: 10.1088/1748-0221/14/02/p02013 (cited on pages 1, 10, 48).

[9] Immacolata Carmen Rea et al. 'P-ONE second pathfinder mission: STRAW-b'. In: *Proceedings of 37th International Cosmic Ray Conference — PoS(ICRC2021)*. ICRC2021. Sissa Medialab, Aug. 2021. DOI: 10.22323/1.395.1092 (cited on pages 1, 10).

[10] Matteo Agostini et al. 'The Pacific Ocean Neutrino Experiment'. In: *Nature Astronomy* 4.10 (Sept. 2020), pp. 913–915. DOI: 10.1038/s41550-020-1182-4 (cited on pages 1, 5, 9).

[11] Paweł Malecki. 'Pacific Ocean Neutrino Experiment'. In: *Universe* 10.2 (Jan. 2024), p. 53. DOI: 10.3390/universe10020053 (cited on pages 1, 9).

[12] M. Ackermann et al. 'Optical properties of deep glacial ice at the South Pole'. In: *Journal of Geophysical Research: Atmospheres* 111.D13 (July 2006). DOI: 10.1029/2005jd006687 (cited on page 1).

[13] Evgenii V Ryabov and Boris Tarashchansky. 'Monitoring of optical properties of deep lake water'. In: *Proceedings of 37th International Cosmic Ray Conference — PoS(ICRC2021)*. ICRC2021. Sissa Medialab, July 2021. DOI: 10.22323/1.395.1034 (cited on pages 1, 48, 50).

[14] Wolfgang Pauli. *Scientific Correspondence with Bohr, Einstein, Heisenberg a.o. 1930–1939*. Ed. by Karl von Meyenn. Vol. 2. Berlin Heidelberg: Springer-Verlag, 1985 (cited on page 3).

[15] Edoardo Vitagliano, Irene Tamborra, and Georg Raffelt. 'Grand unified neutrino spectrum at Earth: Sources and spectral components'. In: *Rev. Mod. Phys.* 92 (4 Dec. 2020), p. 045006. DOI: 10.1103/RevModPhys.92.045006 (cited on pages 3, 8).

[16] Matthias Bartelmann. 'Development of Cosmology: From a Static Universe to Accelerated Expansion'. In: *From Ultra Rays to Astroparticles. A Historical Introduction to Astroparticle Physics*. Ed. by Brigitte Falkenburg and Wolfgang Rhode. Springer Dordrecht, Dec. 2012. DOI: https://doi.org/10.1007/978-94-007-5422-5 (cited on page 4).

[17] Sheldon L. Glashow. 'Resonant Scattering of Antineutrinos'. In: *Phys. Rev.* 118 (1 Apr. 1960), pp. 316–317. DOI: 10.1103/PhysRev.118.316 (cited on page 5).

[18] M. G. Aartsen et al. 'Detection of a particle shower at the Glashow resonance with IceCube'. In: *Nature* 591.7849 (Mar. 2021), pp. 220–224. DOI: 10.1038/s41586-021-03256-1 (cited on page 6).

[19] Amanda Cooper-Sarkar, Philipp Mertsch, and Subir Sarkar. 'The high energy neutrino cross-section in the Standard Model and its uncertainty'. In: *Journal of High Energy Physics* 2011.8 (Aug. 2011). DOI: 10.1007/jhep08(2011)042 (cited on page 6).

[20] V. Barger et al. 'Glashow resonance as a window into cosmic neutrino sources'. In: *Phys. Rev. D* 90 (12 Dec. 2014), p. 121301. DOI: 10.1103/PhysRevD.90.121301 (cited on page 6).

[21] P. A. Cherenkov. 'Visible luminescence of pure liquids under the influence of γ-radiation'. In: *Dokl. Akad. Nauk SSSR* 2.8 (1934), pp. 451–454. DOI: 10.3367/UFNr.0093.196710n.0385 (cited on page 6).

[22] I. M. Frank and I. E. Tamm. 'Coherent visible radiation of fast electrons passing through matter'. In: *Compt. Rend. Acad. Sci. URSS* 14.3 (1937), pp. 109–114. DOI: 10.3367/UFNr.0093.196710o.0388 (cited on page 6).

[23] U.F. Katz. 'Cherenkov light imaging in astroparticle physics'. In: *Nuclear Instruments and Methods in Physics Research Section A: Accelerators, Spectrometers, Detectors and Associated Equipment* 952 (2020). 10th International Workshop on Ring Imaging Cherenkov Detectors (RICH 2018), p. 161654. DOI: https://doi.org/10.1016/j.nima.2018.11.113 (cited on page 6).

[24] J. V. Jelley. 'Cerenkov radiation and its applications'. In: *British Journal of Applied Physics* 6.7 (July 1955), p. 227. DOI: 10.1088/0508-3443/6/7/301 (cited on pages 6–8).

[25] R.C. Millard and G. Seaver. 'An index of refraction algorithm for seawater over temperature, pressure, salinity, density, and wavelength'. In: *Deep Sea Research Part A. Oceanographic Research Papers* 37.12 (1990), pp. 1909–1926. DOI: https://doi.org/10.1016/0198-0149(90)90086-B (cited on pages 7, 12).

[26] Curtis D. Mobley. *The Oceanic Optics Book*. en. 2022. DOI: 10.25607/OBP-1710. URL: https://repository.oceanbestpractices.org/handle/11329/1853 (cited on pages 7, 8, 11, 17, 19–22, 29, 31).

[27] Raymond C. Smith and Karen S. Baker. 'Optical Properties of the clearest natural waters (200-800 nm)'. In: *Applied Optics* 20.2 (1981), pp. 177–184 (cited on pages 8, 17, 19, 21).

[28] Carlos Pérez de los Heros. *Probing Particle Physics with Neutrino Telescopes*. WORLD SCIENTIFIC, 2020 (cited on page 8).

[29] M. G. Aartsen et al. 'Search for time-independent neutrino emission from astrophysical sources with 3 years of IceCube data'. In: *The Astrophysical Journal* 779.2 (Dec. 2013), p. 132. DOI: 10.1088/0004-637x/779/2/132 (cited on page 8).

[30] Annarita Margiotta. 'The KM3NeT deep-sea neutrino telescope'. In: *Nuclear Instruments and Methods in Physics Research Section A: Accelerators, Spectrometers, Detectors and Associated Equipment* 766 (2014). RICH2013 Proceedings of the Eighth International Workshop on Ring Imaging Cherenkov Detectors Shonan, Kanagawa, Japan, December 2-6, 2013, pp. 83–87. DOI: https://doi.org/10.1016/j.nima.2014.05.090 (cited on page 8).

[31] G. Riccobene et al. 'Deep seawater inherent optical properties in the Southern Ionian Sea'. In: *Astroparticle Physics* 27.1 (2007), pp. 1–9. DOI: https://doi.org/10.1016/j.astropartphys.2006.08.006 (cited on page 8).

[32] Felix Henningsen. 'Pacific Ocean Neutrino Experiment: Expected performance of the first cluster of strings'. In: *Proceedings of 38th International Cosmic Ray Conference — PoS(ICRC2023)*. ICRC2023. Sissa Medialab, July 2023. DOI: 10.22323/1.444.1053 (cited on pages 9, 52).

[33] OpenStreetMap contributors. *OpenStreetMap*. https://www.openstreetmap.org. 2024 (cited on page 9).

[34] Christian Haack and Lisa Johanna Schumacher. 'Machine-learning aided detector optimization of the Pacific Ocean Neutrino Experiment'. In: *Proceedings of 38th International Cosmic Ray Conference — PoS(ICRC2023)*. ICRC2023. Sissa Medialab, Aug. 2023. DOI: 10.22323/1.444.1059 (cited on page 10).

[35] Michael Bukshatb. *Photometry, Radiometry, and Measurements of Optical Losses*. Second. Springer Nature Singapore, 2019 (cited on page 11).

[36] Max Born and Emil Wolf. *Principles of Optics. Electromagnetic theory of propagation, interference and diffraction of light*. Seventh. Cambridge, United Kingdom: Cambridge University Press, 1999 (cited on pages 12, 13, 18).

[37] Withawat Withayachumnankul et al. 'A Systemized View of Superluminal Wave Propagation'. In: *Proceedings of the IEEE* 98.10 (2010), pp. 1775–1786. DOI: 10.1109/JPROC.2010.2052910 (cited on page 12).

[38] Lynne D. Talley et al. *Descriptive Physical Oceanography. An Introduction*. Sixth. London, United Kingdom: Academic Press, 2011 (cited on page 13).

[39] Enders A. Robinson and Sven Treitel. *Digital Imaging and Deconvolution: The ABCs of Seismic Exploration and Processing*. Society of Exploration Geophysicists, Jan. 2008 (cited on page 13).

[40] Martin Emilio Moorhead. 'Reflectors in Cherenkov Detectors'. PhD thesis. University of Oxford, 1992 (cited on pages 13–15).

[41] D. Motta and S. Schönert. 'Optical properties of bialkali photocathodes'. In: *Nuclear Instruments and Methods in Physics Research Section A: Accelerators, Spectrometers, Detectors and Associated Equipment* 539.1–2 (Feb. 2005), pp. 217–235. DOI: 10.1016/j.nima.2004.10.009 (cited on page 13).

[42] Hamamatsu Photonics K. K. *Photomultiplier Tubes. Basics and Applications*. Fourth. Hamamatsu Photonics K. K., 2017 (cited on page 13).

[43] Theodore J. Petzold. *Volume Scattering Functions for Selected Ocean Waters*. Oct. 1972 (cited on pages 17, 21, 48, 49).

[44] Fanyu Zhou et al. 'Feeding Ecology of Three Euphausiid Species in the North Pacific Ocean Inferred From 18S V9 Metabarcoding and Stable Isotope Analysis'. In: *Frontiers in Marine Science* 8 (2021). DOI: 10.3389/fmars.2021.756067 (cited on page 17).

[45] John Kessenich, Dave Baldwin, and Randi Rost. *The OpenGL®Shading Language, Version 4.60.8*. 2023 (cited on page 17).

[46] Matt Pharr, Wenzel Jakob, and Greg Humphreys. *Physically based rendering. From theory to implementation*. 4th Edition. Cambridge, Massachusetts: The MIT Press, 2023 (cited on pages 18, 23, 33, 37, 39, 41, 58).

[47] F.E. Nicodemus et al. *Geometrical Considerations and Nomenclature for Reflectance*. Gaithersburg, Maryland: U.S. Department of Commerce / National Bureau of Standards, Oct. 1977 (cited on page 18).

[48] A. von Finck et al. 'Parallelized multichannel BSDF measurements'. In: *Opt. Express* 23.26 (Dec. 2015), pp. 33493–33505. DOI: 10.1364/OE.23.033493 (cited on page 18).

[49] Addy Ngan, Frédo Durand, and Wojciech Matusik. 'Experimental Analysis of BRDF Models'. In: *Eurographics Symposium on Rendering (2005)*. Ed. by Kavita Bala and Philip Dutre. The Eurographics Association, 2005. DOI: 10.2312/EGWR/EGSR05/117-126 (cited on page 18).

[50] Curtis D. Mobley. *Light and Water. Radiative Transfer in Natural Waters*. San Diego, CA: Academic Press, 1994 (cited on pages 20, 21).

[51] L. G. Henyey and J. L. Greenstein. 'Diffuse radiation in the Galaxy.' In: *Astrophysical Journal* 93 (Jan. 1941), pp. 70–83. DOI: 10.1086/144246 (cited on page 20).

[52] Georges R. Fournier and Miroslaw Jonasz. 'Computer-based underwater imaging analysis'. In: *Airborne and In-Water Underwater Imaging*. Ed. by Gary D. Gilbert. Vol. 3761. International Society for Optics and Photonics. SPIE, 1999, pp. 62–70. DOI: 10.1117/12.366488 (cited on page 20).

[53] M. v. Smoluchowski. 'Molekular-kinetische Theorie der Opaleszenz von Gasen im kritischen Zustande, sowie einiger verwandter Erscheinungen'. In: *Annalen der Physik* 330.2 (1908), pp. 205–226. DOI: https://doi.org/10.1002/andp.19083300203 (cited on page 21).

[54] A. Einstein. 'Theorie der Opaleszenz von homogenen Flüssigkeiten und Flüssigkeitsgemischen in der Nähe des kritischen Zustandes'. In: *Annalen der Physik* 338.16 (1910), pp. 1275–1298. DOI: https://doi.org/10.1002/andp.19103381612 (cited on page 21).

[55] O.V. Kopelevich. 'Small-parameter model of optical properties of sea water'. In: *Ocean Optics, vol 1: Physical Ocean Optics*. Ed. by A.S. Monin. Nauka Pub., 1983. Chap. 8 (cited on page 21).

[56] O.V. Kopelevich and E.M. Mezhericher. 'Calculations of spectral characteristics of light scattering by sea water'. In: *Izv. Akad. Nauk. SSSR, Fiz. Atmos. Okeana* 19 (2 1983), p. 144 (cited on page 21).

[57] Jill Pasteris et al. 'Raman Spectroscopy in the Deep Ocean: Successes and Challenges'. In: *Applied spectroscopy* 58 (Aug. 2004), 195A–208A. DOI: 10.1366/0003702041389319 (cited on page 22).

[58] Jasmine Bartlett et al. 'Raman Scattering by Pure Water and Seawater'. In: *Applied optics* 37 (June 1998), pp. 3324–32. DOI: 10.1364/AO.37.003324 (cited on page 22).

[59] G. E. Walrafen. 'Raman Spectral Studies of the Effects of Temperature on Water Structure'. In: *The Journal of Chemical Physics* 47.1 (July 1967), pp. 114–126. DOI: 10.1063/1.1711834 (cited on page 22).

[60] S. Chandrasekhar. *Radiative Transfer*. New York: Dover Publications, 1960 (cited on page 23).

[61] Eric Veach. 'Robust Monte Carlo Methods for Light Transport Simulation'. PhD thesis. Stanford University, 1997 (cited on pages 25, 36, 42, 43).

[62] Tatianan Novikova and Jessica C. Ramella-Roman. 'Polarized Light'. In: *Polarized Light in Biomedical Imaging and Sensing. Clinical and Preclinical Applications*. Ed. by Jessica C. Ramella-Roman and Tatianan Novikova. Cham, Switzerland: Springer Nature Switzerland AG, 2023 (cited on page 27).

[63] George W. Kattawar et al. 'Polarization of light in the atmosphere and ocean'. In: *Light Scattering Reviews 10. Light Scattering and Radiative Transfer*. Ed. by Alexander A. Kokhanovsky. Berlin Heidelberg: Springer Heidelberg, 2016. Chap. 1 (cited on page 27).

[64] G. Franssens. 'Modelling polarization dependent absorption: The vectorial Lambert-Beer law'. In: *Asteroids, Comets, Meteors 2014*. Ed. by K. Muinonen et al. July 2014, p. 167 (cited on page 29).

[65] Kenneth J. Voss and Edward S. Fry. 'Measurement of the Mueller matrix for ocean water'. In: *Appl. Opt.* 23.23 (Dec. 1984), pp. 4427–4439. DOI: 10.1364/AO.23.004427 (cited on pages 29, 30, 49).

[66] Alexander A. Kokhanovsky. 'Parameterization of the Mueller matrix of oceanic waters'. In: *Journal of Geophysical Research: Oceans* 108.C6 (2003). DOI: https://doi.org/10.1029/2001JC001222 (cited on pages 29, 30).

[67] R.D.M. Garcia. 'Fresnel boundary and interface conditions for polarized radiative transfer in a multilayer medium'. In: *Journal of Quantitative Spectroscopy and Radiative Transfer* 113.4 (2012), pp. 306–317. DOI: https://doi.org/10.1016/j.jqsrt.2011.11.015 (cited on page 29).

[68] Tatianan Novikova and Jessica C. Ramella-Roman. 'Polarized-Sensitive Monte Carlo'. In: *Polarized Light in Biomedical Imaging and Sensing. Clinical and Preclinical Applications*. Ed. by Jessica C. Ramella-Roman and Tatianan Novikova. Cham, Switzerland: Springer Nature Switzerland AG, 2023 (cited on page 31).

[69] Michal Mojzík et al. 'Bi-Directional Polarised Light Transport'. In: *Eurographics Symposium on Rendering - Experimental Ideas & Implementations*. Ed. by Elmar Eisemann and Eugene Fiume. The Eurographics Association, 2016. DOI: 10.2312/sre.20161215 (cited on page 31).

[70] Wenzel Alban Jakob. 'Light Transport on Path-Space Manifolds'. PhD thesis. Cornell University, 2013 (cited on page 33).

[71] Nicholas Metropolis and S. Ulam. 'The Monte Carlo Method'. In: *Journal of the American Statistical Association* 44.247 (1949), pp. 335–341 (cited on page 35).

[72] B. J. Archer Avneet Sood R. Arthur Forster and R. C. Little. 'Neutronics Calculation Advances at Los Alamos: Manhattan Project to Monte Carlo'. In: *Nuclear Technology* 207.sup1 (2021), S100–S133. DOI: 10.1080/00295450.2021.1956255 (cited on page 35).

[73] Christiane Lemieux. *Monte Carlo and Quasi-Monte Carlo Sampling*. New York: Springer Science+Business Media, 2009 (cited on pages 35–37).

[74] Sebastiano Vigna. *It is high time we let go of the Mersenne Twister*. 2019 (cited on page 37).

[75] John K. Salmon et al. 'Parallel random numbers: As easy as 1, 2, 3'. In: *SC '11: Proceedings of 2011 International Conference for High Performance Computing, Networking, Storage and Analysis*. 2011, pp. 1–12. DOI: 10.1145/2063384.2063405 (cited on page 37).

[76] I.M Sobol'. 'On the distribution of points in a cube and the approximate evaluation of integrals'. In: *USSR Computational Mathematics and Mathematical Physics* 7.4 (1967), pp. 86–112. DOI: https://doi.org/10.1016/0041-5553(67)90144-9 (cited on page 37).

[77] Art B. Owen. 'Variance with alternative scramblings of digital nets'. In: *ACM Trans. Model. Comput. Simul.* 13.4 (2003), pp. 363–378. DOI: 10.1145/945511.945518 (cited on page 37).

[78] Pierre L'Ecuyer. 'Randomized Quasi-Monte Carlo: An Introduction for Practitioners'. In: *12th International Conference on Monte Carlo and Quasi-Monte Carlo Methods in Scientific Computing (MCQMC 2016)*. Stanford, United States, Aug. 2016 (cited on page 37).

[79] Adrian Jarabo et al. 'A Framework for Transient Rendering'. In: *ACM Transactions on Graphics (Proceedings of SIGGRAPH Asia)* 33.6 (Nov. 2014). DOI: 10/gfznb8 (cited on page 39).

[80] Eric P. Lafortune and Yves D. Willems. 'Bi-directional path tracing'. In: *Proceedings of Third International Conference on Computational Graphics and Visualization Techniques (Compugraphics '93)*. Alvor, Portugal, Dec. 1993, pp. 145–153 (cited on page 42).

[81] Matt Pharr, Wenzel Jakob, and Greg Humphreys. *Physically Based Rendering. From theory to implementation*. 3rd Edition. San Francisco, CA, USA: Morgan Kaufmann Publishers Inc., Nov. 2016, p. 1266 (cited on page 42).

[82] Nicolai Bailly et al. 'Two-year optical site characterization for the Pacific Ocean Neutrino Experiment (P-ONE) in the Cascadia Basin'. In: *The European Physical Journal C* 81.12 (Dec. 2021). DOI: 10.1140/epjc/s10052-021-09872-5 (cited on pages 48, 49).

[83] Rastislav Dvornicky. 'Monitoring of optical properties of deep waters of Lake Baikal in 2021-2022'. In: *Proceedings of 38th International Cosmic Ray Conference — PoS(ICRC2023)*. ICRC2023. Sissa Medialab, July 2023. DOI: 10.22323/1.444.0977 (cited on page 48).

[84] E.G. Anassontzis et al. 'Light transmission measurements with LAMS in the Mediterranean Sea'. In: *Nuclear Instruments and Methods in Physics Research Section A: Accelerators, Spectrometers, Detectors and Associated Equipment* 626–627 (Jan. 2011), S120–S123. DOI: 10.1016/j.nima.2010.06.353 (cited on page 48).

[85] Jakub Stacho et al. 'Development of Calibration Light Sources for the Pacific Ocean Neutrino Experiment'. In: *Proceedings of 38th International Cosmic Ray Conference — PoS(ICRC2023)*. ICRC2023. Sissa Medialab, July 2023. DOI: 10.22323/1.444.1113 (cited on page 49).

[86] Felix Henningsen. 'Optical Characterization of the Deep Pacific Ocean: Development of an Optical Sensor Array for a Future Neutrino Telescope'. MA thesis. TUM, 2018 (cited on page 50).

[87] Erich Strohmaier et al. *November 2023 | TOP500*. (Accessed on May 4, 2024). Nov. 2023. URL: https://top500.org/lists/top500/2023/11/ (cited on page 57).

[88] Adam Marrs, Peter Shirley, and Ingo Wald, eds. *Ray Tracing Gems II. Next Generation Real-Time Rendering with DXR, Vulkan, and OptiX*. Apress Berkeley, CA, Aug. 2021. DOI: https://doi.org/10.1007/978-1-4842-7185-8 (cited on page 57).

[89] John L. Hennessy and David A. Patterson. *Computer Architecture. A Quantitative Approach*. Cambridge, MA: Morgan Kaufmann, 2017 (cited on page 57).

[90] Nvidia. *Nvidia Ada GPU Architecture*. (v2.1). 2023 (cited on page 57).

[91] Samuli Laine, Tero Karras, and Timo Aila. 'Megakernels considered harmful: wavefront path tracing on GPUs'. In: *Proceedings of the 5th High-Performance Graphics Conference*. HPG '13. Anaheim, California: Association for Computing Machinery, 2013, pp. 137–143. DOI: 10.1145/2492045.2492060 (cited on page 57).

[92] Wenzel Jakob et al. *Mitsuba 3 renderer*. Version 3.1.1. https://mitsuba-renderer.org. 2022 (cited on page 57).

[93] Wenzel Jakob et al. 'Dr.Jit: A Just-In-Time Compiler for Differentiable Rendering'. In: *Transactions on Graphics (Proceedings of SIGGRAPH)* 41.4 (July 2022). DOI: 10.1145/3528223.3530099 (cited on page 57).

[94] V. V. Sanzharov, V. A. Frolov, and V. A. Galaktionov. 'Survey of Nvidia RTX Technology'. In: *Programming and Computer Software* 46.4 (July 2020), pp. 297–304. DOI: 10.1134/s0361768820030068 (cited on page 58).

[95] Nvidia. *Nvidia Turing GPU Architecture*. 2018 (cited on page 58).

[96] The Khronos® Vulkan Working Group. *Vulkan® 1.3.285. A Specification (with all ratified extensions)*. May 2024 (cited on page 58).